Hardness of Electrodeposited Nano-Nickel Revisited

by

Bill Tsz Fai Tang

A thesis submitted in conformity with the requirements

for the degree of Master of Applied Science

Department of Materials Science and Engineering

University of Toronto

Hardness of Electrodeposited Nano-Nickel Revisited

Bill Tsz Fai Tang

Master of Applied Science

Department of Materials Science and Engineering
University of Toronto

2011

Abstract

In the past, hardness measurements on nanocrystalline metals were limited to Vickers micro-hardness and nano-indentation tests, mainly due to sample size/thickness limitations. On the other hand, most industries require hardness values on the Rockwell scale and make extensive use of hardness conversion relationships for various hardness scales. However, hardness conversions currently do not exist for nanocrystalline metals. With recent advances in electrodeposition technology, thicker specimens with a wide range of grain sizes can now be produced. In this study, the relationships between Vickers and Rockwell hardness scales have been developed for such materials. In addition, hardness indentations were used to gain further insight into the work hardening of nanocrystalline and polycrystalline nickel. Vickers microhardness and nano-indentation profiles below large Rockwell indentations showed that polycrystalline nickel exhibited considerable strain hardening, as expected. On the other hand, for nanocrystalline nickel the micro-Vickers and nano-indentations hardness profile showed low strain hardening capacity.

Acknowledgements

I would like to express my sincerest thanks to my supervisor, Professor Uwe Erb, who provided me with guidance and patience, along with a sense of humour which made the experience enjoyable. I would also like to thank Mr. Iain Brooks of Integran Technologies, Inc for providing the materials needed for this research and Dr. Gordana Cingara for her TEM work.

Financial support from the Natural Sciences and Engineering Research Council of Canada, the Ontario Research Fund and the University of Toronto Open Fellowship are also gratefully recognized.

Most importantly, I would like to thank the most important people in my life – my family and my girlfriend, Winnie Luy. Their faith in me and support had made everything possible. I am truly fortunate to have them in my life and I would like to devote this thesis to them.

Table of Contents

Abstract ... ii

Acknowledgements ... iv

List of Tables ... vii

List of Figures ... viii

Chapter 1: Introduction ... 1

Chapter 2: Literature Review ... 5

- 2.1 Synthesis of Nanocrystalline Materials ... 5
  - *2.1.1* Solid State *Processing ... 5*
    - 2.1.1.1 Equal-Channel Angular Pressing (ECAP) ... 6
    - 2.1.1.2 Mechanical Attrition ... 6
  - 2.1.2 Vapour Phase Processing ... *9*
  - 2.1.3 Crystallization of Amorphous Precursors ... *11*
  - *2.1.4* Electrochemical Processing ... *11*
- 2.2 Characteristics Structure of Nanomaterials ... 14
- 2.3 Properties of Electrodeposited Nanocrystalline Materials ... 16
  - *2.3.1* Mechanical Properties of Nanocrystalline Materials ... *17*
- 2.4 Deformation Mechanisms in Nanocrystalline Materials ... 18
  - *2.4.1* Grain Boundary Sliding and Grain Rotation ... *19*
  - *2.4.2 Nabarro-Herring Creep ... 23*
  - *2.4.3 Coble Creep ... 24*
- 2.5 Strain Hardening in Polycrystalline and Nanocrystalline Materials ... 25
- 2.6 Hardness ... 31
  - *2.6.1 Rockwell and Superficial Rockwell Hardness ... 32*
  - *2.6.2 Brinell Hardness ... 33*
  - *2.6.3 Vickers and Knoop Hardness ... 34*
  - *2.6.4 Nanoindentation Hardness ... 36*

2.6.5 Summary of Hardness Tests 37
2.7 Hardness Conversion Relationship........ 38
2.8 Objectives of this Research 38
Chapter 3: Materials and Experimental Methods 40
3.1 Materials and Sample Preparation 40
3.2 Materials Characterization........ 42
3.2.1 Energy-Dispersive X-ray Spectroscopy (EDX)........ 42
3.2.2 Grain Size Analysis........ 42
3.2.2.1 Transmission Electron Microscopy (TEM)........42
3.2.2.2 Optical Imaging of Polycrystalline Microstructure........43
3.3 Mechanical Testing........ 43
3.3.1 Rockwell Hardness Testing 43
3.3.2 Vickers Micro-hardness Testing........ 44
3.3.3 Nanoindentation Hardness Testing 44
Chapter 4: Results and Discussion........45
4.1 Characterization of Materials........ 45
4.1.1 Grain Size Analysis 45
4.1.2 EDX Analysis........ 55
4.2 Vickers Micro-hardness........ 56
4.3 Rockwell and Superficial Rockwel Hardness........ 58
4.4 Relationship between Vickers and Rockwell Scales........ 61
4.5 Strain Hardening Capacity........ 67
Chapter 5: Conclusion 79
Chapter 6: Recommendation for Future Work........81
Chapter 7: References 82
Appendix........85

List of Tables

Table 2.1: Upper and lower limits for critical distance between two dislocations [modified after Wang (1994)].

Table 2.2: Summaries of the static hardness indentation tests

Table 4.1: Average grain sizes of the specimen used in this experiment

Table 4.2: Compositsion of the materials in weight percentage, as determined by energy-dispersive X-ray spectroscopy analysis

Table 4.3: Average Vickers Micro-hardness measurements

Table 4.4: Average Rockwell hardness measurements

Table 4.5: Average Superficial Rockwell hardness measurements

Table 4.6: Vickers to Superficial Rockwell Hardness Relationships

Table 4.7: Vickers to Rockwell Hardness Relationships

Table 4.8: Average Vickers Micro-hardness measured at 100 grams

List of Figures

Figure 2.1: (a) Schematic representation of ECAP [Komura et al. (1999)], (b) the four processing routes for ECAP, rotation between each pass [Iwahashi et al. (1998)]

Figure 2.2: (a) Schematic representation of mechanical attrition [Fecht, (1990)], (b) Schematic representation of the consolidated structure [Birringer et al. 1988]

Figure 2.3: Schematic drawing of a inert gas condensation synthesis technique [Siegel et al. (1989)]

Figure 2.4: Schematic of an electrodeposition set up [Cheung (2001)]

Figure 2.5: Schematic diagram of (a) Diffusion processes on the surface of the specimen and (b) the Nernst diffusion layer [Erb et al. (2007)]

Figure 2.6: Schematic diagram of the atomic arrangement in nanocrystalline materials. The black circles represent the ordered structure, the grains; the white circles represent the disordered structure, the intercrystalline component [Gleiter (1989)].

Figure 2.7: (a) The 14- sided tetrakaidecahedron grain shape, [Allen and Thomas (2003)] and (b) the volume fractions of total intercrystal components (V_{ic}), grain boundary (V_{gb}) and triple junctions (V_{tj}) as a function of grain size, [Palumbo et al. (1990)]

Figure 2.8: Plot of Vickers micro-hardness against one over square root of grain size, [Armstrong et al. (1896)]

Figure 2.9: Low temperature deformation mechanisms in nanocrystalline metals, from [Erb et al. (2004)]

Figure 2.10: Schematic diagram of a) grain boundary sliding with a protrusion in the boundary, b) grain boundary sliding of the triple junction, Gifkins and Snowden [1966]

Figure 2.11: Schematic diagram of grain boundary sliding, proposed by Hahn et al. [1997]

Figure 2.12: Schematic diagram of grain rotation of nanocrystalline material under tensile loading due to disclination dipole motion, as proposed by Ovid'ko [2002]

Figure 2.13: Nabarro-Herring vacancy diffusion mechanism through a grain during loading, Herring [1949]

Figure 2.14: Coble vacancy diffusion mechanism along grain boundary during loading, Ashby [1969]

Figure 2.15: The strain hardening behaviour of copper, brass and steel increase in tensile strength with increase in cold work [Callister (2005)].

Figure 2.16: Plot of Vickers micro-hardness against elongation for as-received and cold-rolled polycrystalline nickel [Liang and Yu, (2008)]

Figure 2.17: Plot of Vickers micro-hardness against elongation for as-received and cold rolled polycrystalline and nanocrystalline nickel [Zabev, (2008)]

Figure 2.18: Plot of yield strength against rolling strain, where yield strength is determined by one third of Vickers micro-hardness relationship [Wu et al. (2009)]

Figure 2.19: Schematic diagram of the cross section of Rockwell hardness measurement, modified [ASTM E18 – 08, (2008)]

Figure 2.20: Schematic diagram of the indenter and indentation of Vickers and Knoop hardness [Callister (2005)].

Figure 2.21: Schematic diagram of the Berkovich indenter

Figure 3.1: Schematic diagram of the cross section below the Rockwell indentation. Vickers micro-hardness profiles were measured along direction x.

Figure 4.1: Optical micrograph of polycrystalline nickel, Ni 1

Figure 4.2: Grain size distribution histogram for polycrystalline nickel, Ni 1

Figure 4.3: Plot of frequency against grain size for the polycrystalline nickel (Ni 1) with superimposed log-normal distribution

Figure 4.4: Plot of cumulative volume fraction against grain size for the polycrystalline nickel, Ni

Figure 4.5: Bright field TEM image, dark field, TEM image and SADP of ultra-fine grained nickel sample, Ni 4

Figure 4.6: Grain size distribution histogram for ultra-fine-grained nickel, Ni 4

Figure 4.7: Plot of frequency against grain size for the ultra-fine-grained nickel (Ni 4) with superimposed log-normal distribution.

Figure 4.8: Plot of cumulative volume fraction against grain size for the ultra-fine-grained nickel, Ni 4

Figure 4.9: Bright field TEM image, dark field, TEM image and SADP of nanocrystalline nickel sample, Ni 6

Figure 4.10: Grain size distribution histogram for nanocrystalline nickel sample, Ni 6

Figure 4. 11: Plot of frequency against grain size for nanocrystalline nickel sample (Ni 6) with superimposed log-normal distribution

Figure 4.12: Plot of cumulative volume fraction against grain size for nanocrystalline nickel sample, Ni 6

Figure 4.13: Vickers hardness plotted against grain size

Figure 4.14: Hardness plotted against $d^{-0.5}$ a) Rockwell, b) Superficial Rockwell Ball indenter and c) Superficial Rockwell Diamond indenter

Figure 4.15: Experimental results and ASTM relationship of Vickers Micro-hardness plotted against a) Superficial Rockwell, Ball indenter, b) Superficial Rockwell, Diamond indenter, c) Rockwell, Ball indenter and d) Rockwell, Diamond indenter

Figure 4.16: Optical micrographs of the cross sections of Rockwell indentations in a) Ni 1, Diamond indenter, b) Ni 1, Ball indenter, c) Ni 5, Diamond indenter, d) Ni 5, Ball indenter, e) Ni 6, Diamond indenter and f) Ni 6, Ball indenter

Figure 4.17: Vickers micro-hardness as a function of distance from the Rockwell Diamond indentation

Figure 4.18: Vickers micro-hardness as a function of distance from the Ball indentation

Figure 4.19: Normalized hardness as a function of distance from Rockwell indentation, under Rockwell Diamond indentations

Figure 4.20: Normalized hardness as a function of distance from Rockwell indentation, under Rockwell Ball indentations

Figure 4.21: Optical micrographs of the cross sections of Rockwell Diamond indentation in Ni 6

Figure 4.22: Normalized nanoindentation hardness as a function of distance from Rockwell indentation against under Rockwell Diamond indentation

1.0 Introduction

Nanocrystalline metals are defined as metals with grain sizes less than 100 nm. These materials have drawn considerable industrial and academic interest due to the substantial improvements of certain properties. Extensive research has shown that with the reduction in grain size properties such as strength [e.g. Nieman et al. (1990)], wear rate [e.g. Jeong (2003)], magnetic coercivity [Herzer et al. (1989)], corrosion behaviour [e.g. Rofagha et al. (1991)] and hardness [e.g. Gleiter (1989)] are greatly enhanced and surpass the properties observed in the larger grained, polycrystalline materials.

Many different synthesis techniques for the production of nanocrystalline materials have been developed over the past three decades. These synthesis techniques include severe plastic deformation [e.g Valiev et al. (1999)], physical vapour deposition [e.g Iwama et al. (1992)], chemical vapour deposition [e.g Gleiter (1981)], sputtering [e.g Grovenor et al. (1984)], crystallization of amorphous materials [e.g Herzer (1995)], inert gas condensation [e.g Gleiter (1981)], electrodepostion [e.g McMahon and Erb (1989)], etc. Each method uses different mechanisms to create the nanocrystalline structure such that the internal porosity, impurity content and grain boundary structure formation of the end product may differ considerably from one technique to another. Hence, by fabricating nanocrystalline materials with different methods, there could be substantial variations in their properties [e.g Siegel (1993)].

A previous study by Palumbo et al. has shown that through grain refinement (reducing the size of an idealized 14- sided tetrakaidecahedron as the grain shape model) to the nanocrystalline regime, the total intercrystal volume (sum of grain boundaries and triple junctions) can increase to a significant fraction of the total material volume [Palumbo et al. (1990)]. For example, this increase in interfacial volume fractions is an important aspect in interpreting many mechanical properties of nanocrystalline materials, as deformation mechanisms in nanocrystalline materials are quite different than in polycrystalline materials. Several known deformation mechanisms in nanocrystalline materials at low temperature are operative in polycrystalline materials only at high stress or high temperatures. These include: grain rotation, grain boundary sliding, Coble creep and Nabarro-Herring creep. Since grain size, grain boundary structure and secondary defects (e.g. porosity, impurities) all play a major role in deformation mechanisms, the synthesis technique can have a significant influence on the performance of nanomaterials under plastic deformation conditions.

It is well established that the hardness and strength of metals increase with the refinement of grain size to the nanocrystalline regime. This behaviour is the well known classical Hall-Petch behaviour [Hall (1951), Petch (1953)]. In the past, hardness measurements for nanocrystalline metals were usually limited to Vickers micro-hardness and nano-indentation hardness tests. This was mainly due to sample size/thickness limitations of available nanomaterials produced in research laboratories.

In industrial applications, however, the hardness of materials is often determined by other methods, including the Brinell, Rockwell, and Superficial Rockwell methods. The Rockwell and

Superficial Rockwell hardness scales are of particular importance as they are often used as non-destructive tests in quality control of finished parts [ASTM E18 – 08b, (2008)]. Conversion tables and empirical relationships to compare the different hardness scales are available for several conventional materials from the American Society for Testing and Materials (ASTM). However, there are currently no conversion tables available, for nanocrystalline materials in which the hardness is controlled by grain size.

Through recent advances in the electroplating technology, much larger nanocrystalline metal geometries can now be produced. With thicker specimens, Rockwell hardness measurements can now be made following the ASTM Standard E-18, Standard Test Methods for Rockwell Hardness of Materials [2008]. The main objective of the present work is to obtain Rockwell and Superficial Rockwell hardness values for polycrystalline and nanocrystalline nickel with different grain sizes and to develop a relationship between the Vickers and Rockwell hardness scales. In addition, a combination of Rockwell, Vickers and nano indentations were used to gain further insight into the work hardening behaviour of nanocrystalline nickel in comparison with conventional polycrystalline nickel. A total of seven specimens of nickel with varying grain sizes were used in which strengthening is mainly due to grain size reduction.

The thesis is organized as follows. Chapter 2 presents a literature review on nanocrystalline materials, discussing some of the common synthesis methods used for the production of such materials, the characteristic structures of nanocrystalline materials and various deformation mechanisms. The experimental section, Chapter 3, will discuss the methods applied to characterize the material used in this study and the hardness measurement procedures applied throughout this work. The experimental results on the relationship between Rockwell hardness scale and Vickers-micro hardness along with the strain hardening behaviour are presented and discussed in Chapter 4. Lastly, the conclusions drawn from this work and recommendations for future work are presented in Chapters 5 and 6, respectively.

2.0 Literature Review

This chapter presents a review of various types of synthesis techniques (Chapter 2.1) and the resulting structures and defects embedded within nanocrystalline materials (Chapter 2.2). Following this, the mechanical strengthening behaviour and deformation mechanisms of nanocrystalline materials are presented (Chapter 2.3).

2.1 Synthesis of Nanocrystalline Materials

There are various different synthesis techniques to produce nanocrystalline materials and the majority of these methods can be categorized into five distinct approaches: solid state processing, chemical synthesis, electrochemical synthesis, vapour phase processing and liquid state processing [Erb et al. (2007)]. These techniques range from top-down approaches in which nanocrystalline materials are produced from bulk polycrystalline precursor materials to bottom-up methods in which materials are made atom by atom. Many studies have shown that the synthesis method used has a great effect on the grain size, grain boundary structures and properties of the resulting product. Hence, in any comparison of the deformation behaviour and other properties of nanocrystalline materials, the synthesis method must be considered.

2.1.1 Solid State Processing

Both bulk processing and powder synthesis are used to manufacture nanocrystalline materials by solid state processing. A common characteristic for these processes is that the reduction of grain size is generated by successive refinement of dislocation cells or sub grain boundary networks through mechanical deformation under shear conditions and high strain rates [Fecht et al. (2007)].

2.1.1.1 Equal-Channel Angular Pressing (ECAP)

Equal-Channel Angular Pressing, ECAP, is a severe plastic deformation processing technique where a bulk polycrystalline precursor material is plastically deformed through one of several processing routes [e.g. Valiev et al. (1999)]. A billet specimen is placed into a die, then a plunger applies pressure to press the specimen out through an angle, usually 90º, Fig. 2.1a. This process is repeated several times according to one of four different processing routes, Fig. 2.1b. The final grain structure and grain size are different for the various routes and depend on the number of passes made through the die. However, there is a limitation with this processing method. Grain refinement to less than 50 nm through this deformation process is usually not possible.

2.1.1.2 Mechanical Attrition

Similar to ECAP, mechanical attrition requires extensive deformation of the precursor materials. However, the starting material used in this method is in powder form. Thus, this synthesis technique consists of two steps. First the powder undergoes mechanical deformation, and then additional consolidation steps are required to form the final product [e.g. Fecht (1990)]. The precursor powder is subjected to mechanical deformation between milling balls which are usually made of hardened steel or tungsten carbide, Fig. 2.2a. A variety of ball mills have been developed, such as: shaker mills, vibratory mills, tumbler mills and attrition mills. The large strain exerted by the balls continuously deforms, fractures and cold welds the powder particles. During this process, dislocations fill up the dislocation boundaries to maximum possible

a)

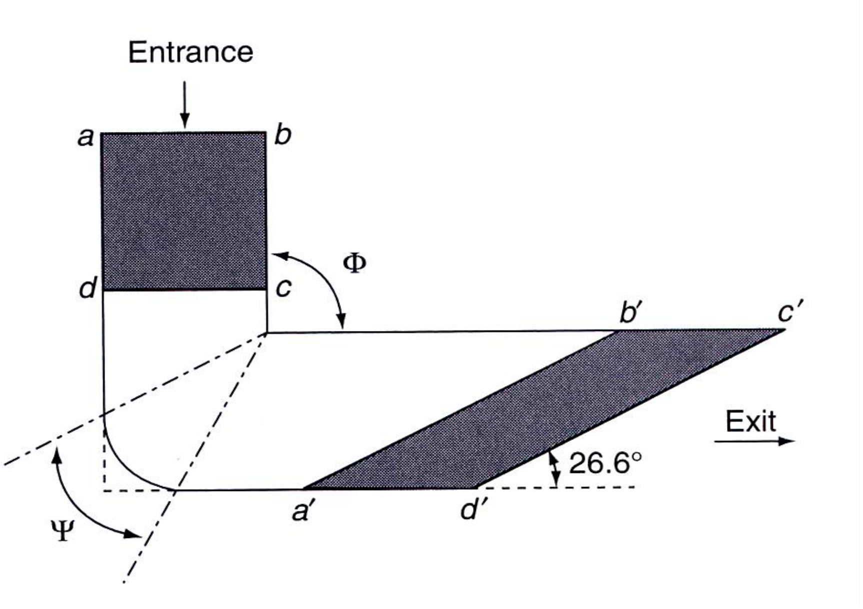

b)

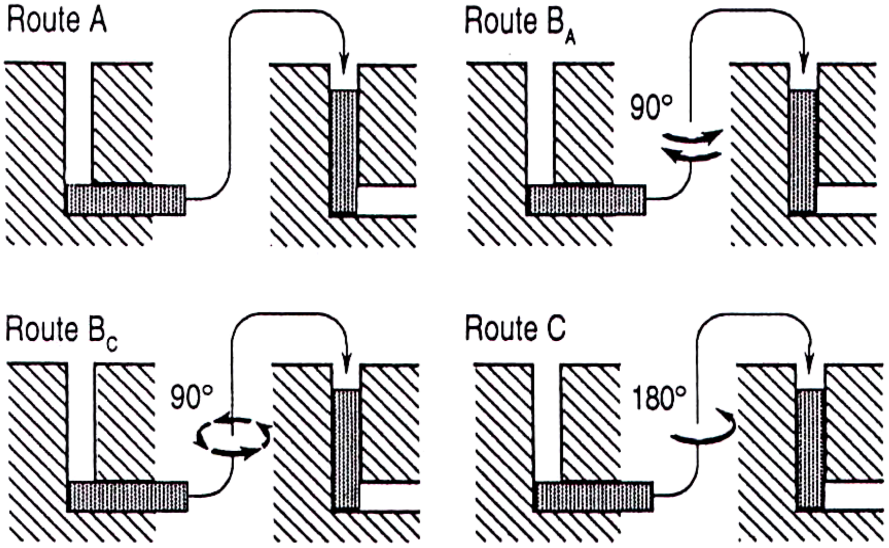

Figure 2.1: (a) Schematic representation of ECAP [Komura et al. (1999)], (b) the four processing routes for ECAP with sample rotation between each pass [Iwahashi et al. (1998)]

dislocation density; subsequently, high angle grain boundaries are formed. With extended milling time, the micro-strains within the powders increase and the grains eventually reach the nanocrystalline regime, in some cases even the amorphous structure.

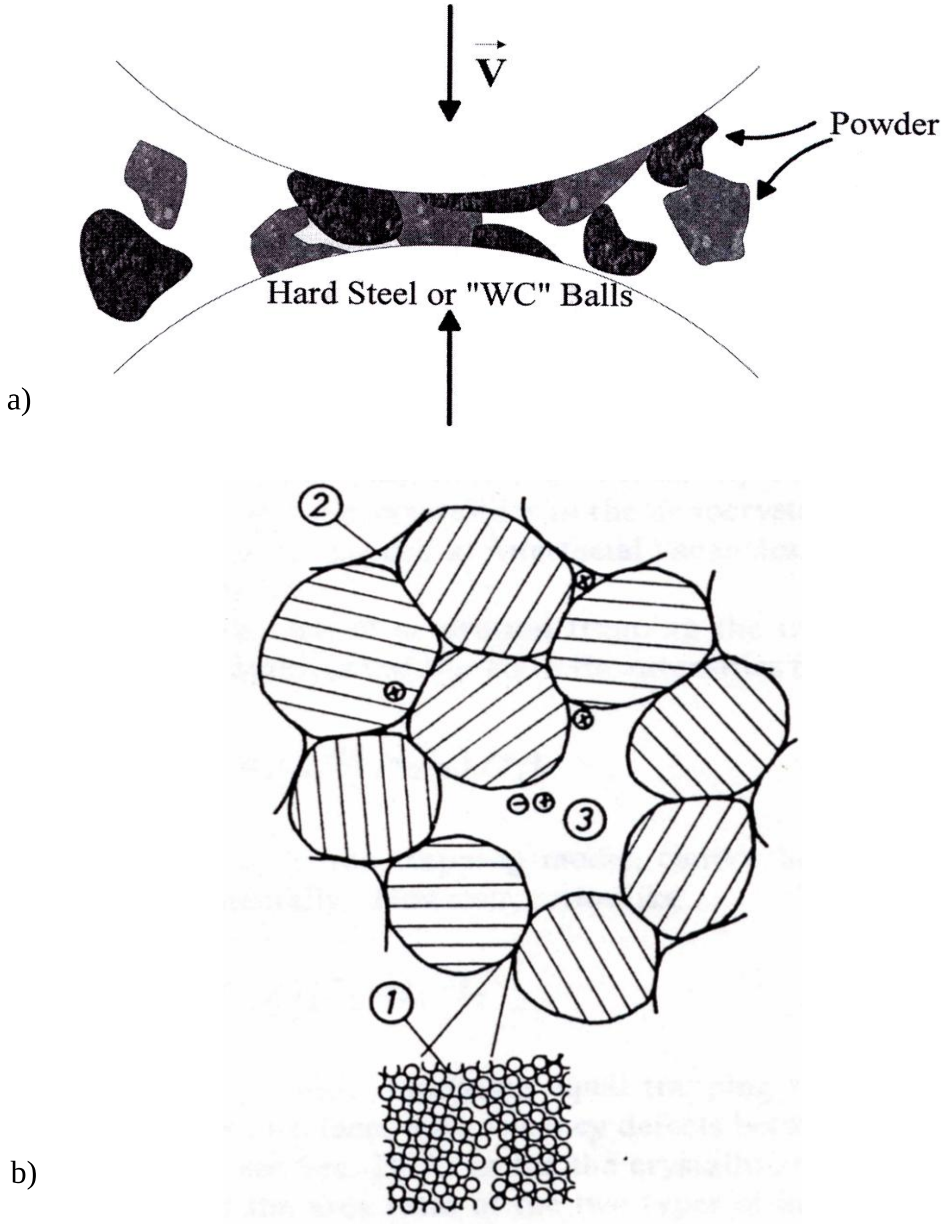

Figure 2.2: (a) Schematic representation of mechanical attrition [Fecht, (1990)], (b) Schematic representation of the consolidated structure [Birringer et al. 1988]

Although this synthesis technique is inexpensive and many nanocrystalline alloys can be produced, interface and surface contamination are a common problem. In the resulting powders, significant amounts of wear debris from the grinding media are formed and these are usually impurities in the resulting product. Furthermore, the required consolidation of the powders to make bulk materials also presents a problem in that the final structure often contains porosity, Fig. 2.2b. This porosity content can be as high as 5-25% of the final material. Thus, the mechanical properties observed on these materials could be different than the properties of fully dense nanocrystalline materials. During the consolidation process, contact points are formed between the particles and this constructs the load-bearing skeleton of this structure which makes further compaction difficult. Hence, it is very difficult to eliminate all the porosity without applying high temperatures. To achieve higher densities, diffusion in the materials must be increased by raising the temperature during densification [e.g. Wu et al. (1999)]. However, through the thermal processes, dislocation climb could lead to recovery and grain growth which will also affect the properties of the final product [e.g. Rawers et al. (1996]].

2.1.2 Vapour Phase Processing

Vapour phase processing is a bottom up synthesis technique in which nanostructured products are produced atom-by-atom through the evaporation and deposition of a material under high vacuum conditions or is an inert gas atmosphere. One common vapour phase processing technique is inert gas condensation through which a large range of materials can be produced [Gleiter (1981)]. Virtually any material that can be vaporized can be synthesised into nanocrystalline material with this technique. This process takes place in a chamber filled with inert gas such as Ar, He or Xe at a low pressure. Within the chamber, a metal is vaporized by thermal evaporation, electron beam evaporation or laser ablation. The metal atoms condense rapidly to form nano-particles during the collisions with the inert gas molecules. To collect the particles suspended in the flow gas, a liquid nitrogen cooled cold finger is placed in the middle of the chamber to attract them. Once all the particles are collected by the cold finger, the powders are scraped off from the cold finger, compacted and sintered into the final product under vacuum condition [Gleiter, (1989)]. After consolidation, the density of the samples is approximately 90-95%. Through altering process parameters such as inert gas partial pressure and temperature, a range of nanoparticle sizes can be made.

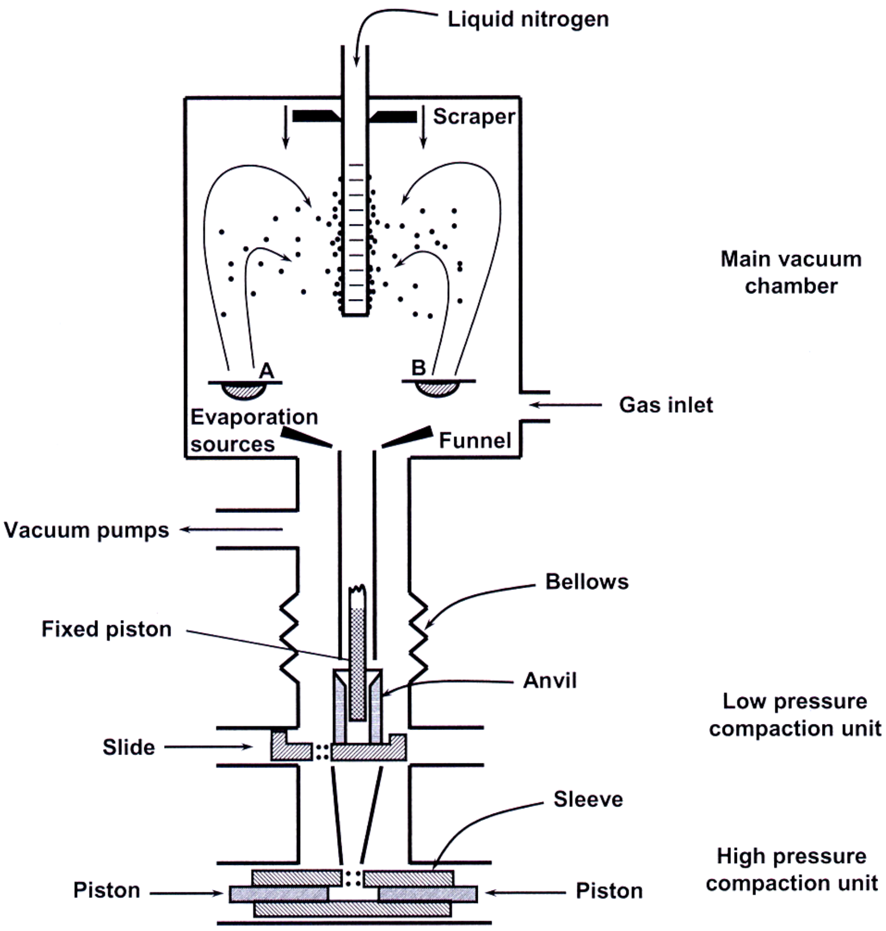

Figure 2.3: Schematic drawing of the inert gas condensation synthesis technique [Siegel et al. (1989)]

Many of the early studies on nanocrystalline materials were based on these materials. However, the properties observed were often affected by the lower density in these materials. Agglomeration of particles is a major drawback in this synthesis technique which leads to the formation of artifacts in the final product such as interparticle and interagglomerate pores that influence the overall properties.

2.1.3 Crystallization of Amorphous Precursors

Rapid solidification of materials was originally developed to produce amorphous metals, but is now an established route for producing precursor amorphous metals to yield fully dense and porosity-free nanocrystalline materials. The crystallization of amorphous precursors occurs through controlled annealing. To obtain the specific nanocrystalline structure from the amorphous precursor material, controlled grain growth is induced. In this process, annealing temperature and time are adjusted to obtain the desired grain size [e.g. Lu et al. (1990)]. However, pure metals cannot be rapidly quenched with the amorphous structure; thus, crystallization of amorphous precursors has the ability to fabricate nanocrystalline alloys but not pure nanocrystalline metals. Also, the thickness of the resulting product is a limitation for this process, due to the required heat transfer during the rapid solidification step. Materials made by this process are usually less than 100 µm in thickness.

2.1.4 Electrochemical Processing

Electrochemical processing is also a bottom-up synthesis route. The process involves charge transfer at the interfaces of an anode and a cathode. One of the well established methods is electrodeposition, which is used to synthesize fully dense surface coatings and bulk materials, with little limitations in the shape and size of the resulting product. The basic setup consists of a cathode and an anode submerged into an aqueous solution in which the cathodic and anodic reactions are driven by an external power supply, Fig. 2.4 [Erb et al. (2007)].

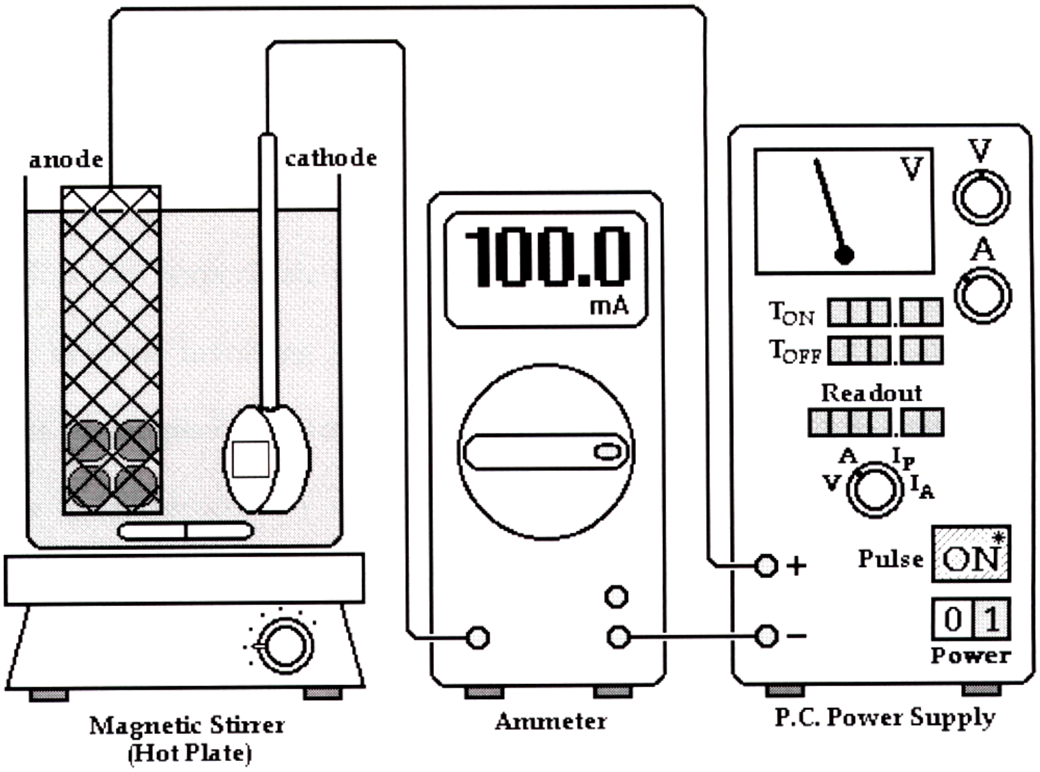

Figure 2.4: Schematic diagram of an electrodeposition set up [Cheung (2001)]

During the deposition process, metal ions in the aqueous solution are reduced and deposited onto the cathode. As this reaction continues the metal ion concentration within the solution depletes. Thus, as this process carries on, metal ions are continuously replenished into the solution by dissolving the anode which is the same metal as the deposit. The main process parameters in electrodeposition include bath composition, temperature, overpotential, bath additives, pH, etc. By altering these parameters, a wide range of grain sizes and structures are possible.

To electroplate nanocrystalline materials, nucleation of new grains must be promoted and the growth of existing grains must be suppressed. At low overpotential and high surface diffusion, grain growth is favoured; for this reason high overpotential and low diffusion rates are the optimal conditions for plating nanocrystalline materials. Nucleation can be promoted by increasing the current density and using pulsed current depositions. This allows higher deposition rates by increasing the mass transfer and metallic ion replenishing rate in the Nernst diffusion layer, Fig. 2.5a. Furthermore, with the addition of grain refiners to the plating bath, the surface mobility of the atoms on the deposit surface is reduced; thus, grain growth is hindered.

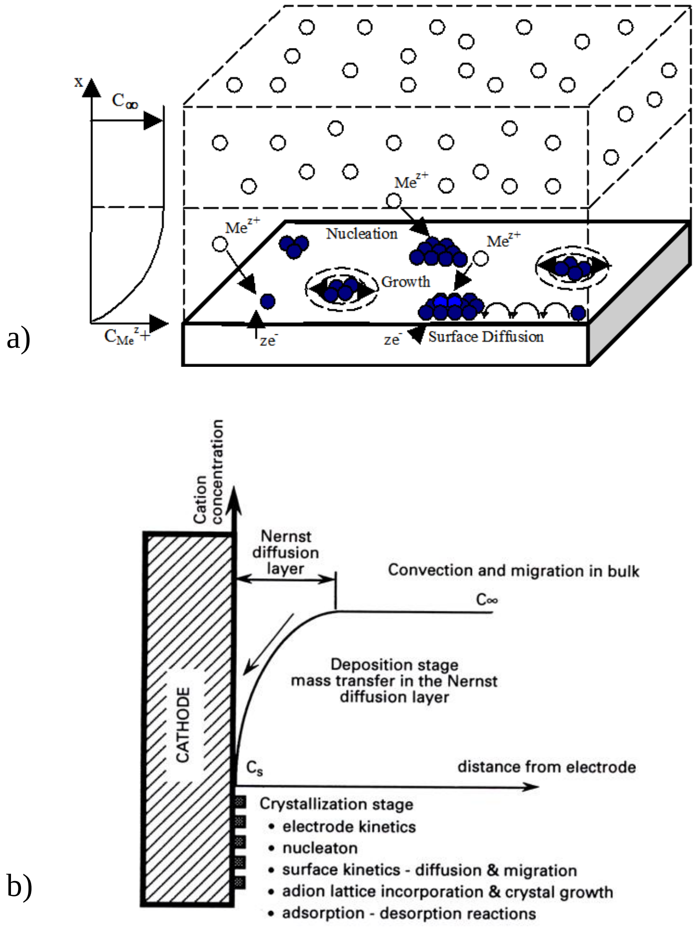

Figure 2.5: Schematic diagram of (a) Diffusion processes on the surface of the specimen and (b) the Nernst diffusion layer [Erb et al. (2007)]

2.2 Characteristic Structure of Nanomaterials

Nanocrystalline materials can be produced in many different shapes including particles, fibres, tubes or ribbons. The characteristic length scale in these material is less than 100 nm, at least in one dimension. This thesis deals with porosity-free, three dimensional bulk nanomaterials, in which the grain size is less than 100 nm.

The materials used in the current study may be considered as a two-phase composite which contain an ordered crystalline phase and a somewhat disordered intercrystalline phase consisting of grain boundaries and triple junctions, Fig. 2.6 [Gleiter 1989]. Due to the small grain size in nanocrystalline materials, the volume fractions of atoms associated with grain boundaries and triple junctions (open circles in Fig. 2.6) are much greater when compared to polycrystalline materials.

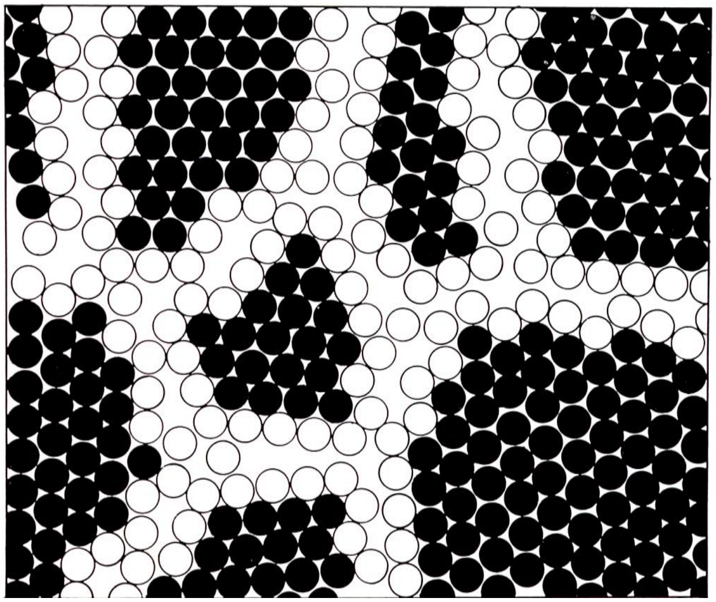

Figure 2.6: Schematic diagram of the atomic arrangement in nanocrystalline materials. The black circles represent the ordered structure, the grains; the open circles represent the disordered structure, the intercrystalline component [Gleiter (1989)].

To estimate the volume fraction of intercrystalline atoms, Palumbo et al. proposed a model by assuming that the grain shape is a fourteen-sided tetrakaidecahedron, Fig. 2.7a [Palumbo et al (1990)]. The hexagonal and square faces on every grain represent the grain boundaries, whereas the edges at which three grains are joined form the triple junctions. The following equations were derived to calculate the volume fractions of atoms associated with grain boundaries (v_{gb}), triple junctions (v_{tj}) and the total intercrystalline component (v_{ic}) [Palumbo et al. (1990)]:

Volume fraction of grain boundaries: $v_{gb} = \frac{[3\Delta(d-\Delta)^2]}{d^3}$ **(1)**

Volume fraction of triple junctions: $v_{tj} = v_{ic} - v_{gb}$ **(2)**

Total intercrystalline volume fraction: $v_{ic} = 1 - \left[\frac{d-\Delta}{d}\right]^3$ **(3)**

where d and Δ represent the grain size and grain boundary thickness, respectively. Fig. 2.7b displays a plot of volume fractions against grain size for a grain boundary thickness of Δ=1 nm. This figure shows that a grain size of 1000 nm yields an intercrystalline volume fraction of less than 1 %. With a decrease in grain size to 100 nm and 10 nm, the intercrystalline volume fraction increases to 3% and 30%, respectively. At very small grain sizes the volume fraction of triple junctions continues to increase, whereas the volume fraction of grain boundary begins to decrease as the grain size becomes less than 3 nm. The significance of Fig. 2.7 is that the somewhat disordered intercrystalline component becomes a very important structural defect of fully dense, 3-D nanomaterials at very small grain sizes.

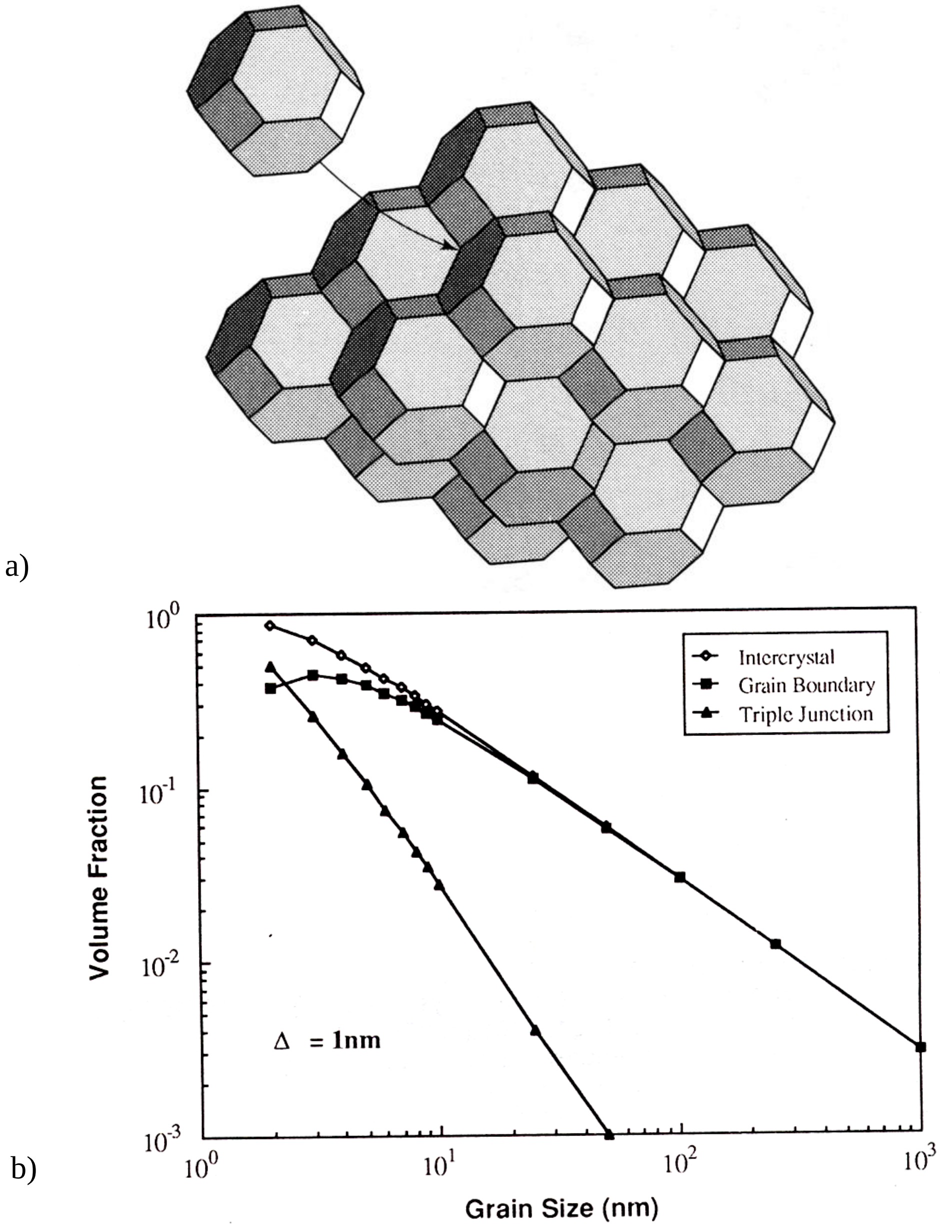

Figure 2.7: (a) The 14- sided tetrakaidecahedron grain shape, [Allen and Thomas (2003)] and (b) the volume fractions of total intercrystal components (V_{ic}), grain boundary (V_{gb}) and triple junctions (V_{tj}) as a function of grain size, [Palumbo et al. (1990)]

2.3 Properties of Electrodeposited Nanocrystalline Materials

In comparison with conventional materials, nanocrystalline materials as described in section 2.2, exhibit considerable changes in many properties, including strength, hardness [e.g. El-Sherik et al. (1992)], wear resistance, coefficient of friction [El-Sherik and Erb (1997)], hydrogen solubility and diffusivity [Doyle et al. (1995)], corrosion properties [Rofagha et al. (1991)] and thermal stability [Boylan et al. (1991)]. These properties are strongly depended on grain size and their enhancements are a direct result of grain refinement into the nanocrystalline regime. In the following section, the mechanical properties will be discussed in more detail.

2.3.1 Mechanical Properties of Nanocrystalline Materials

The mechanical strength and hardness of nanocrystalline materials are much higher than for polycrystalline materials. The relationship between grain size and strength/hardness is most commonly described by the Hall-Petch relationship as follows:

Yield strength: $$\sigma_y = \sigma_0 + k' d^{-0.5} \tag{4}$$

where σ_y is the yield strength of the material, σ_0 is the stress required to move an individual dislocation, k' is a material constant, and d is the average grain size of the material [Hall (1951), Petch (1953)]. A similar relationship is developed to express the effect of grain size on hardness,

Hardness: $$H_y = H_0 + k'' d^{-0.5} \tag{5}$$

Thus, by decreasing the grain size, significant gains in strength and hardness can be obtained. A hardness against grain size plot for electrodeposited nickel is shown in Fig. 2.8. The effect of grain size on hardness and strength can be understood when considering that grain boundaries and triple junctions are barriers to hinder dislocation motion in materials [Hall (1951), Petch (1953), Wang et al. (1995)]. With the reduction in grain size the volume fraction of the intercrystalline component increases, thus there is a greater number of barriers resulting from grain refinement which generate larger numbers of dislocation pile-ups [Palumbo et al. (1990)].

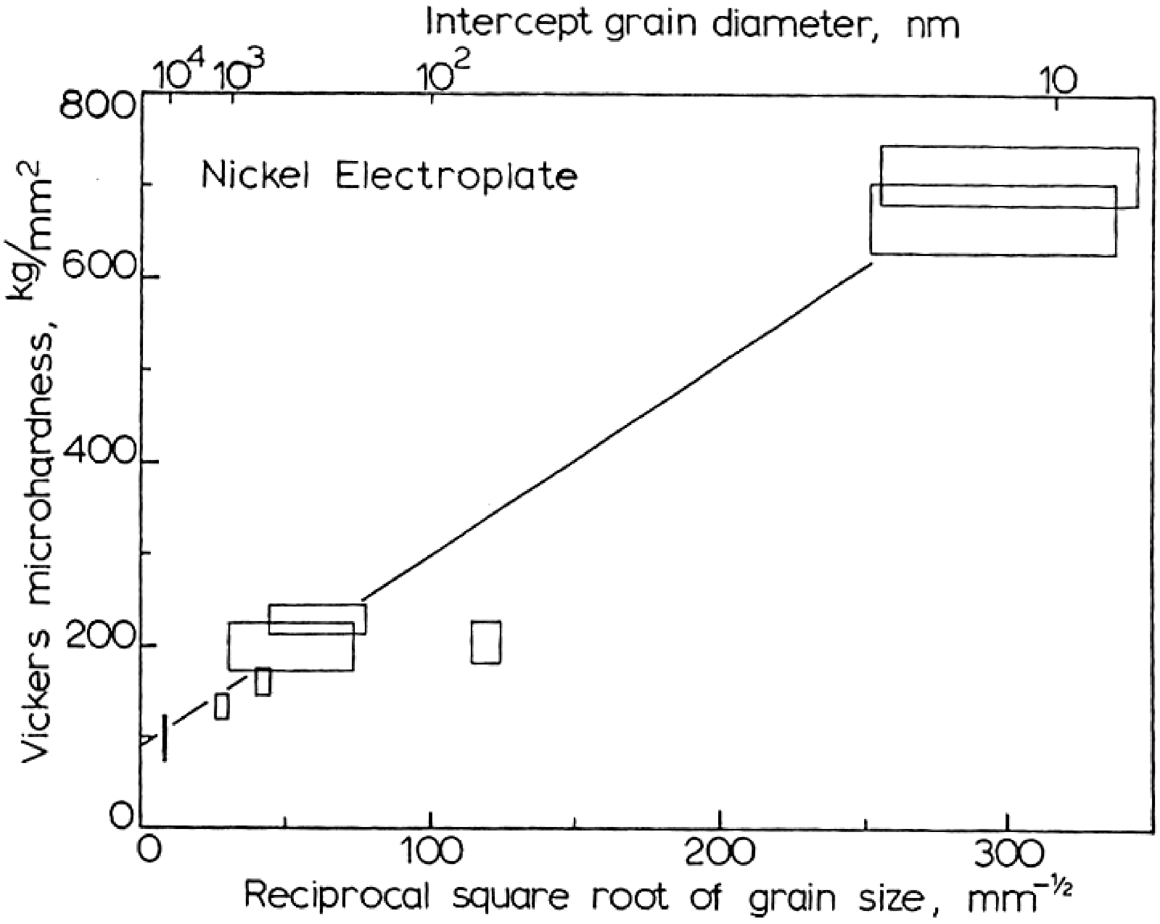

Figure 2.8: Plot of Vickers micro-hardness against one over square root of grain size, [Huges et al. (1896)]

2.4 Deformation Mechanisms in Nanocrystalline Materials

The primary deformation mechanisms for polycrystalline materials at low temperature are dislocation slip and twinning. To activate other mechanisms such as grain boundary sliding, grain rotation and diffusional mechanisms, higher temperatures and/or high stresses are required. In nanocrystalline materials, the volume fraction of intercrystalline defects is significantly higher than in polycrystalline structures. With the larger volume fraction of grain boundaries and triple junctions, deformation at room temperature is no longer controlled only by dislocation movement or twinning. Many previous studies have shown that plastic deformation in nanocrystalline materials at ambient temperature could be accommodated by diffusional creep, grain boundary sliding and grain rotation [e.g. Whang, (2011)], such as summarized in Fig. 2.9.

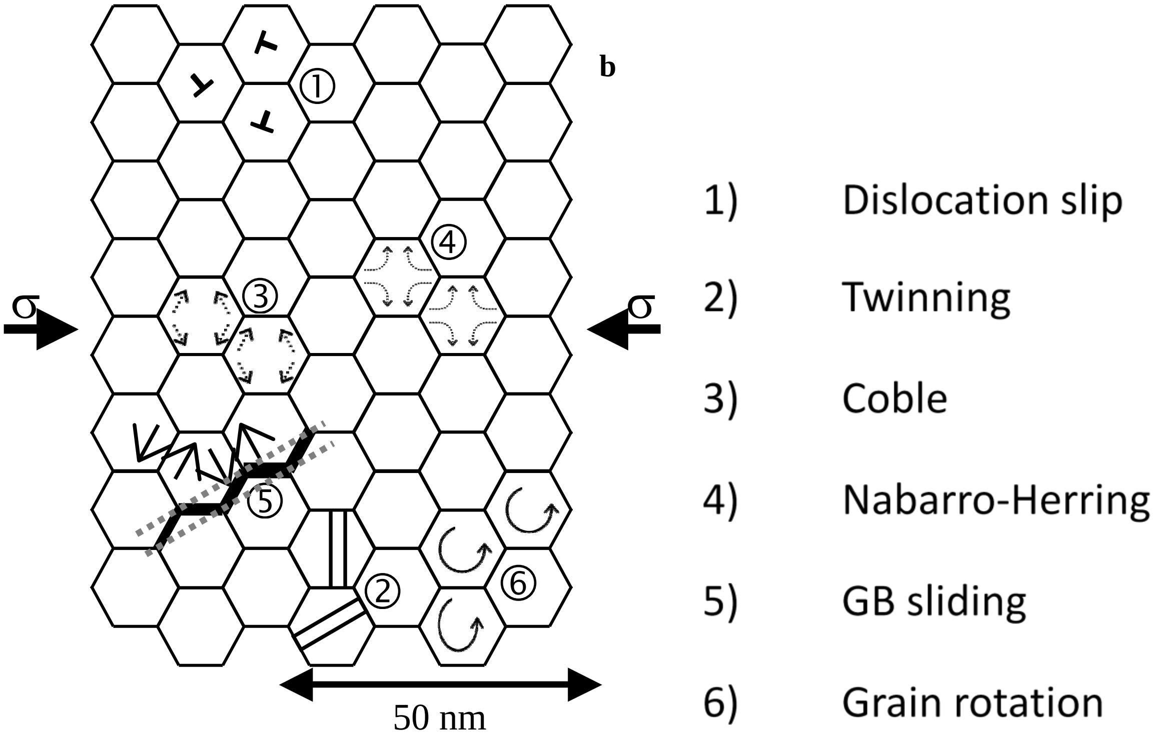

Figure 2.9: Low temperature deformation mechanisms in nanocrystalline metals, from [Erb et al. (2004)]

2.4.1 Grain Boundary Sliding and Grain Rotation

Grain boundary sliding is a macroscopic deformation mechanism where un-deformed grains slide over each other along their common boundaries. The original theory for polycrystals was presented by Gifkins and Snowden [1966] and later further developed by Ashby and Verall [1973]. This process is accommodated with other deformation mechanisms such as grain rotation and diffusional processes.

Gifkins and Snowden proposed that grain boundary sliding is induced by applied stress, where the adjacent grains slide in the opposite directions and the protrusions within the boundary move through lattice diffusion. Thus, protrusions within the grain boundaries hinder the rate of grain boundary sliding. As seen in Fig. 2.10a, under the applied stress, the top grain slides to the right and the bottom grain slides to the left. The rate of boundary sliding is reduced due to the movement of the protrusion, YX. As the grains slide over one another, the protrusion is under compressive stress at X and tensile stress at Y. The tension region has a higher concentration of vacancies than the compression region X. Thus, the tension region acts as a vacancy sink and the atoms in the compression region diffuse to the other side, thereby moving the protrusion towards the right.

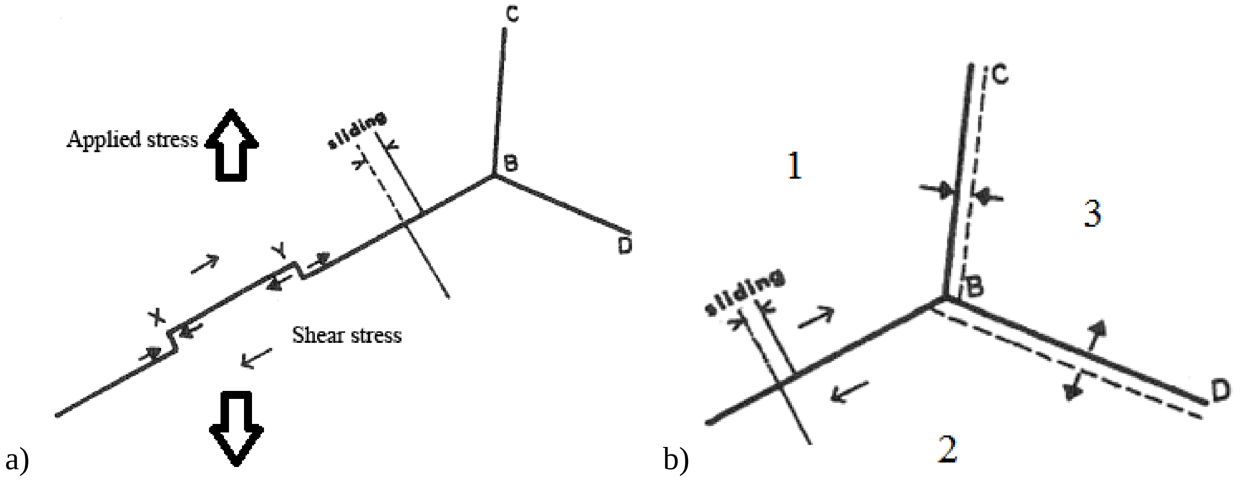

Figure 2.10: Schematic diagram of a) grain boundary sliding with a protrusion in the boundary, b) grain boundary sliding of the triple junction, Gifkins and Snowden [1966]

In 1968, Gifkins further developed the model and proposed that the rate determining step of grain boundary sliding is the diffusion around triple junctions, Fig. 2.10b. As stress is applied, grain number 1 moves to the right while grain number 2 moves to the left. This creates a compression stress on the BC boundary and a tensile stress on the BD boundary. Since boundary BD has a higher vacancy concentration than boundary BC, the atoms in BC diffuse to boundary BC, whereby boundary BC will slide to the right and boundary BD will slide to the left.

Ashby and Verral [1973] and Hahn et al. [1997] have proposed alternative models where grain boundary sliding is accommodated with diffusional mechanisms in polycrystalline and nanocrystalline materials, respectively. In Ashby and Verral's model, it is suggested that as one grain slides over another grain in polycrystalline materials, the local deformation on the adjacent boundaries accommodates changes through Coble and/or Nabarro-Herring creep. This allows the grains to remain wedged together and the rate determining step for this model is suggested to be the diffusion mechanisms, Coble and Nabarro-Herring creep.

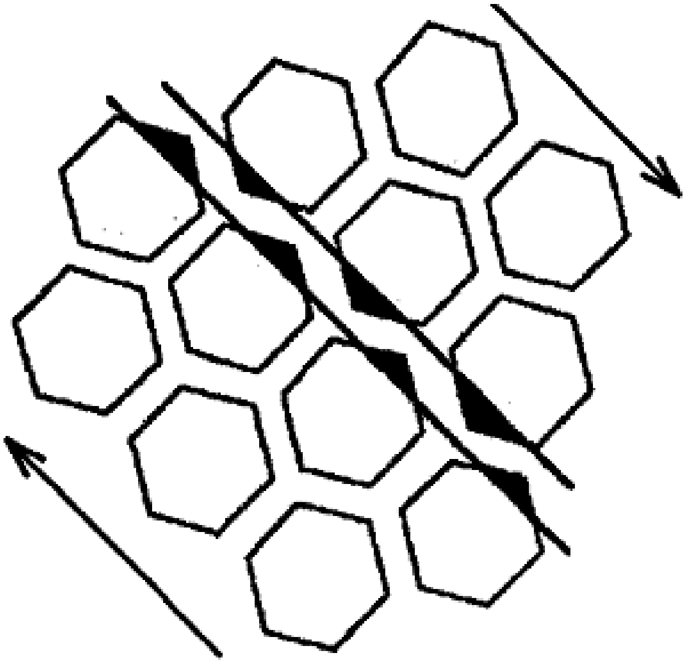

Figure 2.11: Schematic diagram of grain boundary sliding, proposed by Hahn et al. [1997]

The model developed by Hahn et al. [1997] is explicitly for grain boundary sliding in nanocrystalline materials, Fig. 2.11. By assuming all grains in a material have similar shape and size, Hahn et al. proposed that there's a macroscopic sliding plane (denoted by the black area between the parallel lines) between the non-deforming grains (denoted by the white area), in which these planes are activated to accommodate the deformation. Prior to sliding, deformation is accommodated through grain boundary diffusion (Coble creep) along the interfaces. The sharp edge of each grain is smoothened by diffusion to form the sliding plane. Grain boundary sliding can only occur after the applied stress overcomes a certain threshold value. Molecular dynamics simulations on sliding along grain boundaries were carried out by van Swygenhoven et al. [2001]. Their results showed that grain boundary sliding is the primary deformation mechanism in nanocrystalline materials. The sliding activity shown by the simulation is in support of Hahn's model where grain boundary sliding is facilitated by stress assisted atomic diffusion.

During grain boundary sliding, grain rotation can also occur simultaneously in which the grains turn in the direction of the shear stress [e.g. Murayama et al. (2006)]. The adjacent grains may rotate to a point where their orientations are closer to each other, which leads to softening. Murayama et al. suggested that grains can rotate by disclination motion, where a disclination is a line defect characterized by a rotation of the crystalline lattice around its line [Klimanek et al. (2001)] and the motion of disclination dipole is a combination of two disclinations which causes crystal lattices to rotate between them [Ovid'ko (2002)], Fig. 2.12.

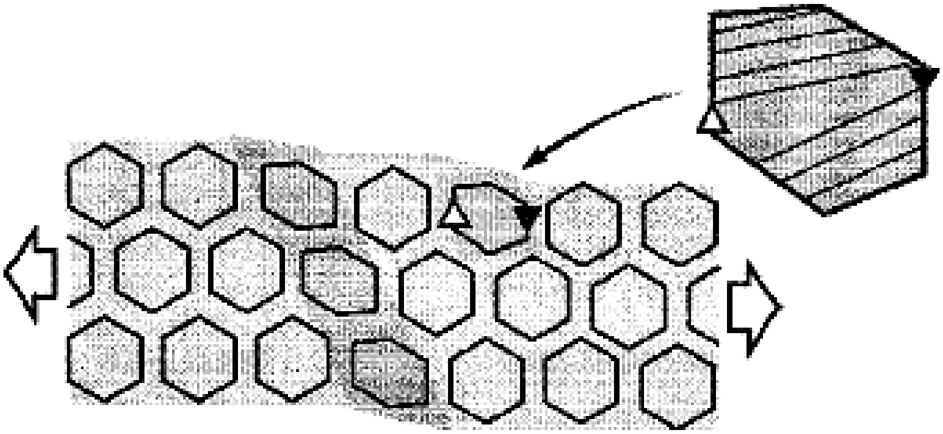

Figure 2.12: Schematic diagram of grain rotation of nanocrystalline material under tensile loading due to disclination dipole motion, as proposed by Ovid'ko [2002]

2.4.2 Nabarro-Herring Creep

Diffusion mechanisms for the deformation of polycrystalline materials were proposed by Nabarro [1948] and further developed by Herring [1950]. Self-diffusion within the grains of a polycrystalline material is driven by the applied shear stress. Vacancies within a grain can be created under compression or tension and they can move through grain boundaries or lattice diffusion. In the presence of tensile stress on a grain boundary, the energy needed for vacancy formation is reduced by the atomic volume multiplied by the applied stressed normal to the boundary. On the other hand, when a grain boundary experiences a compressive stress, the energy required for vacancy formation is increased by the same amount. Thus, the formation of vacancies at a grain boundary is more preferable under tensile stress than compressive stress and the annihilation of vacancies is the opposite. Diffusion of matter within the grain flows towards the vacancies, from the compression region towards the area under tension. Thus, in the presence of stress, there is a pressure gradient within the lattice and lattice defects such as vacancies move towards the direction which will relieve the inequality of pressure. The concentration of vacancies varies across the grain based on its shape and these vacancies move through the grain by lattice diffusion. Fig. 2.13 is a schematic diagram of a polycrystalline solid showing the macroscopic stress state. The directional flow of vacancies is shown by the arrows. Atoms and vacancies diffuse through the crystalline lattice to the grain boundaries, resulting in macroscopic deformation.

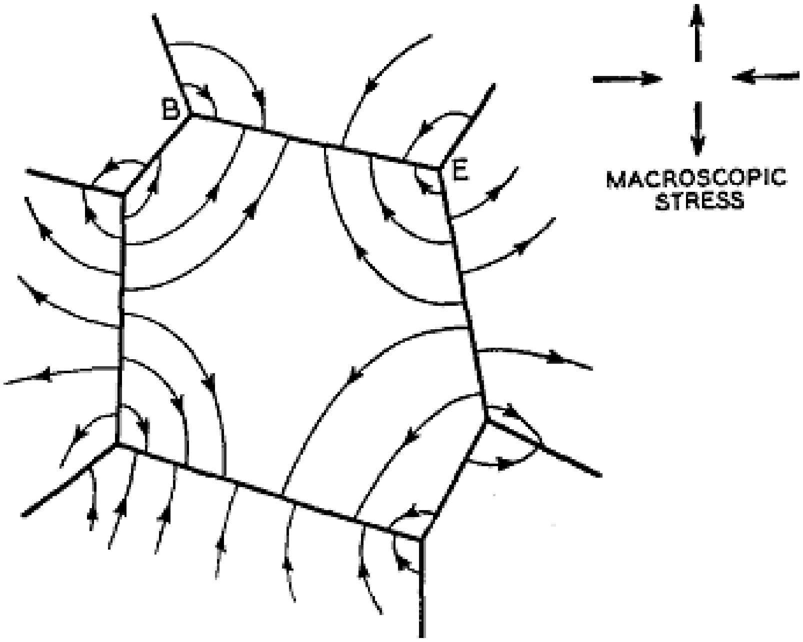

Figure 2.13: Nabarro-Herring vacancy diffusion mechanism through a grain during loading, Herring [1949]

2.4.3 Coble Creep

Another deformation mechanism through diffusion was proposed by Coble [1963]. Similar to Nabarro-Herring creep, Coble creep is a diffusion process that is induced by stress; however, the diffusion of vacancies/atoms occurs through grain boundaries instead of the crystal lattice. Coble proposed that the absorption and generation of vacancies is uniform along a given grain boundary; however, the various angles of planar grain boundaries with respect to the applied stress would affect the rate of the diffusion. Fig. 2.14 illustrates the flow in Coble creep. Under the opposing stress, σ_n, a vacancy concentration gradient arises between the boundaries. As shown in Fig. 2.14, two boundaries are under compressive stress while the other two boundaries are in tension; this leads to the diffusion of vacancies toward the boundaries under compressive stress and diffusion of atoms toward boundaries under tensile stress. Thus, the diffusive current is similar to Nabarro-Herring's model. As mentioned above, with the reduction in grain size to the nanocrystalline regime, the volume fraction of grain boundaries and triple junctions increases by a significant amount. Hence, it is likely that Coble creep becomes the dominant deformation mechanism as grain size decreases.

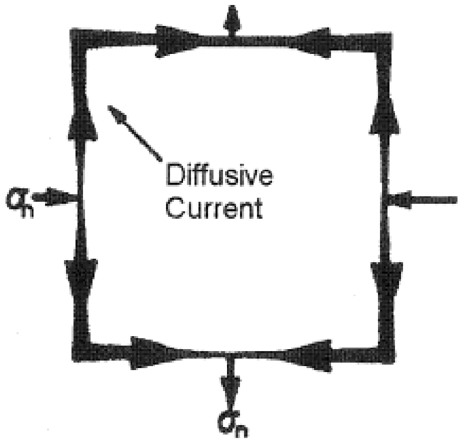

Figure 2.14: Coble vacancy diffusion mechanism along grain boundary during loading, Ashby [1969]

2.5 Strain Hardening in Polycrystalline and Nanocrystalline Materials

Strain hardening of polycrystalline materials is a result of the increase in dislocation interactions. Plastic deformation of polycrystalline materials can be separated into stages; in the early stage, there is a random distribution of few dislocations in the crystal structure. These dislocations can move along their slip planes with minimum interference from other dislocations. As plastic deformation continues, dislocation density increases due to dislocation multiplication which results in a decrease in mean free dislocation length [Kuhlmann-Wilsdorf (1989)]. With further deformation, the dislocation density increases even more and dislocations begin to pile up at strong obstacles such as grain boundaries; this impedes dislocation motion on their respective slip plane. Thus, the mobility of a dislocation is reduced and higher stress is required for further deformation. Most polycrystalline metals strain harden at room temperature. For example, Fig. 2.15 shows that the tensile strengths of copper, brass and 1040 steel increase significantly with increasing strain hardening, expressed here as percent cold work.

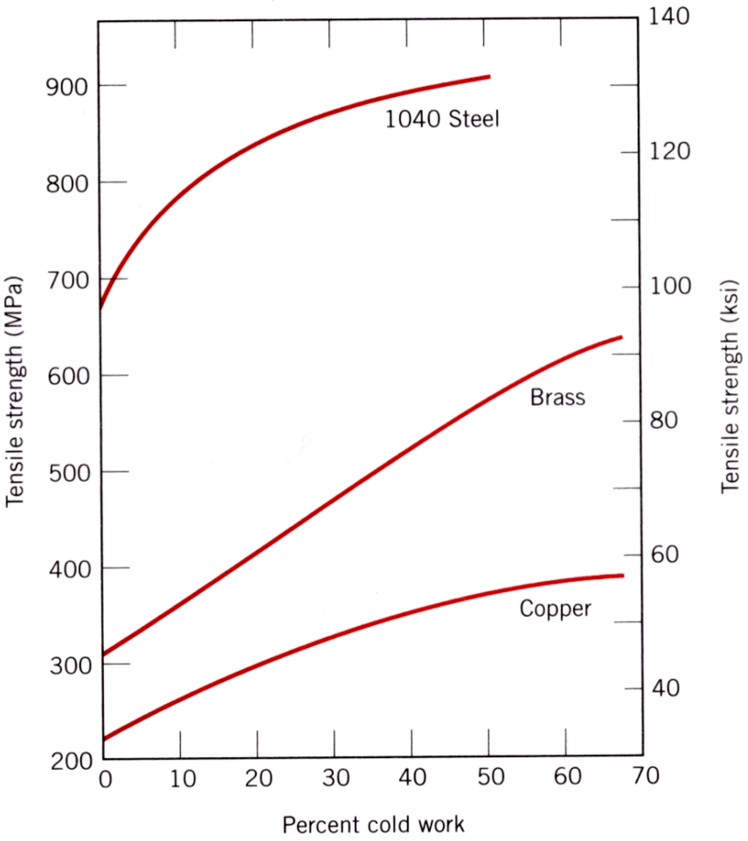

Fig. 2.15: The strain hardening behaviour of copper, brass and steel increase in tensile strength with increase in cold work [Callister (2005)].

A previous study done by Liang and Yu demonstrated the strain hardening affect in polycrystalline nickel [Liang and Yu (2008)]. Liang and Yu introduced strain into the material through cold rolling. The specimens were cold rolled in small increments and water quenching was used after each pass. The specimens were rolled to a strain of 80%, where strain, ε, was given as

$$\varepsilon = [(L_f - L_o)/L_o]x100\% \qquad \textbf{(6)}$$

where L_f and L_o are the final and initial lengths of the specimens. Vickers micro-hardness was measured for fully annealed Ni and at strains of ~10, 20, 40, 60 and 80%, respectively. The hardness value increased twofold from 1 GPa to over 2 GPa at 80% elongation, Fig. 2.16. The material had the highest strain hardening, between 0-20% elongation. With further deformation to 80% elongation, the strain hardening rate was reduced.

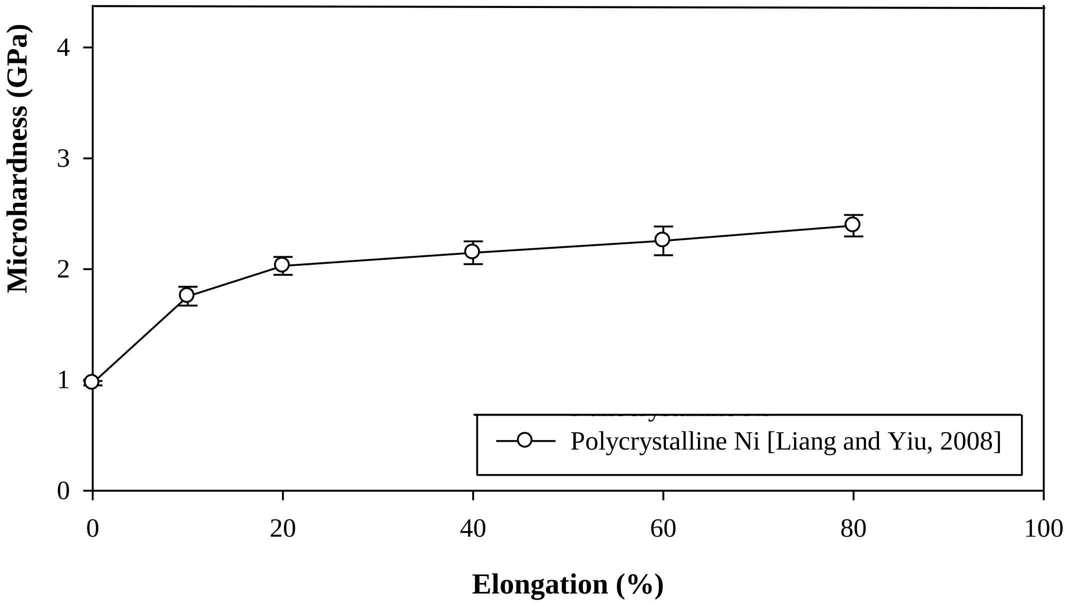

Figure 2.16: Plot of Vickers micro-hardness against elongation for as-received and cold-rolled polycrystalline nickel [Liang and Yu, (2008)]

Since strain hardening is due to dislocation-dislocation interactions, in order to form a dislocation pile-up against grain boundaries, at least two dislocations are needed [Callister (2005)]. Nieh and Wadsworth proposed that dislocation pile-ups can only be generated within a grain that is over a critical size [Nieh and Wadsworth, (1991)]. When grains are below the size where two dislocations cannot co-exist within the same slip plane within one grain, dislocation mechanisms may not be suitable to interpret the deformation behavior. Eshelby's analysis of the critical distance between two dislocations provides an estimate of the lower and upper limits of grain size for dislocations to form a pile-up within a grain [Eshelby et al. (1951)]. The critical distance, d_c, between two dislocations is given by,

$$d_c = \frac{Kb}{2\pi\tau_c} \qquad \textbf{(7)}$$

where τ_c is the critical shear strength, b is the Burgers vector of the dislocation and K is the energy factor. Since the variables K and b are material constants, the distance between two dislocations is determined by the shear strength. To estimate the lower limit of grain size, theoretical shear strength, τ_{max}^{th}, which is the highest shear stress the material can with-stand, is used. The upper limit is estimated by using the Peierls-Nabarro force, τ_{p-n}, the lowest shear stress required to move a single dislocation. Peierls-Nabarro force is expressed as,

$$\tau_{P-N} = \frac{G}{(1-\nu)} e^{-2\pi W/b} \qquad \textbf{(8)}$$

where G is the shear modulus, W is the width of the dislocation, b is the burger's vector and ν is the Poisson's ratio. A previous study by Wang et al. [Wang et al. (1994)] has calculated the critical distances for copper and nickel, given as $(d_c)_u$ and $(d_c)_L$ in Table 2.1. Thus, the smallest distance that two dislocations can be brought together without pushing them away in an infinite crystal are 39.4nm and 25.6nm for the upper limits and 1.2 and 1.3 nm for the lower limits for copper and nickel, respectively.

Table 2.1: Upper and lower limits for critical distance between two dislocations

Crystal	K (GPa)	τ_{max}^{th} (GPa)	τ_{p-n} (GPa)	b (nm)	$(d_c)_U$ (nm)	$(d_c)_L$ (nm)
Cu	78.2	1.54	1.91	0.286	39.4	1.2
Ni	126	3.71	3.71	0.275	25.6	1.3

Previous studies on the strain hardening capacity of nanocrystalline nickel were carried out by Wang et al. [1994], Kulovits et al. [2008], Zabev [2008] and Wu et al. [2009]. In these studies, different methods such as tensile deformation and rolling were used to introduce strain into the specimens. In the studies by Zabev and Wu et al. samples of electrodeposited nanocrystalline nickel were used. Plastic deformation was introduced into the specimens through cold rolling; however, there is a considerable discrepancy between their results. Zabev obtained samples of electroplated nanocrystalline from Integran Technologies, Inc. with a grain size of 29 nm. After characterizing the as-received materials, the specimens went through cold-rolling in small increments (1-5 µm thickness reduction per pass and water quenched after each pass). Zabev's strain calculation were also based on the elongation of the sample in terms of length as given in equation 6. Vickers micro-hardness was measured at different strains from 0% to 80%. It was found that the hardness values fluctuated only slightly (Fig. 2.17), approximately by 7%, as compared to polycrystalline nickel, which exceeded 100% in the initial stage, Fig. 2.16 and also shown in Fig. 2.17 for comparison.

In contrast, Wu et al. [2009] reported significant yield strength increases for cryogenically deformed nanocrystalline nickel electrodeposits with an initial grain size of 20 nm, Fig. 2.18. Rolling strain was defined as

$$\varepsilon = \ln\left(\frac{t_i}{t_f}\right) \qquad \textbf{(9)}$$

where t_i and t_f are the initial and final sample thickness, respectively. Fig. 2.18 is a plot of yield strength against rolling strain, which illustrates a sharp rise in yield strength, from 1400 MPa to ~2300 MPa, with increasing rolling strain to 0.5. For higher strains the yield strength decreased to an intermediate value of ~1900 MPa.

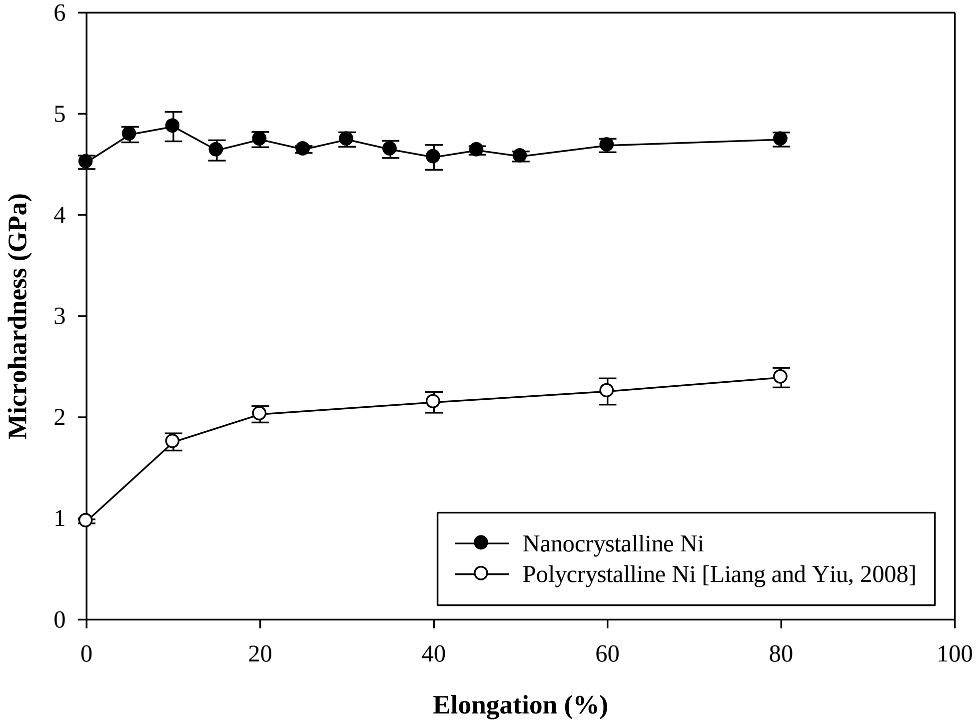

Figure 2.17: Plot of Vickers micro-hardness against elongation for as-received and cold rolled polycrystalline and nanocrystalline nickel [Zabev, (2008)]

The hardness against elongation plot obtained by Zabev, Fig. 2.17, led to the suggestion that the strain hardening capacity of electroplated nanocrystalline nickel is low due to their inability to accumulate dislocations. In contrast, strong strain hardening under large plastic deformation was observed by Wu et al. In view of this discrepancy regarding strain hardening effects in nickel as a function of grain size, one part of this thesis will use a different experimental approach to compare strain hardening in polycrystalline and nanocrystalline nickel based on hardness indentations. This will be explained in more detail in section 4.3

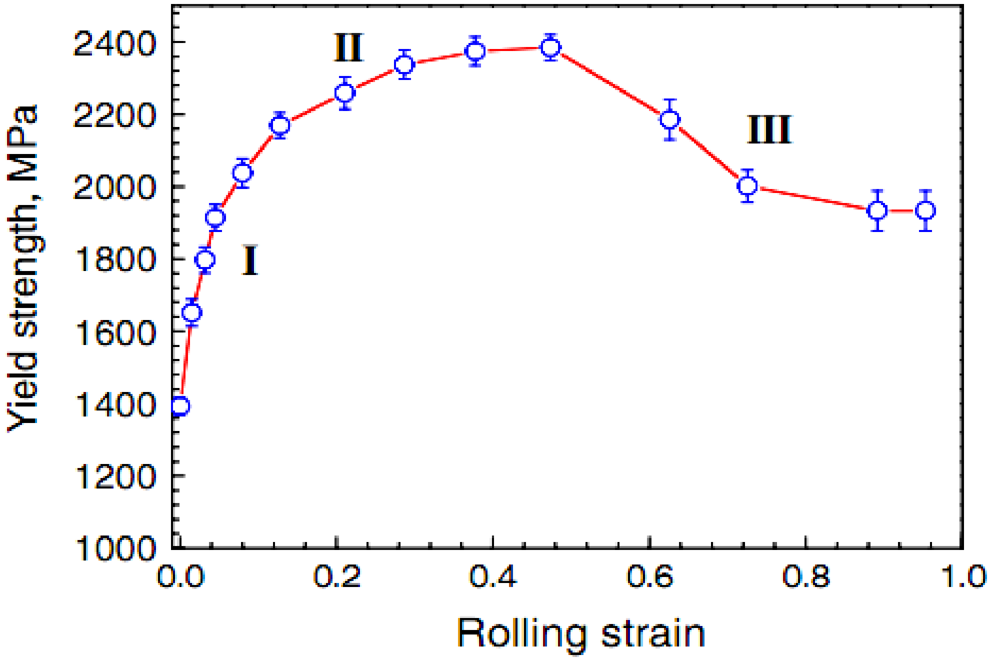

Figure 2.18: Plot of yield strength against rolling strain, where yield strength is determined by one third of Vickers micro-hardness relationship [Wu et al. (2009)]

2.6 Hardness

Hardness is a mechanical property that is often used to for comparison between different materials. The hardness of a material is defined as the material's resistance to localized plastic/permanent deformation [Callister (2005)]. One group of tests used to determine hardness are known as static indentation tests, where an indenter with the geometry of a ball, pyramid, or diamond cone is pressed into the surface of the material being tested. The hardness is either determined from the total test force to the penetration depth or the indentation area. Common static indentation tests include Rockwell, Vickers, Brinell and Knoop hardness tests [Callister (2005)].

2.6.1 Rockwell and Superficial Rockwell Hardness

Rockwell hardness is classified as a penetration method, Fig. 2.19. The principle of the test can be divided into three steps: first, a minor load is applied to establish a reference point, and then a major load is applied and held for a specified dwell time. Lastly the major load is removed and the final depth of indentation is measured. The initial minor load eliminates the effects of backlash in the measuring system and surface roughness which could lead to potential measuring errors. There are two types of Rockwell hardness tests: Superficial Rockwell and Rockwell. The difference between the two is the load selections for specimens with different thickness and test locations. For Superficial Rockwell, the reference point is set by a minor load of 3kgf, and major loads of 15, 30, or 45 kgf, respectively. On the other hand, the minor load in Rockwell testing is 10kgf, and the major loads are 60, 100, or 150 kgf. The selection of indenter is determined by the type of material to be tested and the scale limitations; for testing hard materials the 120° sphero-conical diamond indenter is utilized to avoid plastic deformation of the indenter during the test. Hardened steel ball indenters with diameter of $\frac{1}{16}, \frac{1}{8}, \frac{1}{4}, \frac{1}{2}$ inches are used for testing softer materials.

The hardness value is derived from the differences in the two indentation depth measurements, h in mm, Fig. 2.19, where the Superficial Rockwell hardness value is given as,

$$Rockwell\ Superficial\ hardness = 100 - \frac{h}{0.001} \qquad \textbf{(10)}$$

On the other hand, the Rockwell hardness value is given as,

Ball indenter:

$$Rockwell\ hardness = 130 - \frac{h}{0.002} \qquad \textbf{(11)}$$

Diamond cone indenter:

$$Rockwell\ \ hardness = 100 - \frac{h}{0.002} \tag{12}$$

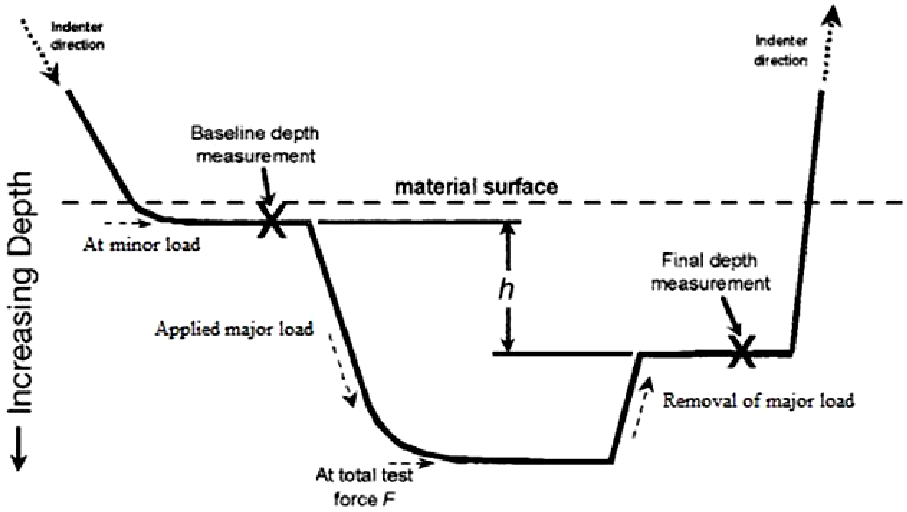

Figure 2.19: Schematic diagram of the cross section of Rockwell hardness measurement, modified [ASTM E18 – 08, (2008)]

2.6.2 Brinell Hardness

Brinell hardness testing is another static hardness test which utilizes the indentation depth to determine the hardness of materials. The test consists of applying a load between 500 to 3000 kgf for a specific dwelling time usually between 10 to 30 seconds using a hardened steel or tungsten carbide ball with a diameter of 5 or 10 mm. Once plastic deformation is introduced into the testing specimen, the resultant recovered round impression is measured in millimeters using a low power microscope. Hardness is determined by taking the mean diameter of the indentation, the hardness number (HB) is given as,

$$HB = \frac{2P}{\pi D[D - \sqrt{D^2 - d^2}]} \tag{13}$$

where P is the load in kg; D is the diameter of the indenter in mm; and d is the diameter of the indentation in mm.

2.6.3 Vickers and Knoop Hardness

Vickers and Knoop micro-hardness are static indentation tests which utilize the area of the indentation to provide the measure of hardness. The hardness test involves indenting a diamond indenter of specific geometry into the surface of the test specimen at loads ranging from 1 to 1000 grams force. Both methods are used to determine the hardness of material geometries that are too small to be measured by conventional macroscopic methods. The differences between Vickers and Knoop hardness test is the geometry of the indenter, Fig. 2.20. The Vickers indenter is a square based pyramidal diamond with a face angle of 136°, while the Knoop indenter is a rhombic based pyramidal diamond shape. The long to short diagonal ratio for the Knoop indenter is about 7 to 1 with a longitudinal angle of 172° and a 130° transverse angle. With the difference in indenter geometry, Vickers indenter penetrates into the specimen about twice as far as compared to Knoop indenter; thus, the Vickers hardness test is less sensitive to surface conditions than the Knoop test.

The hardness value for both Vickers and Knoop is a stress value with units of kilograms per millimeter square. It is determined by the ratio of the applied load, P, to the unrecovered projected area of indentation, A.

$$\text{Hardness} = P / A \qquad \textbf{(14)}$$

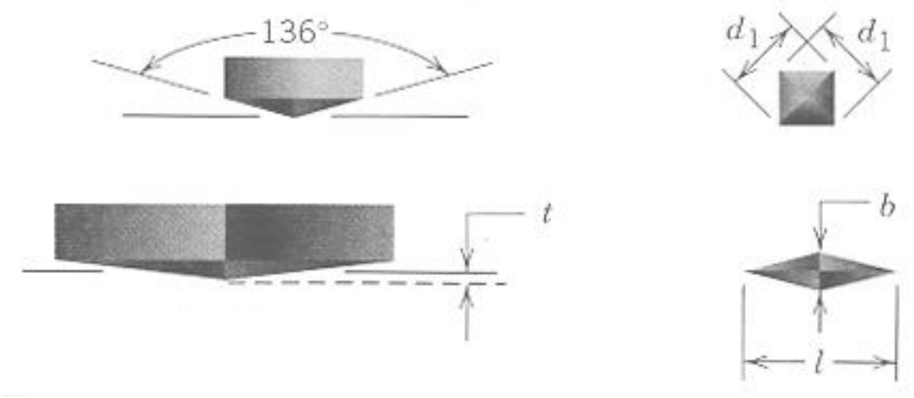

Figure 2.20: Schematic diagrams of the indenter and indentation of Vickers and Knoop hardness [Callister (2005)].

Vickers and Knoop hardness values are designated as HV and HK, respectively. The formula for Vickers hardness (HV) is given as,

$$HV = 1.854\,\frac{P}{d_1^2} \qquad \textbf{(15)}$$

where P is the applied load in kgf; d is the mean diagonal of the indentation in mm;. The Knoop hardness value (HK) is expressed as,

$$HK = 14.2\frac{P}{l^2} \qquad \textbf{(16)}$$

where P is the applied load in kgf; l is the measured length of the long diagonal in mm. Since the width of the Knoop indenter is much thinner, it is often used to measure hardness on the cross-sections of thin coatings.

2.6.4 Nanoindentation Hardness

Nanoindentation is a very popular technique used for studying the mechanical properties of solids in submicrometer or nanometer size regions [e.g. Oliver et al. (1986)]. Similar to Vickers hardness, nanoindentation hardness measures the load over a projected residual area of the indentation. The hardness test involves indenting the so-called Berkovich indenter into the surface of the test specimen, Fig. 2.21.

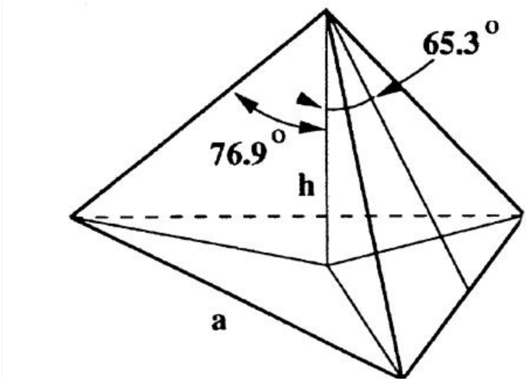

Figure 2.21: Schematic diagram of the Berkovich indenter

Since the projected residual area of the indent is correlated with penetration depth, as the load is applied the depth of penetration is measured and the area of contact is determined by the depth of the impression and the known angle of the Berkovich indenter. The nanoindentation hardness value is expressed as,

$$H = {}^{P}\!/_{24.5h_p^2} \quad \textbf{(17)}$$

where H is the hardness value measured by nanoindentaiton, P is the applied load and h_p is the measured displacement. With the smaller indentations, nanoindentation is often used to measure mechanical properties of coatings and thin films.

2.6.5. Summary of Hardness Tests

For a quick comparison, the various hardness tests described in sections 2.6.1 - 2.6.4 are summarized in the following table giving details on the indenter and the equations for the various tests.

Table 2.2 Summaries of the static hardness indentation tests

Test	**Indenter**	**Formula for Hardness Number**
Rockwell and Superficial Rockwell Hardness	Diamond cone; $\frac{1}{16}, \frac{1}{8}, \frac{1}{4}, \frac{1}{2}$ in. steel spheres	Rockwell Hardness: $Ball\colon\ Rockwell\ hardness = 130 - \frac{h}{0.002}$ $Diamond\colon\ Rockwell\ hardness = 100 - \frac{h}{0.002}$ Superficial Rockwell Hardness: $Rockwell\ Superficial\ hardness = 100 - \frac{h}{0.001}$
Brinell	10 mm sphere of steel or tungsten carbide	$HB = \frac{2P}{\pi D[D - \sqrt{D^2 - d^2}]}$ Where P is load, kg; D is sphere diameter, mm; d is diameter of the indentation, mm.
Vickers micro-hardness	Vickers diamond pyramid	$HV = 1.854\ \frac{P}{d_1^2}$ Where P is load, kgf; d is the mean diagonal of the indentation, mm
Knoop micro-hardness	Knoop diamond pyramid	$HK = 14.2\frac{P}{l^2}$ Where P is the applied load, kgf; l is the measured length of long diagonal, mm.
Nanoindentation hardness	Berkovich diamond pyramid	$H = {}^{P}/_{24.5h_p^2}$ Where P is the applied load, and h_p is the measured displacement of penetration depth

2.7 Hardness Conversion Relationship

Hardness conversion tables for metals such as copper, steel and nickel can be found in ASTM standard E140 - 07. Equations describing the relationships between Brinell, Vickers, Rockwell and Knoop hardness for different metals are generated empirically from the hardness numbers contained in the tables. The hardness conversion tables for nickel and high-nickel alloys can be found in the appendix. ASTM suggested that these hardness conversion tables and relationships are intended for nickel and high-nickel alloys, where the nickel content is over 50 %, and particularly for nickel-aluminum-silicon specimens. To cover the large range of hardness values, these alloys were in their annealed to heavily cold-worked or age-hardening conditions, including intermediate conditions. However, a Rockwell/Superficial Rockwell to Vickers hardness conversion table and relationship has yet to be developed for polycrystalline and nanocrystalline nickel in which strengthening is solely due to grain size refinement.

2.8 Objectives of this Research

As mentioned in the previous chapter, in industry hardness values are commonly reported in terms of Rockwell hardness value. However, in the past most of the hardness measurements for nanocrystalline metals were limited to Vickers micro-hardness and nano-indentation hardness tests, mainly due to sample size/thickness limitations which did not permit the application of the Rockwell method. Hardness conversion relationships for various hardness scales and materials can be found in ASTM standards. For nickel the hardness relationship are based on the materials in which the strengthening mechanism were through alloying, annealing, cold working, and age hardening. However, there is no Vickers-Rockwell hardness conversion for polycrystalline and nanocrystalline nickel, in which the strengthening mechanism is mainly due to grain size refinement. The first objective of this thesis is to establish such a relationship for nickel covering a wide range of grain sizes.

With respect to strain hardening of nanocrystalline nickel electrodeposits, there are conflicting results reported in the literature. Some studies have concluded that strain hardening decreases with decreasing grain size on the basis of tensile test results [Wang et al. (1997)], others studies found very little to no strain hardening when strain was introduced through cold rolling [Kulovits et al. (2008) and Zabev et al. (2008)]. In contrast, Wu et al reported significant strain hardening capacity on the basis of relatively large yield strength increases for cryogenically deformed nanocrystalline nickel. In view of these conflicting results regarding strain hardening effects in nickel as a function of grain size, the second objective of this study was to use a different experimental approach to compare strain hardening in polycrystalline and nanocrystalline nickel based on hardness indentation measurements.

3.0 Materials and Experimental Methods

The goal of this study is to investigate hardness scale conversions and the strain hardening behaviour in localized deformation zones for nanocrystalline nickel. This section details the procedures followed in sample preparation, materials characterization and the different types of hardness measurements for polycrystalline and nanocrystalline nickel.

3.1 Materials and Sample Preparation

Eight specimens of nickel with different grain sizes and hardness were used to determine the relationship between the Rockwell/Superficial Rockwell hardness scales and the Vickers micro-hardness. The grain sizes of these specimens ranged from polycrystalline down to nanocrystalline. The polycrystalline metal samples were commercially available Ni-200 samples while the electrodeposited nanocrystalline nickels were provided by Integran Technologies Inc.. Several nanocrystalline samples contained some iron or phosphorus alloying additions. However, from previous studies, it is known that the strengthening mechanism of these materials comes mainly from grain size reduction and not solid solution hardening [Erb et al. (1996)]. For Rockwell/Superficial Rockwell hardness testing, the samples were electroplated with thicknesses between 0.6 mm to 1 mm in accordance with ASTM standard (E18-08) for Rockwell hardness testing of materials.

To investigate the effect of grain size on strain hardening, four lots of nickel were selected, and these materials were chosen from the two extreme ends of the grain size range. The work hardening behaviour of these materials was studied under a localized plastic zone, which was inducted into the specimens through large Rockwell hardness indentations. An ASTM standard Rockwell scale D, 120° diamond cone indenter at 100kgf of load, and a Rockwell scale B, ball indenter at 100kgf of load, were used to introduce macro-indents on each specimen. Subsequently, the specimens were sectioned near the Rockwell indentation followed by cold mounting into epoxy. Grinding and polishing were used to expose the cross-section of the indentation. To reduce residual stresses introduced during grinding and polishing, standard LECO's metallographic polishing procedures using progressively finer polishing media were utilized. To determine the changes in hardness due to the localized deformation in the plastic zone, hardness profiles along direction, x, away from the Rockwell indentation were measured using a much smaller Vickers micro-hardness indentations, Fig. 3.1. For higher resolution of hardness closer to the Rockwell indent, nano-indentation hardness contours were also carried out for the smallest grained nickel. Similar to Vickers micro-hardness, the sample surface preparation was as per ASTM standard (E2546-07) for nano-indentation.

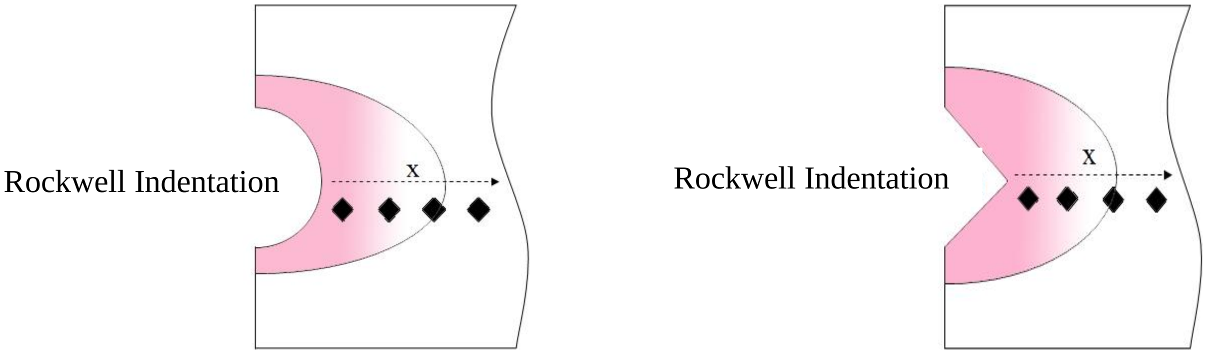

Figure 3.1 Schematic diagram of the cross sections below the Rockwell indentations. Vickers micro-hardness profiles were measured along direction x.

3.2 Material Characterization

3.2.1 Energy-Dispersive X-ray Spectroscopy (EDX)

The compositions of the materials were determined by energy-dispersive X-ray spectroscopy (EDX) in a conventional Hitachi S-570 field emission scanning electron microscope (SEM), at an acceleration voltage of 20 kV. The specimens were prepared by wet-grinding and a total of three measurements were made on each specimen using the area mode to analyze large areas (~100 x 100 µm) on the specimens.

3.2.2 Grain Size Analysis

3.2.2.1 Transmission Electron Microscopy (TEM)

To investigate the microstructures and grain sizes of the nanocrystalline specimens, bright field and dark field images and selected area diffraction patterns (SADP) were required. For this analysis, a Philips CM12- LaB_6 TEM, with an operating accelerating voltage of 200kV was utilized. To prepare the TEM specimens, the bulk materials were mechanically ground and polished down to a thickness of approximately 100 µm. Subsequently, 3 mm discs were mechanically punched out (Gatan sample punch) for further preparation. To create the thin electron transparent area, the 3 mm discs were electropolished using a Struers TenuPol-5 twin-jet electropolisher. The electrolyte used consisted of 90% methanol and 10% perchloric acid and the temperature was kept between -40ºC to -50ºC with liquid nitrogen cooling. The polishing was achieved at a voltage of 15V, at 74-95mA current density for 1 minute and 15 seconds per disk. The average grain sizes were calculated from grain measurements on dark field images using ImageJ. An average of at least 200 grains were measured per specimen.

3.2.2.2 Optical Imaging of Polycrystalline Microstructure

To determine the average grain size of the polycrystalline materials, an etching solution was chosen from LECO Metallography Handbook to reveal the grain structure for nickel [LECO (2011)]. The etching solution consisted of 10g $CuSO_4$, 50 ml HCl and 50 ml H_2O. The specimens were ground, then polished with 1µm diamond paste and subsequently immersed into the solution at room temperature for 1 min to 30 seconds to obtain the desired contrast. The average grain sizes were calculated from the grain measurements on optical micrographs using ImageJ. Again, an average at least 200 grains were measured per specimen.

3.3 Mechanical Testing

3.3.1 Rockwell Hardness Testing

Rockwell hardness values for the specimens were measured on a Buehler Macromets 5100TA Rockwell and Rockwell Superficial hardness indenter. Rockwell hardness scales A, B, D and F, which use either the 120 ° degree diamond cone or the $\frac{1}{16}$ inch diameter steel sphere at loads of 60 and 100 kilogram, and the Superficial Rockwell hardness scale with loads of 15, 30, 45, were used (see Table 2.2), respectively. The hardness measurements were taken in accordance with the ASTM E18-8 standard, where the thickness of the specimens must be ten times greater than the indentation depth. To determine the average hardness for each Rockwell hardness scale, 5 measurements were made on each specimen.

3.3.2 Vickers Micro-hardness Testing

Vickers micro-hardness measurements were taken for all as-received materials by following ASTM standard E384-99. A Buehler Micromet 5103 Microhardness Tester was used to measure the hardness. Five hardness measurements at 1kg load and 10 seconds loading time on each sample were made to determine the average hardness. To obtain the hardness profile underneath the macro indentations, Vickers micro-hardness value were measured with an applied load of 100g and a dwelling time of 10 seconds. As per ASTM standard for Vickers hardness testing, the indentation spacing was a minimum of 100µm apart to avoid strain hardening effects from neighbouring indents.

3.3.3 Nanoindentation Hardness Testing

Nanoindentation hardness measurements were done on a Shimadzu DUH-W201S nanoindenter. To obtain a reference hardness measurement, a total of ten measurements were taken on the specimens to determine the average hardness value and then three series of hardness profile were measured away from the bottom of the macro indent (see Fig. 3.1). The hardness values were calculated with Oilver-Pharrr method. Indentations were made using an applied load of 110mN with the loading time of 10 seconds for 4 cycles. To minimize sample drift during the test, stabilization was implemented prior the measurements to avoid potential drifts of the specimen or the stage. To stabilize the set up, a cycle of four indentations were made with a force of 100 mN for 600 seconds. As per ASTM standard for nanoindentation hardness testing (ASTM E2546-07), the indentation spacing was a minimum of 2 indentations to avoid strain hardening effects from neighbouring indents.

4.0 Results and Discussion

4.1 Characterization of Materials

4.1.1 Grain Size Analysis

The grain size of the polycrystalline material was determined from the examination of optical micrographs, whereas the average grain sizes of the nanocrystalline materials were determined from measurements on TEM micrographs. In Fig. 4.1 to 4.4, an example of an optical micrograph with a histogram of the grain size distribution, log grain size distribution and cumulative volume fraction curve for the polycrystalline nickel (Ni 1) are shown. Optical micrographs for polycrystalline nickel (Ni 1) at 50 times and 100 times magnifications were used for grain size analysis. By measuring the size of 340 grains, the average grain size was determined to be 161 μm with a standard deviation of ± 52 μm. The plot of frequency versus grain size, where log-normal distribution is superimposed onto the graph shows that the grains are distributed log-normally (Fig. 4.3).

Structural investigation of the ultra-fine grained and nanocrystalline nickel were performed through the use of TEM micrographs. The analysis of specimen Ni 4 and Ni 6 are shown here as examples. Bright field and dark field TEM images along with the corresponding selected area diffraction pattern (SADP) for the ultra-fined grained nickel are shown in Fig. 4.5. From the TEM images, grains in the micrometer and nanometer ranges are observed and through grain size measurements, the average grain size was determined to be 61 nm with a standard deviation of ± 29 nm (Fig. 4.6). The plot of frequency versus grain size with the log-normal distribution curve superimposed on it, Fig. 4.7, again shows that the grains are distributed log-normally.

In addition, for one of the nanocrystalline nickel, Ni 6, the bright field and dark field micrographs along with the corresponding diffraction pattern are shown in Fig. 4.9. The histogram of the grain size distribution, log grain size distribution and cumulative volume fraction curve for this sample are shown in Fig. 4.9 - 4.12. The grain size measurements were carried out on the dark field images; the average grain size for this material was 19 nm with a standard deviation of ± 7 nm. The plot of log-normal distribution shows that the grains are also distributed normally.

Grain size analysis on specimens Ni 2, Ni 3, Ni 5 and Ni 7 were previously studied in the group [Erb et al. (2007) and Zabev (2008)]. The optical and transmission electron microscopy images confirmed that indeed a large range of grain sizes for nickel were examined in this study. The average grain sizes for all materials used for subsequent hardness testing are presented in Table 4.1.

Table 4.1 Average grain sizes of the specimen used in this experiment

Sample	**Average Grain Size**
Ni 1	161 µm (Poly)
Ni 2	540 nm (Ultrafine)
Ni 3	318 nm (Ultrafine)
Ni 4	61 nm (Nano)
Ni 5	29 nm (Nano)
Ni 6	19 nm (Nano)
Ni 7	8 nm (Nano)

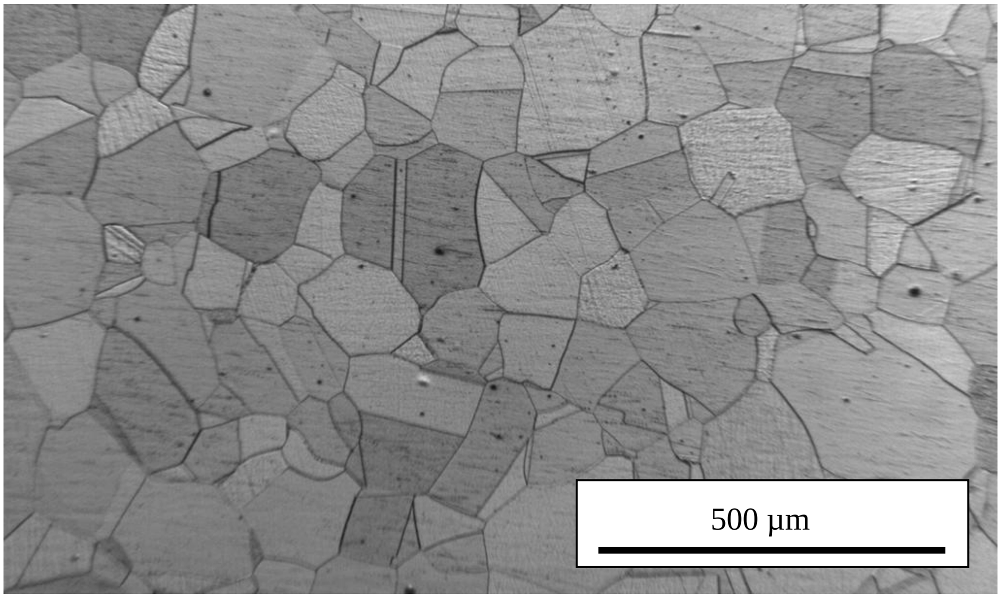

Figure 4.1: Optical micrograph of polycrystalline nickel, Ni 1

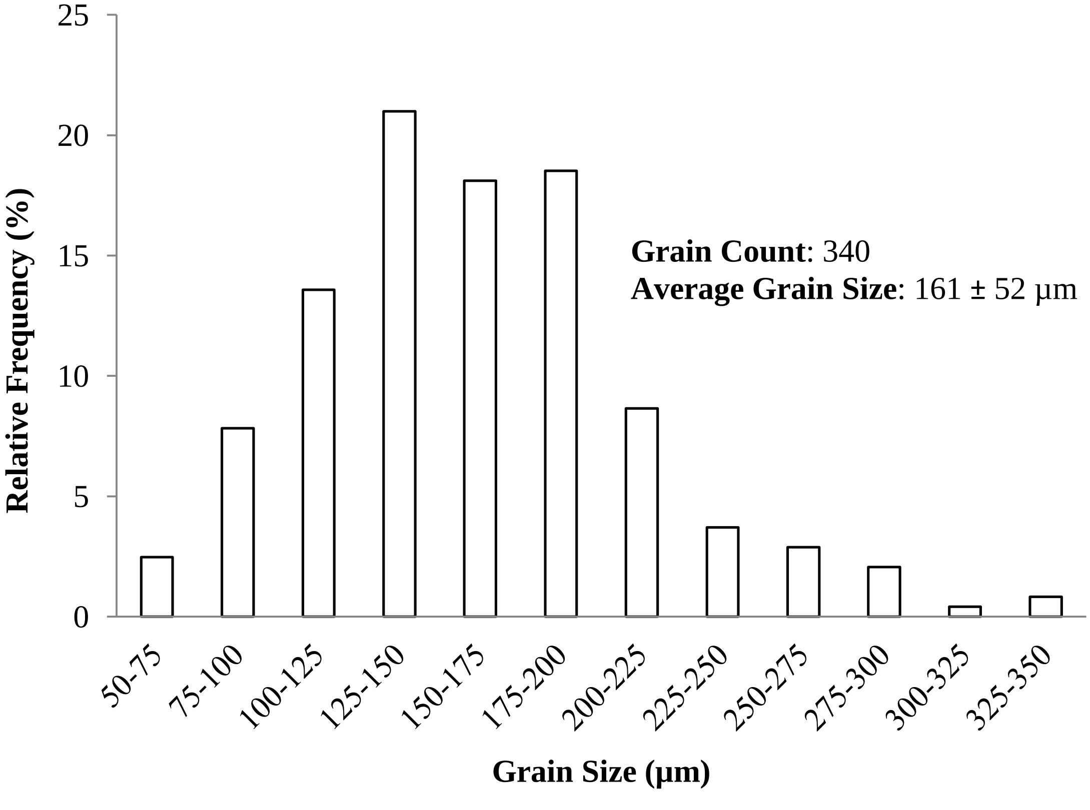

Figure 4.2: Grain size distribution histogram for polycrystalline nickel, Ni 1

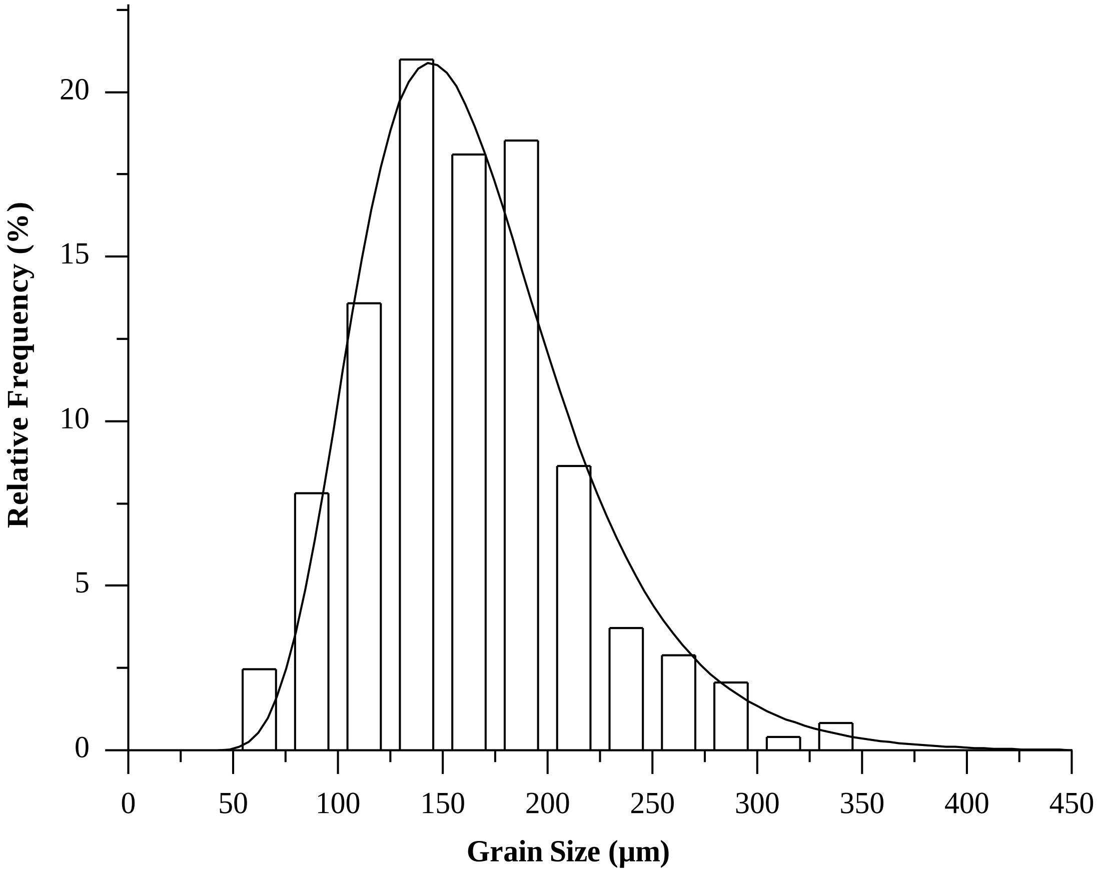

Figure 4.3: Plot of frequency against grain size for the polycrystalline nickel (Ni 1) with log-normal distribution superimposed

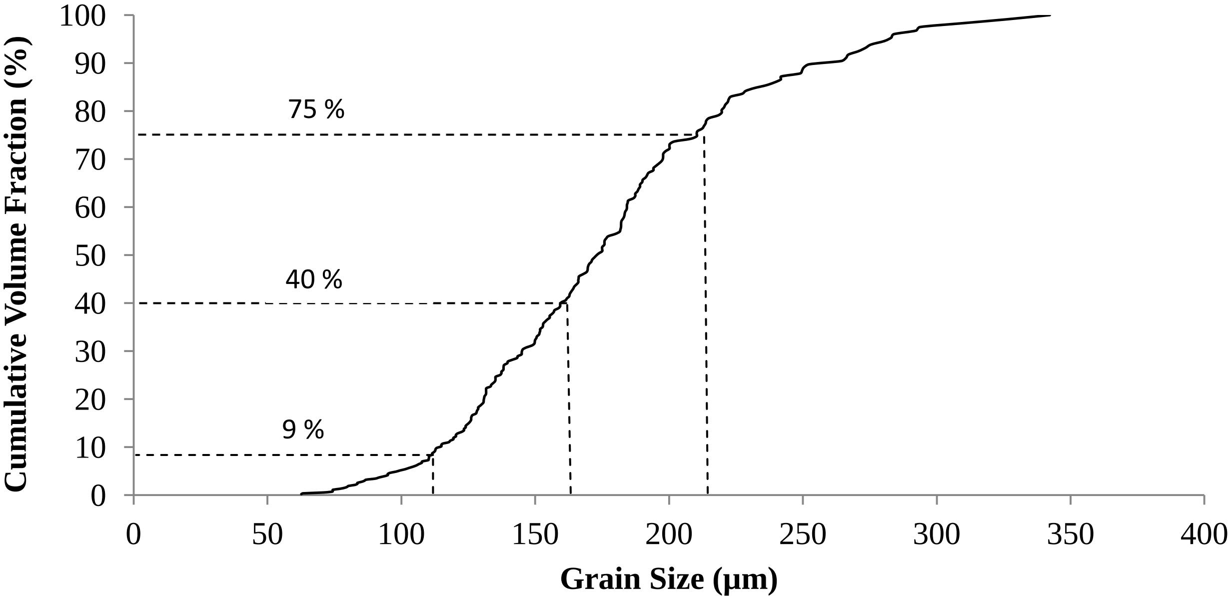

Figure 4.4: Plot of cumulative volume fraction against grain size for polycrystalline nickel, Ni 1

Figure 4.5: Bright field TEM image, dark field TEM image and SADP of ultra-fine grained nickel sample, Ni 4

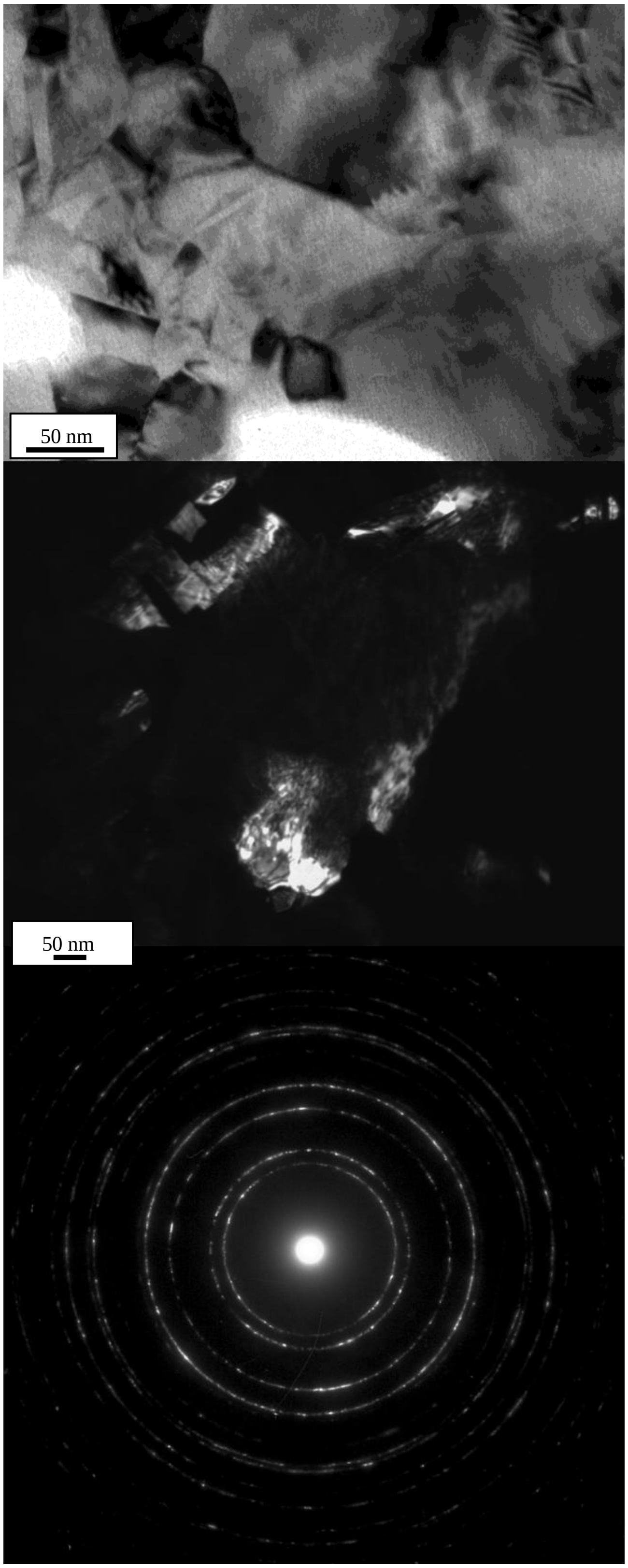

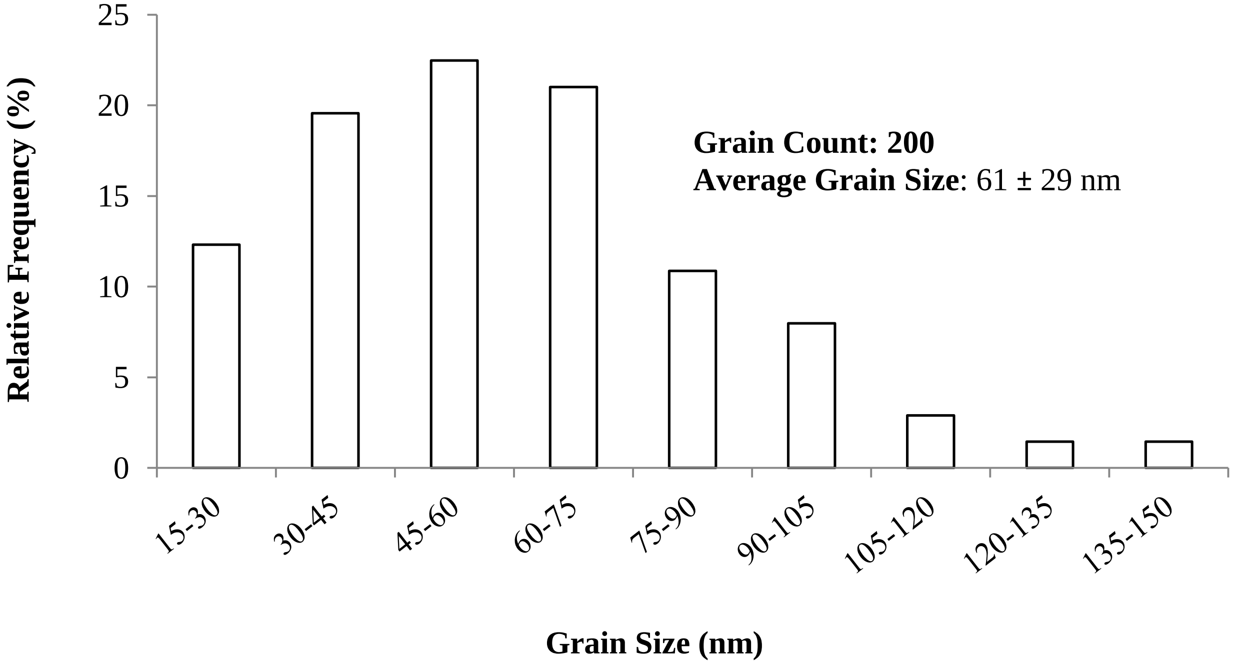

Figure 4.6: Grain size distribution histogram for ultra-fine-grained nickel, Ni 4

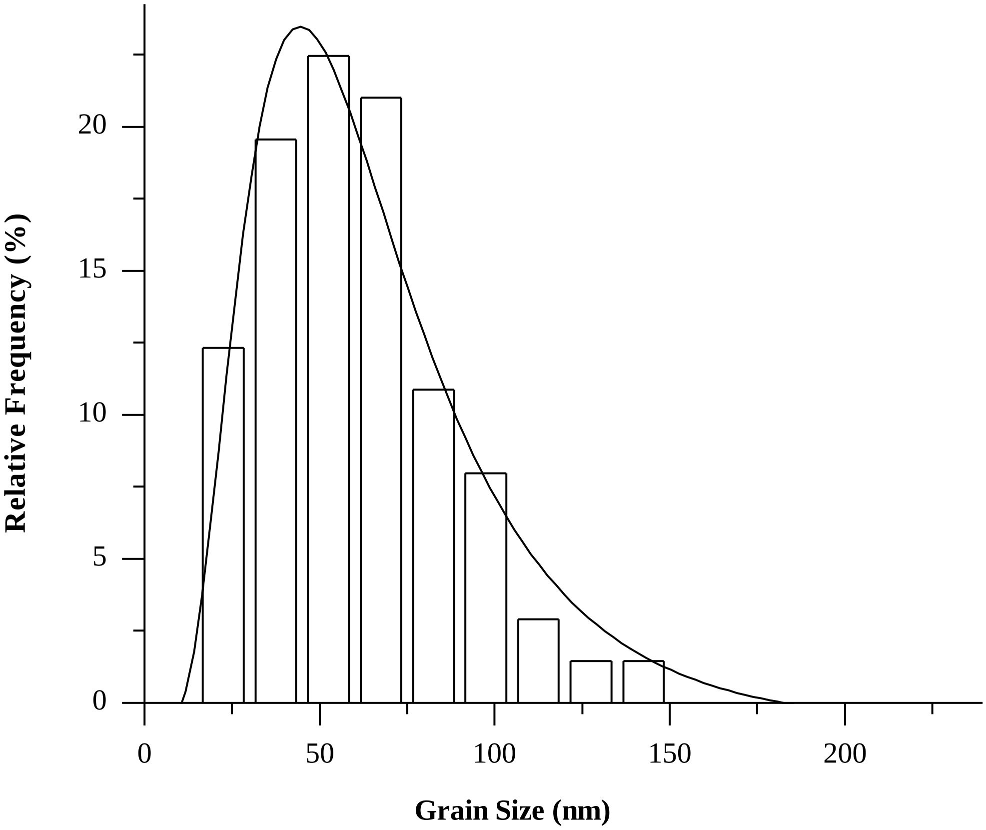

Figure 4.7: Plot of frequency against grain size for the ultra-fine-grained nickel (Ni 4) with log-normal distribution superimposed.

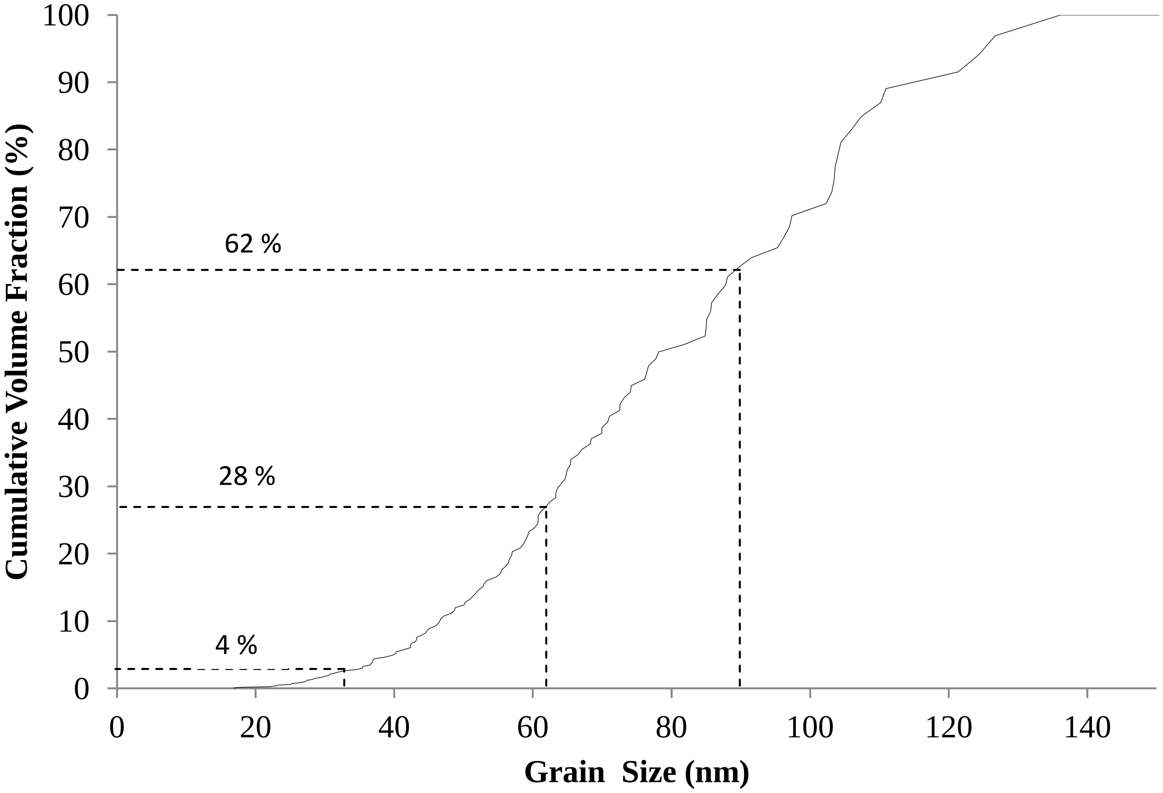

Figure 4.8: Plot of cumulative volume fraction against grain size for ultra-fine-grained nickel, Ni 4

Figure 4.9: Bright field TEM image, dark field, TEM image and SADP of nanocrystalline nickel sample, Ni 6

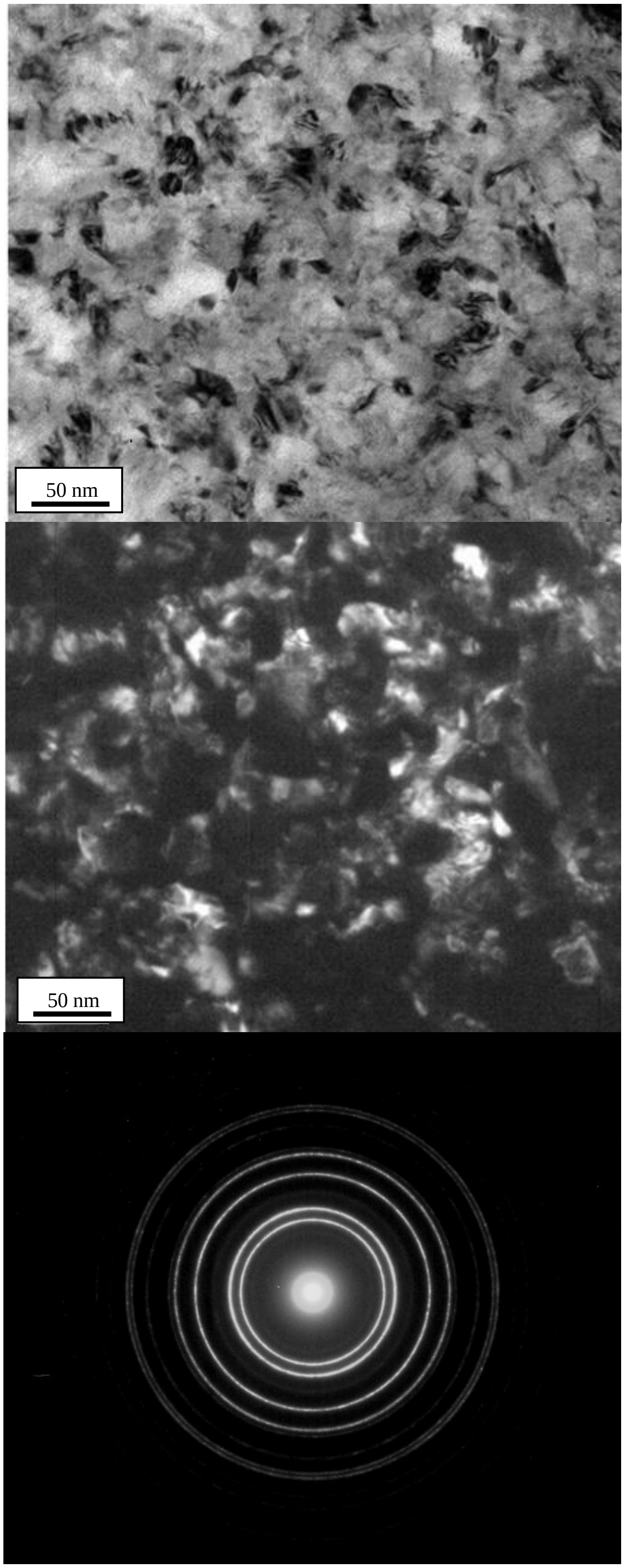

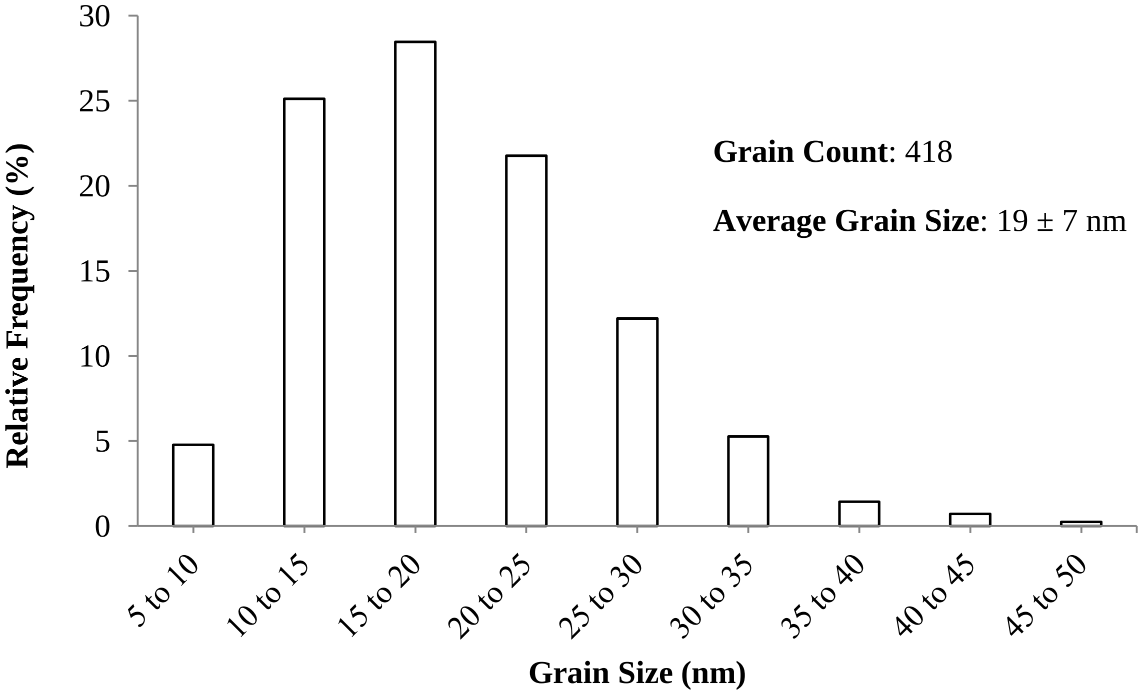

Figure 4.10: Grain size distribution histogram for nanocrystalline nickel sample, Ni 6

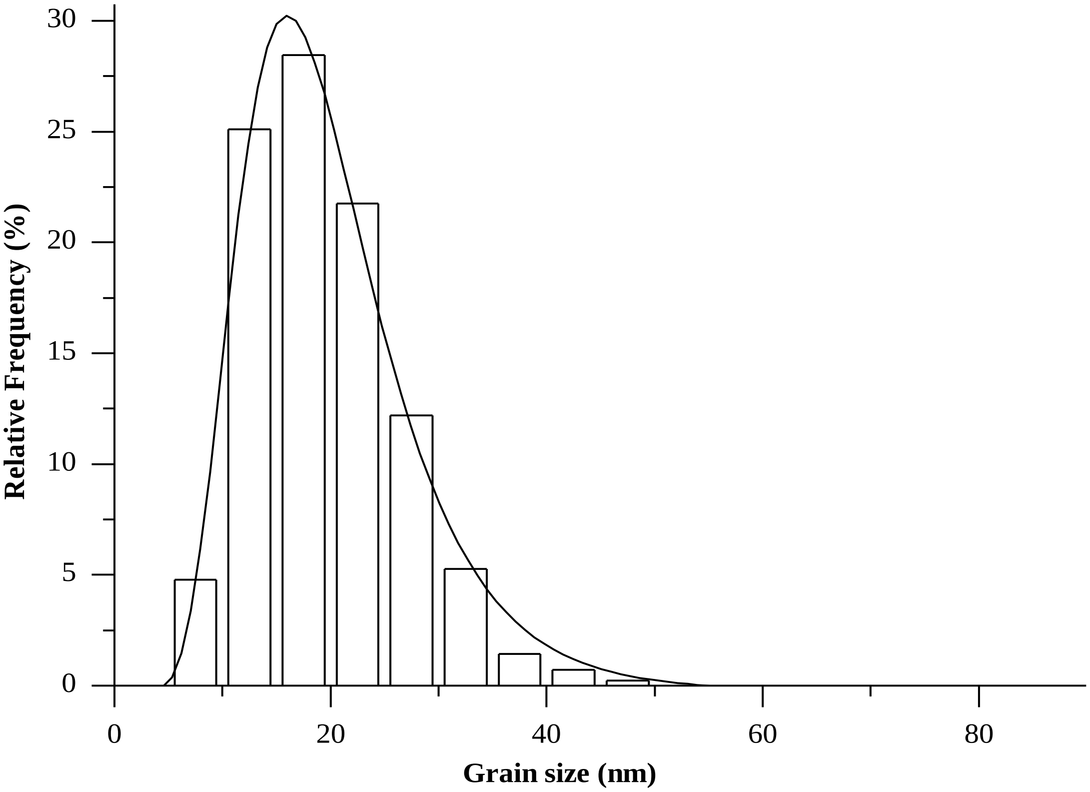

Figure 4.11: Plot of frequency against grain size for nanocrystalline nickel sample (Ni 6) with log-normal distribution superimposed

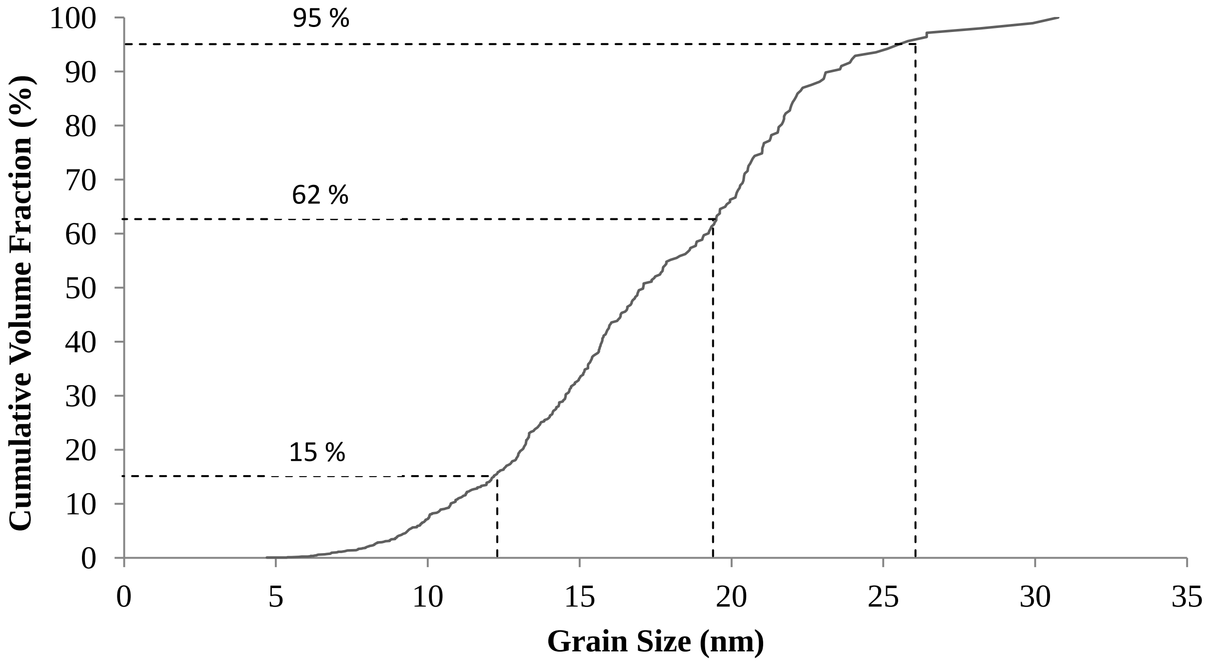

Figure 4.12: Plot of cumulative volume fraction against grain size for nanocrystalline nickel sample, Ni 6

Although the average grain sizes of the specimens were determined from the measurements on TEM micrographs, the resulting average grain size on the basis of number frequencies may not clearly represent the actual volume of the material within a certain grain size range. More specifically, the average grain sizes determined from number frequencies may underestimate the actual average grain size in terms of fractional volume in the material. This problem can be seen clearly when examining the results for sample Ni 4. The grain size distribution, Fig. 4.6, illustrated a broad distribution, in which the material has an average grain size of 61 nm with a standard deviation of ± 29 nm. Statistically the measured number frequencies are dominated by the smaller grains with sizes in the range of 32 - 90 nm. However, many TEM micrographs showed that the structure also contained much larger grains (>100 nm). By looking at the cumulative volume fraction curve (Fig. 4.8), the cumulative volume fraction between 32 to 90 nm (average grain size, 61 μm, ± 1 standard deviation of 29 nm) is only ~62 % (indicated as the dotted line in Fig. 4.8), while ~4 % of the total volume of the material is from grains below 32 nm and ~38 % from grains greater than 90 nm. In addition, this figure illustrates that a large portion of the volume (~30%) in the material is taken up by grains with diameters larger than 100 µm.

In contrast, the polycrystalline (Ni 1) and nanocrystalline (Ni 6) materials both have relatively narrow grain size distributions. By looking at the cumulative volume fraction curve for Ni 1, Fig. 4.4, ~ 66% of the volume within the material has a grain size in the range of 109 - 213 µm which is again within the upper and lower standard deviation of the average grain size. Similarly in Ni 6, the area of the grains within the upper and lower standard deviation of the average grain size (12 - 26 nm) took up ~80% of the volume within the material. Hence, the importance of the average grain size from count frequency histograms varies from sample to sample, especially when dealing with wide, non-uniform grain size distributions. Thus, cumulative volume fraction curve should be used along with the average grain size and log grain size distribution curves to determine the structure characteristics.

4.1.2 EDX Analysis

The EDX results of the composition analysis conducted on the materials are shown in, Table 4.2. The polycrystalline Ni 200 sample (Ni 1) contained about 0.3% Si which is within the specification for commercial Ni 200 alloy. Specimens 6 and 7 with the smallest grain size (19 and 8 nm, respectively) contain alloying elements of iron or phosphorus. On the other hand, the EDX analysis on all other electrodeposited materials (Ni 2, Ni 3, Ni 4, Ni 6) showed that they were pure metals. Although some of the nanocrystalline nickel samples have a different composition than the polycrystalline and ultrafine grained nickel, it has been previously shown that the strengthening for all the nanocrystalline nickel materials is mainly due to grain size refinement; alloying with phosphorus and iron had no significant effect on hardness in these materials [Erb (1995)].

Table 4.2: Composition of the materials in weight percentage, as determined by energy-dispersive X-ray spectroscopy analysis

Sample	Average Grain Size	Composition, weight %
Ni 1	161 µm	99.7 wt% Ni 0.3 wt% Si
Ni 2	540 nm	100 wt% Ni
Ni 3	318 nm	100 wt% Ni
Ni 4	100 nm	100 wt% Ni
Ni 5	29 nm	100 wt% Ni
Ni 6	19 nm	86.1 wt% Ni 13.9 wt% Fe
Ni 7	8 nm	95.5 wt% Ni 4.5 wt% P

4.2 Vickers Micro-hardness

To determine the relationship between Superficial Rockwell / Rockwell hardness and Vickers micro-hardness for nickel, hardness measurements were conducted on each specimen and the average hardness values were calculated from five or more measurements. For a direct comparison with ASTM standard conversion Tables (see Appendix), Vickers micro-hardness measurements were recorded with an applied load of 1000 grams.

Table 4.3 shows the average Vickers micro-hardness value for each specimen. It is apparent that Ni 1 with the largest grain size of 161 µm has the lowest hardness value of 93 HV. With the reduction in grain size down to 8 nm, the hardness increased to 768 HV. Fig. 4.13 plots the Vickers micro-hardness as a function of grain size. The strengthening coefficient, k, in the Hall-

Petch relationship is calculated to be 1778.4 HV/(nm$^{-0.5}$) from this graph. This value is close to the value of k=2206 HV/(nm$^{-0.5}$) previously reported by Huges et al [Huges et al. (1986)]. The slight deviation in the k value could be from factors such as material processing history or residual stresses. Overall, the Vickers micro-hardness measurements in this study are in good agreement with the classical Hall-Petch relationship, where the hardness increases with the refinement of grain size.

Table 4.3: Average Vickers Micro-hardness measurements

Sample	Average Grain Size	Average Vickers Micro-hardness (1000g, HV)
Ni 1	161 µm	93 ± 3
Ni 2	540 nm	209 ± 6
Ni 3	318 nm	244 ± 3
Ni 4	100 nm	349 ± 3
Ni 5	29 nm	462 ± 13
Ni 6	19 nm	537 ± 3
Ni 7	8 nm	768 ± 3

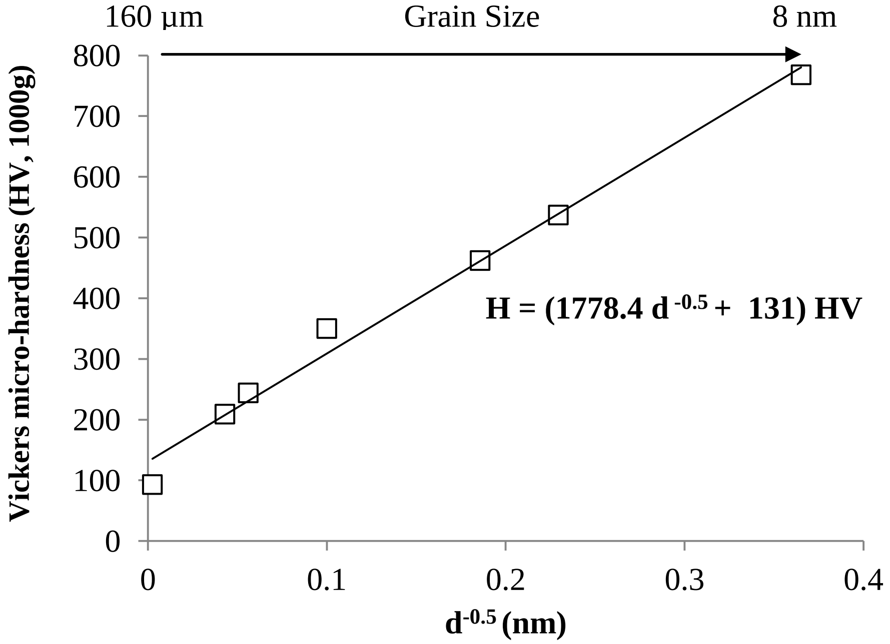

Fig. 4.13: Vickers hardness plotted against grain size

4.3 Rockwell and Superficial Rockwell Hardness

Table 4.4 shows the average hardness values for each specimen on different Rockwell hardness scales. It is apparent that Ni 1 (grain size of 161 µm) is the softest specimen with hardness value of 75, 33 and 26 at 60, 100 kgf with the ball indenter and 60 kgf with the diamond indenter respectively. On the other hand, the Rockwell hardness of nanocrystalline nickel, Ni 6 (grain size of 19 nm), has Rockwell hardness values of 123, 118, 74 and 60 at 60, 100 kgf with the ball and diamond indenter, respectively.

Table 4.4: Average Rockwell hardness measurements

Sample	**Rockwell Hardness ± STDEV**				
	Average Grain Size	**Ball Indenter**		**Diamond Indenter**	
		60 Kgf	*100 Kgf*	*60 Kgf*	*100 Kgf*
Ni 1	161 µm	75 ± 0.4	33 ± 3.6	26 ± 3.1	N/A
Ni 2	540 nm	107 ± 0.9	92 ± 1.2	56 ± 1.1	35 ± 0.5
Ni 3	318 nm	105 ± 0.1	89 ± 1	50 ± 3.1	25 ± 2.4
Ni 4	100 nm	116 ± 0.1	102 ± 0.5	67 ± 0.2	47 ± 0.3
Ni 5	29 nm	120.9 ± 0.17	114 ± 0.2	74 ± 0.13	60 ± 0.3
Ni 6	19 nm	123 ± 0.5	118 ± 1.4	74 ± 0.3	60 ± 0.2
Ni 7	8 nm	N/A	N/A	N/A	N/A

Rockwell hardness measurements for sample Ni 7 are not available due to the brittleness of this material. As the indenter penetrated into the specimen, the sample fractured into numerous pieces. Hence, Rockwell hardness measurements for specimen Ni 7 could not be measured.

Table 4.5 summarizes the Superficial Rockwell hardness measurements for all specimens at different loading conditions and indenter geometries. Again, the hardness of the specimen increases from Ni 1 to Ni 7, i.e. with decreasing grain size for all superficial scales.

Table 4.5: Average Superficial Rockwell hardness measurements

Sample	**Superficial Rockwell Hardness ± STDEV**						
	Average Grain Size	**Ball Indenter (T)**			**Diamond Indenter (N)**		
		15 Kgf	30 Kgf	45 Kgf	15 Kgf	30 Kgf	45 Kgf
Ni 1	161 μm	71 ± 0.9	39 ± 1.1	9 ± 1.8	59 ± 4.1	11 ± 0.9	N/A
Ni 2	540 nm	87 ± 0.8	74 ± 2.3	63 ± 1.9	64 ± 2.6	32 ± 1.4	17 ± 1.7
Ni 3	318 nm	89 ± 2	80 ± 3.4	61 ± 2.2	76 ± 0.7	57 ± 2.3	31 ± 0.8
Ni 4	100 nm	94 ± 0.8	86 ± 0.1	78 ± 0.3	81 ± 1.5	69 ± 0.6	59 ± 0.6
Ni 5	29 nm	96 ± 0.4	90 ± 0.1	85 ± 0.6	85 ± 0.3	75 ± 0.7	67 ± 0.6
Ni 6	19 nm	96 ± 0.9	93 ± 0.9	87 ± 1	85 ± 1.5	74 ± 1.4	68 ± 2.1
Ni 7	8 nm	99 ± 0.1	97 ± 0.2	94 ± 1	91 ± 0.6	79 ± 0.3	66 ± 1.7

Figs 4.14 a, b and c show plots of Rockwell hardness and Superficial Rockwell hardness as a function of the reciprocal of the square root of grain size. It is apparent that with the reduction in grain size, the values for all Rockwell/Superficial Rockwell scales increase.

However, the curves for Rockwell hardness and Superficial Rockwell hardness do not show a linear relationship with $d^{-0.5}$, as was the case for Vickers hardness (Fig. 4.13). The reason for this is that the relationship between the Vickers hardness and Rockwell/Superficial Rockwell hardness is not a linear function. This will be discussed in more detail in section 4.4.

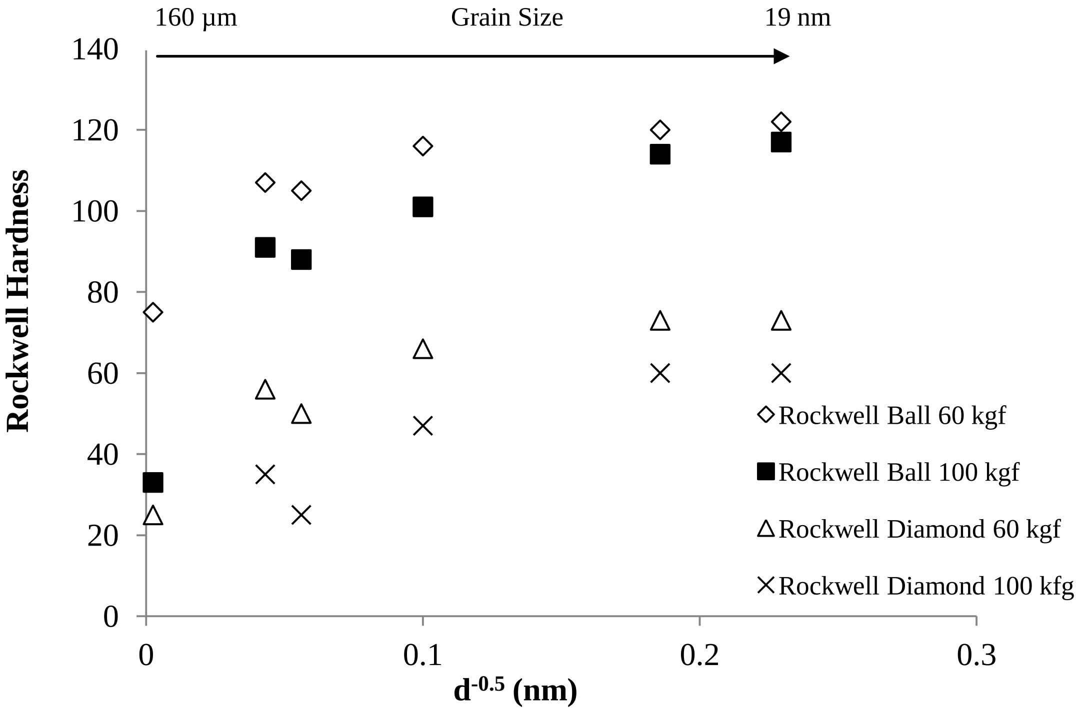
160 µm
Grain Size
19 nm
140
120
100
80
60
40
20
0
Rockwell Hardness
◇Rockwell Ball 60 kgf
■Rockwell Ball 100 kgf
△Rockwell Diamond 60 kgf
×Rockwell Diamond 100 kfg
0
0.1
0.2
0.3
d$^{-0.5}$ (nm)

a)

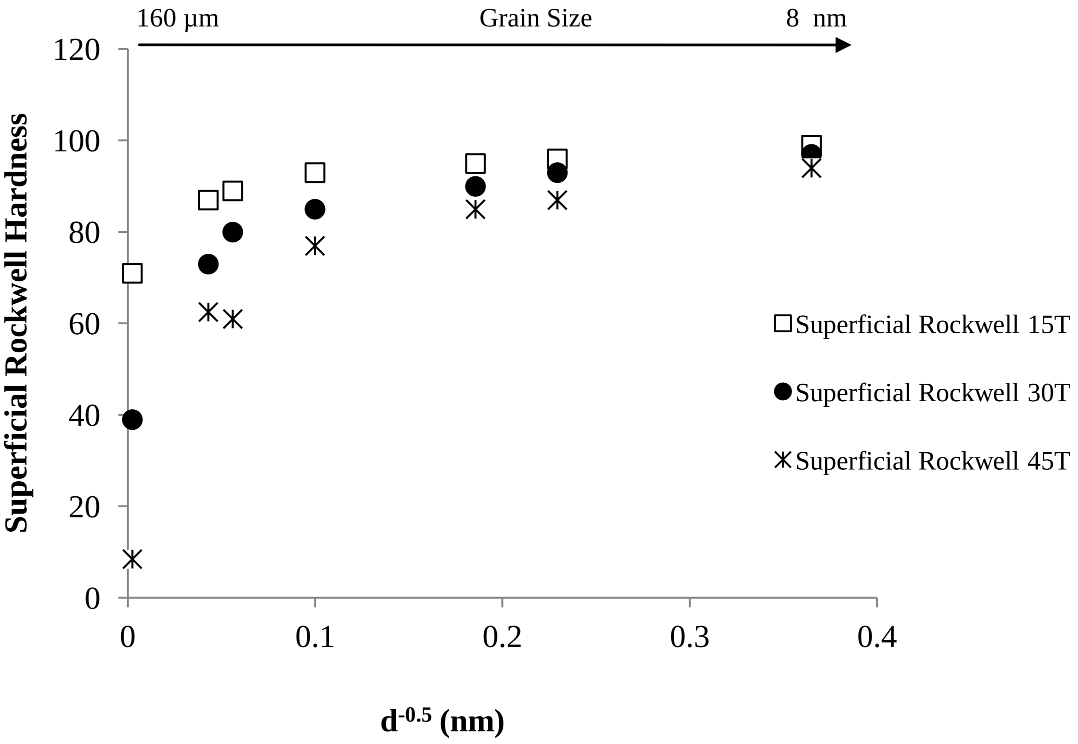
160 µm
Grain Size
8 nm
120
100
80
60
40
20
0
Superficial Rockwell Hardness
□Superficial Rockwell 15T
●Superficial Rockwell 30T
✳Superficial Rockwell 45T
0
0.1
0.2
0.3
0.4
d$^{-0.5}$ (nm)

b)

c)

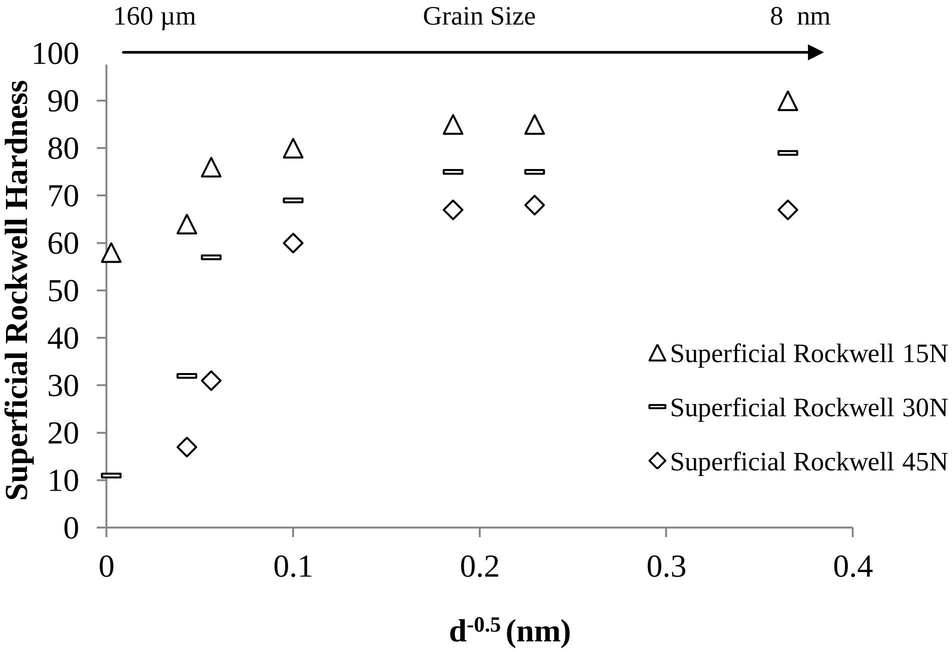

Fig. 4.14: Hardness plotted against d$^{-0.5}$ a) Rockwell, b) Superficial Rockwell Ball indenter and c) Superficial Rockwell Diamond indenter

4.4 Relationship between Vickers and Rockwell Scales

ASTM standard E140-07 contains standard hardness conversion tables, for which hardness conversions among different hardness scales for metals are given. The relevant tables for nickel are reproduced in the appendix. The hardness conversion relationships found in the standard for nickel and high-nickel (nickel concentrations greater than 50 %) is intended specifically for nickel-aluminum-silicon specimens (ASTM E140-07). To cover a relatively large range in hardness, these nickel and high-nickel alloys were in the form of annealed to heavily cold-worked or aged-hardened conditions, including intermediate states.

Conversion factors were generated by ASTM from the specific hardness numbers contained in the hardness conversion table (refer to appendix). In the ASTM hardness relationships, Vickers hardness as a function of Rockwell/Superficial Rockwell hardness is expressed as:

$$(Y)^{-1} = \text{Constant} + A(X) + B(X^2) \tag{18}$$

where Y are the Vickers hardness and X are the Rockwell or Superficial Rockwell hardness values. The values for the constant, A and B are given in Tables 4.6 and 4.7, respectively.

Table 4.6: Vickers to Superficial Rockwell Hardness Relationships

<u>Superficial Rockwell Hardness Diamond Indenter</u>			
Load: 15 kgf			
	B	A	Constant
ASTM Standard	1.75×10^{-6}	-0.0043	0.03
Load: 30 kgf			
	B	A	Constant
ASTM Standard	6.17×10^{-7}	-0.0002	0.01
Load: 45 kgf			
	B	A	Constant
ASTM Standard	3.6×10^{-7}	-0.0001	0.006
<u>Superficial Rockwell Hardness Ball Indenter</u>			
Load: 15 kgf			
	B	A	Constant
ASTM Standard	-8.9×10^{-8}	-0.0004	0.037
Load: 30 kgf			
	B	A	Constant
ASTM Standard	-4.02×10^{-8}	-0.0002	0.019
Load: 45 kgf			
	B	A	Constant
ASTM Standard	-1.62×10^{-7}	-0.0001	0.013

Table 4.7: Vickers to Rockwell Hardness Relationships

	B	A	Constant
<u>Rockwell Hardness Diamond Indenter</u>			
Load: 60 kgf			
ASTM Standard	$1.67X10^{-6}$	-0.0004	0.021
Load: 100 kgf			
ASTM Standard	$8.12X10^{-7}$	-0.0002	0.01
<u>Rockwell Hardness Ball Indenter</u>			
Load: 60 kgf			
ASTM Standard	-	-0.0002	0.021
Load:100 kgf			
ASTM Standard	-	-0.0001	0.017

The Superficial Rockwell and Rockwell hardness values obtained in this study are plotted against Vickers micro-hardness in Fig. 4.15 a-d. Also shown in these graphs are the relationships (lines) as per ASTM standard using equation 18 and the constants given in Tables 4.6 and 4.7. In Fig. 4.15a, the plot of the relationship between Vickers micro-hardness and Superficial Rockwell hardness using the 15 kgf ball indenter is almost identical to the plot in the ASTM standard. However, with increasing load to 30 and 45 there are considerable deviations from the ASTM relationships. Similarly, in Fig. 4.15b, the relationship between Superficial Rockwell diamond indentation hardness and the Vickers micro-hardness at 15 kgf is nearly equivalent to the relationship obtained by ASTM. However, at higher loads (30 and 45 kgf) considerable deviations are again observed.

As for Superficial Rockwell hardness, the relationships developed for Rockwell ball and diamond indenter and Vickers micro-hardness display a similar pattern (Fig 4.15c and d). There is a trend that the deviation of the results obtained in this study from the ASTM lines increases with increasing penetration load. Thus, when applying the relationships given in ASTM for nickel and high nickel alloy to nanocrystalline nickel, the estimated hardness values are relatively accurate only for low Rockwell/Superficial Rockwell loads. At higher loads the ASTM conversion would underestimate the Superficial Rockwell and Rockwell hardness of nanocrystalline nickel.

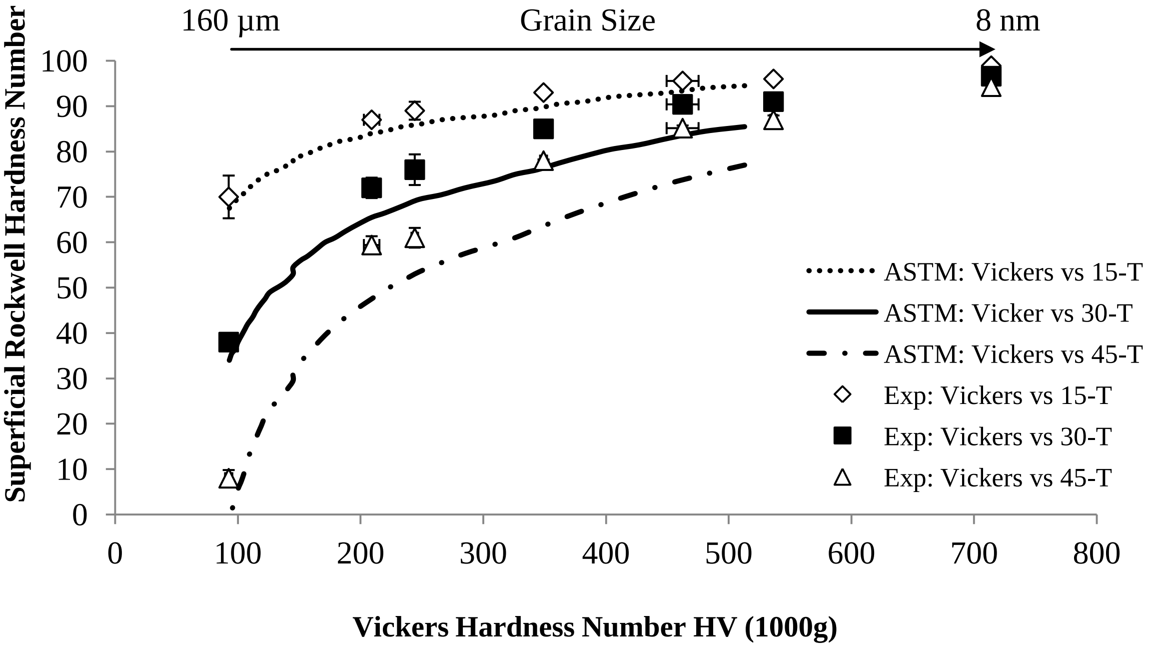

a)

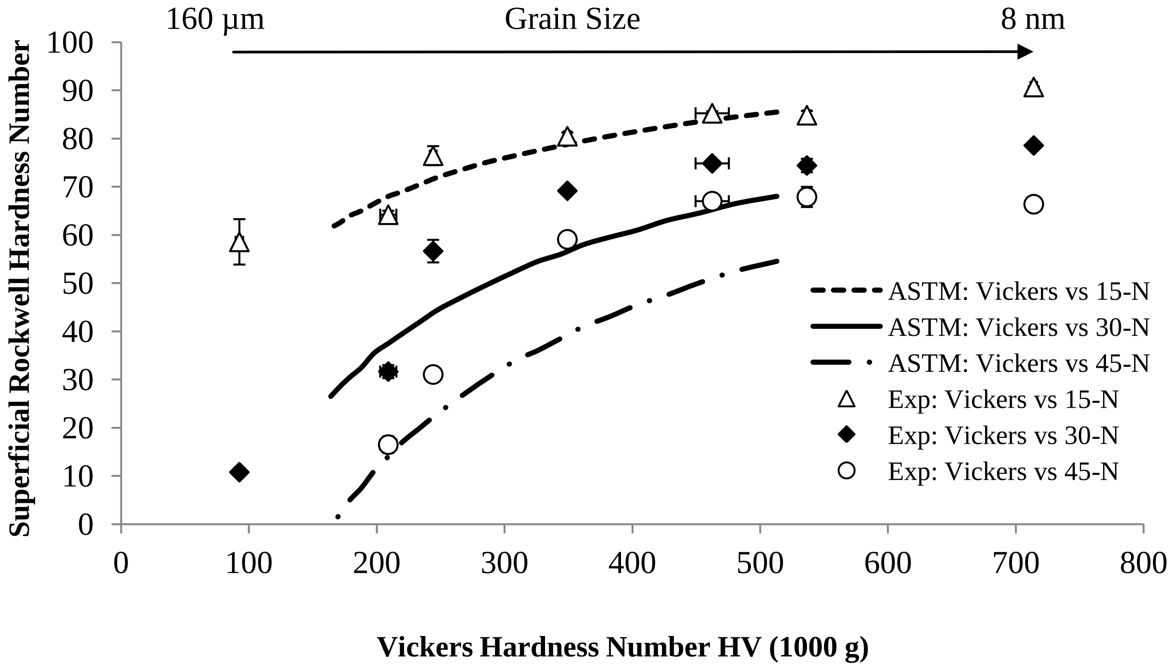
160 µm
Grain Size
8 nm
Superficial Rockwell Hardness Number
100
90
80
70
60
50
40
30
20
10
0
0
100
200
300
400
500
600
700
800
Vickers Hardness Number HV (1000 g)
ASTM: Vickers vs 15-N
ASTM: Vickers vs 30-N
ASTM: Vickers vs 45-N
Exp: Vickers vs 15-N
Exp: Vickers vs 30-N
Exp: Vickers vs 45-N

b)

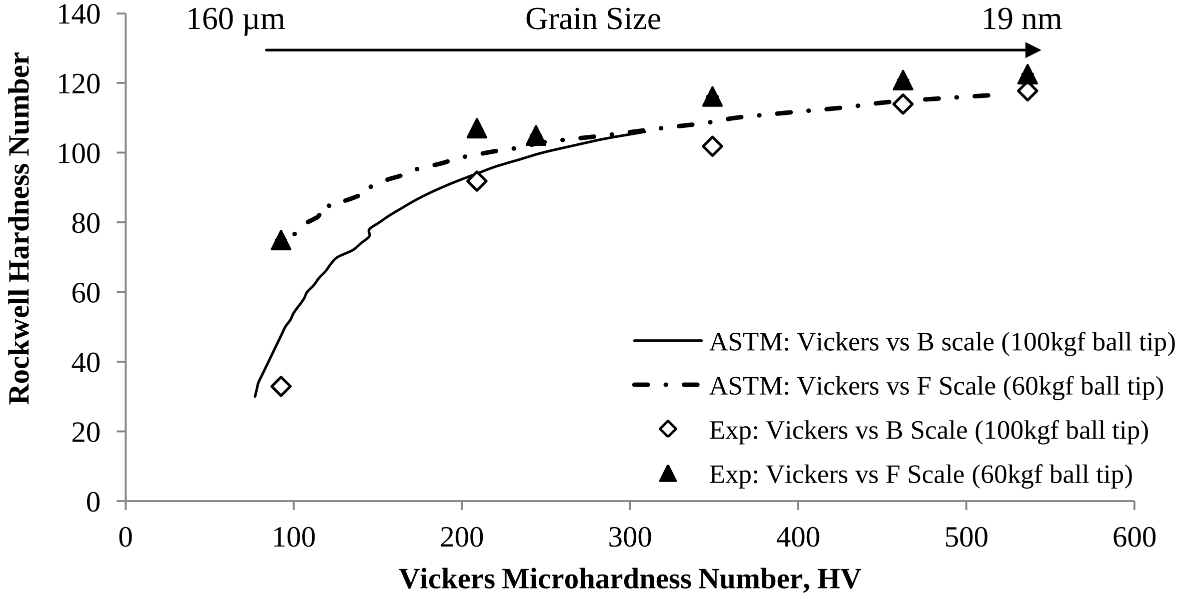
160 µm
Grain Size
19 nm
Rockwell Hardness Number
140
120
100
80
60
40
20
0
0
100
200
300
400
500
600
Vickers Microhardness Number, HV
ASTM: Vickers vs B scale (100kgf ball tip)
ASTM: Vickers vs F Scale (60kgf ball tip)
Exp: Vickers vs B Scale (100kgf ball tip)
Exp: Vickers vs F Scale (60kgf ball tip)

c)

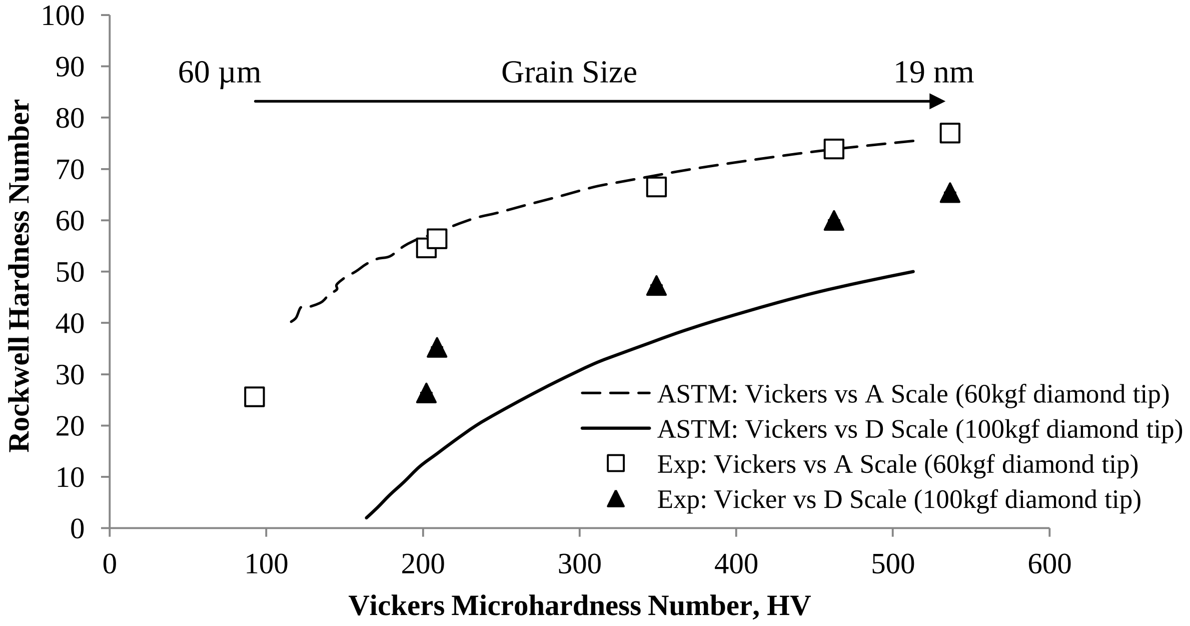

d)

Figure 4.15: Experimental results and ASTM relationship of Vickers Micro-hardness plotted against a) Superficial Rockwell, Ball indenter, b) Superficial Rockwell, Diamond indenter, c) Rockwell, Ball indenter and d) Rockwell, Diamond indenter

In an extensive analysis of hardness testing, Tabor stated that the Young's modulus of a material could significantly affect hardness measurements which are based on depth of penetration [D.Tabor (1951)]. Materials with dissimilar Young's modules have different recoveries in indentation depth after the applied load is removed from the indenter; thus, materials with higher Young's modulus would tend to have a higher Rockwell hardness value. Unfortunately, the compositions of the high nickel alloys used in ASTM's study are not given. Therefore a direct comparison cannot be made. However, one possible reason for the deviations observed in Fig. 4.15 could be the differences in the Young's modulus for the materials used in ASTM and the present study. ASTM used nickel and Ni-Al-Si alloys where the nickel content is over 50 % to achieve the broad range of Vickers hardness and these materials were in their annealed, cold worked and age hardened stage. It can be assumed that ASTM used age hardening to strengthen the nickel alloys in the higher Vickers hardness regime and that the precipitates would likely be Ni_3Al which has a lower Young's modules of 179 GPa as compared to 204 GPa for pure nickel [Metals Handbooks, (1998)]. On the other hand, a previous study by Zhou et al. [2003] on the effect of grain size on the Young's modulus in Ni has shown that Young's modulus is only weakly depended on grain size [Zhou, 2006]. The Young's modulus showed virtually no grain size dependence down to 20 nm grain size and only a slight reduction below 20 nm. Thus, according to the rule of mixture, the overall Young's modulus values for the alloys used in ASTM's study could be lower than the Young's modulus of the nanocrystalline nickel specimens used in this study.

4.5 Strain Hardening Capacity

Vickers micro-hardness measurements were utilized under the Rockwell hardness indentations on several specimens to determine the change in Vickers hardness caused by the strain introduced by the plastic deformation introduced by the much larger Rockwell indentation (see Fig. 3.1). To show a direct comparison of the work hardening behaviour of poly and nanocrystalline nickel, four specimens were selected from the extreme ends of the hardness scale to perform these tests; the large grain conventional polycrystalline nickel (Ni 1), an ultra-fine grained nickel (Ni 4), and two nanocrystalline nickel (Ni 5 and Ni 6). To measure the hardness profile on a fine scale, Vickers micro-hardness values were measured with a load of 100 grams force instead of 1000 grams. Fig. 4.16 a - f show examples of the Vickers micro-hardness indentations made beneath the Rockwell indentation. As per ASTM standard E382, the Vickers micro-hardness indentations along the lines of plastic zone were spaced apart a minimum distance of 100 µm to prevent interactions between neighbouring indentations. From these optical micrographs (Fig. 4.16), it can be observed that for the conventional polycrystalline specimen, Ni 1, the Vickers micro-hardness indentation size increases as the distance away from the Rockwell indentation increases. In contrast, for the ultra-fine grained and nanocrystalline nickel, the indentation size is relatively constant throughout the Vickers micro-hardness profile (Fig. 4.16 c to f). This indicates a significant change in hardness in the vicinity of the large Rockwell indentation for polycrystalline nickel, but a relatively constant hardness for the ultra fine grained and nanocrystalline nickel specimens.

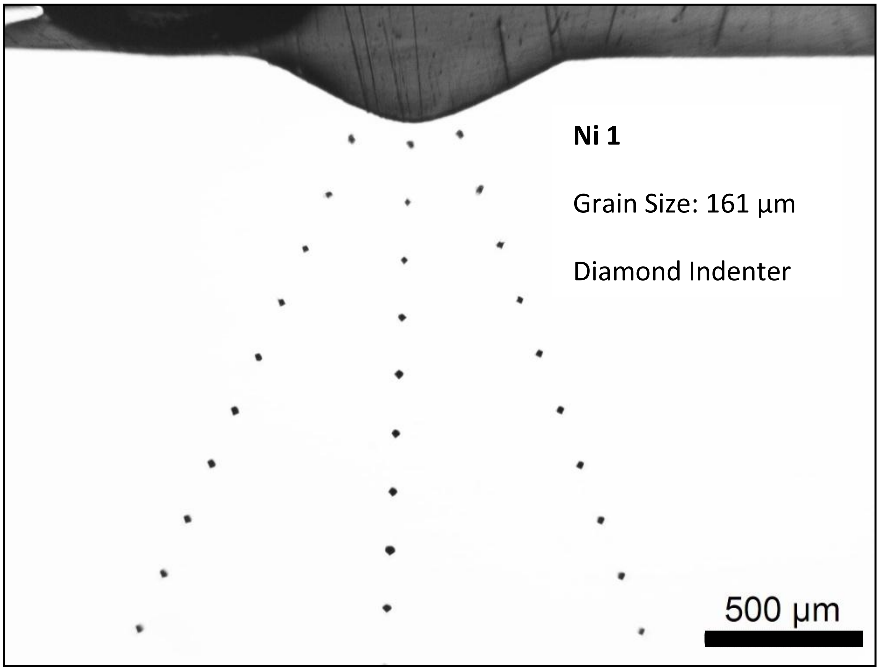

a)

b)

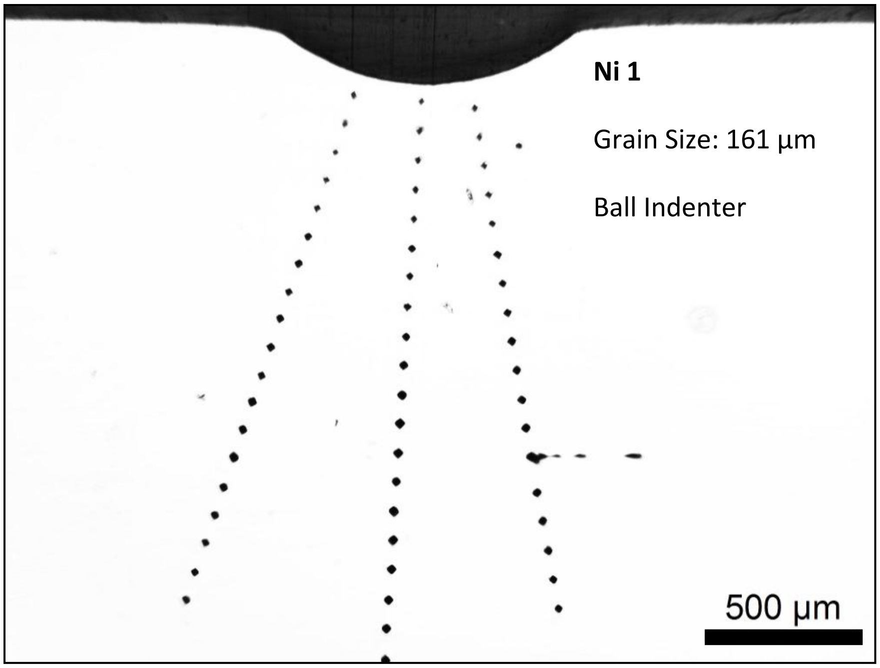
Ni 1
Grain Size: 161 µm
Ball Indenter
500 µm

c)

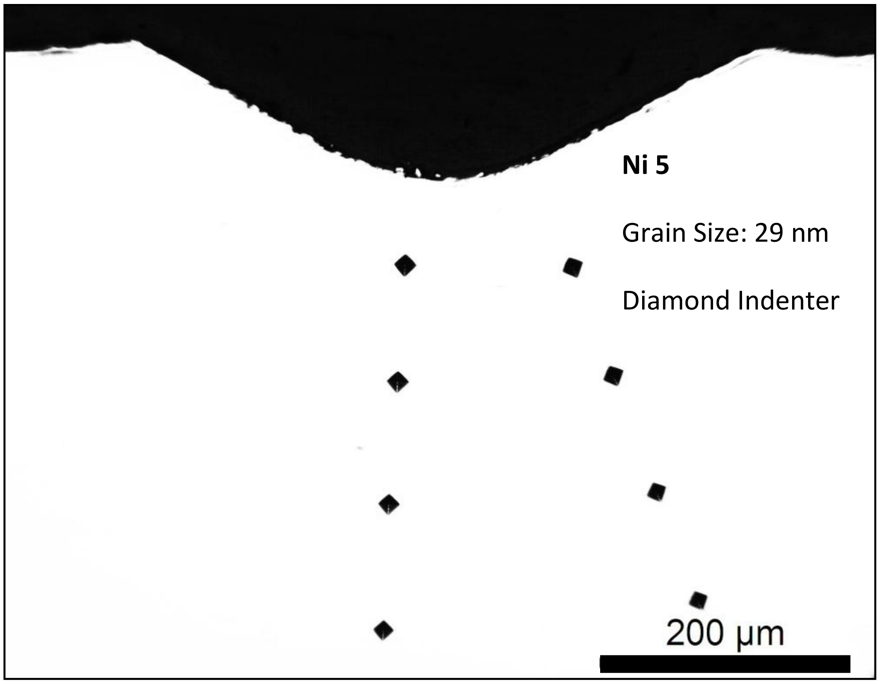
Ni 5
Grain Size: 29 nm
Diamond Indenter
200 µm

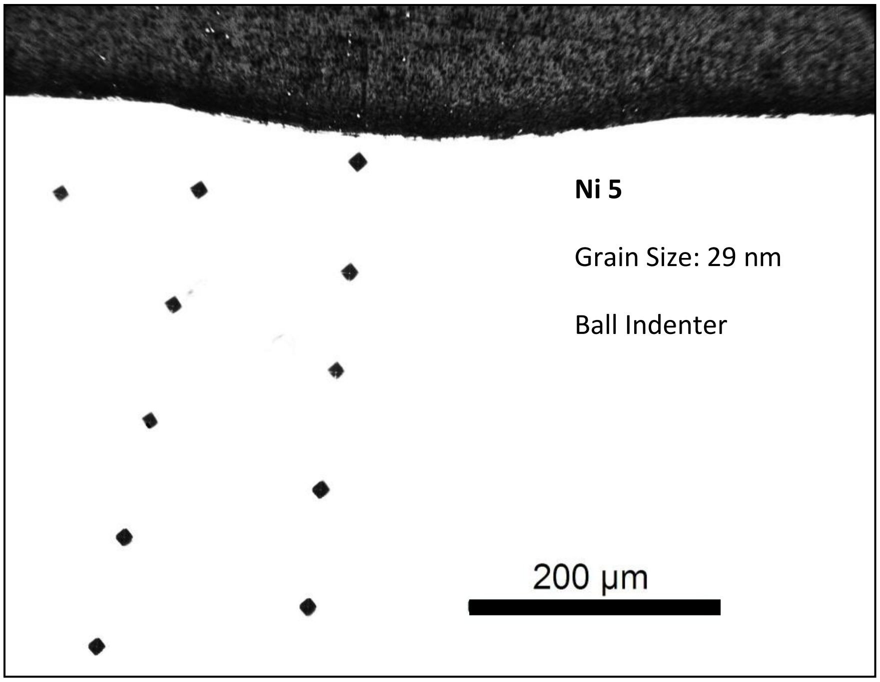
Ni 5
Grain Size: 29 nm
Ball Indenter
200 µm

d)

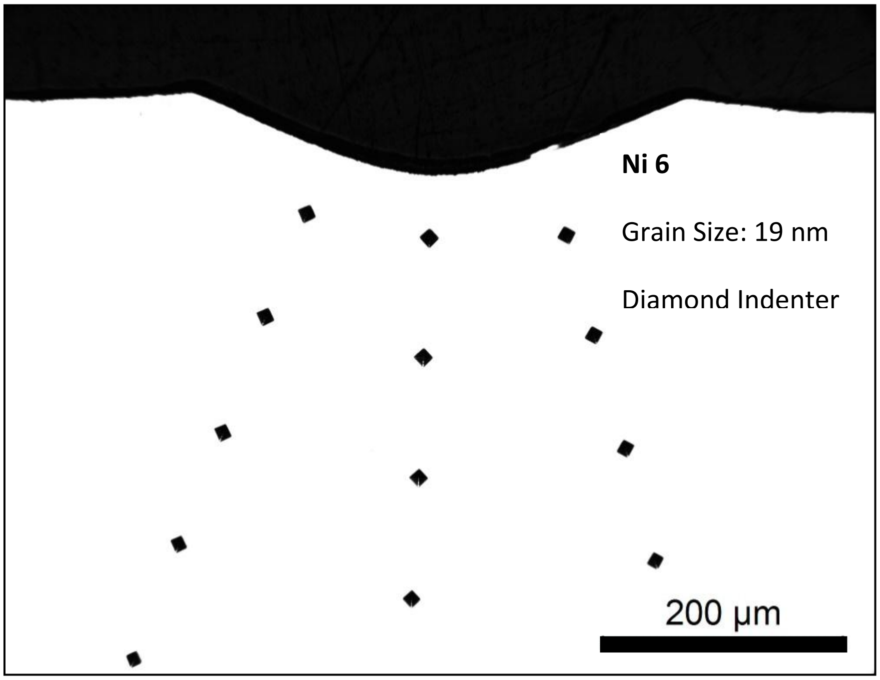
Ni 6
Grain Size: 19 nm
Diamond Indenter
200 µm

e)

f) 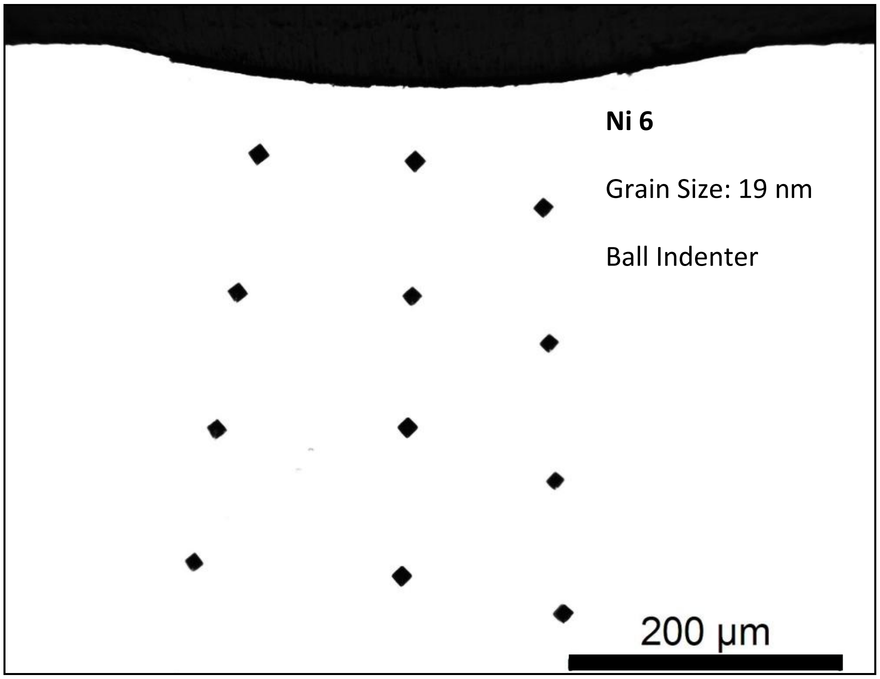

Figure 4.16: Optical micrographs of the cross sections of Rockwell indentations in a) Ni 1, Diamond indenter, b) Ni 1, Ball indenter, c) Ni 5, Diamond indenter, d) Ni 5, Ball indenter, e) Ni 6, Diamond indenter and f) Ni 6, Ball indenter

The Vickers hardness contours below the Rockwell diamond and ball indents of the four nickel specimens are shown in Fig. 4.17 and 4.18, respectively. These figures summarize the measured Vickers micro-hardness as a function of distance away from the Rockwell indentation for the polycrystalline to nanocrystalline materials. For the polycrystalline nickel, Ni 1, a notable change in hardness is observed under the Rockwell ball and diamond indentations. The Vickers hardness closest to the Rockwell indentation has a maximum value of ~258 kg/mm^2 at a distance of ~65 µm and 245 kg/mm^2 also at a distance of ~65 µm from the Rockwell diamond and ball indentations, respectively. As compared to the average hardness of the bulk material, with a hardness of 130 kg/mm^2, the hardness closest to the Rockwell indentation is almost 100% higher.

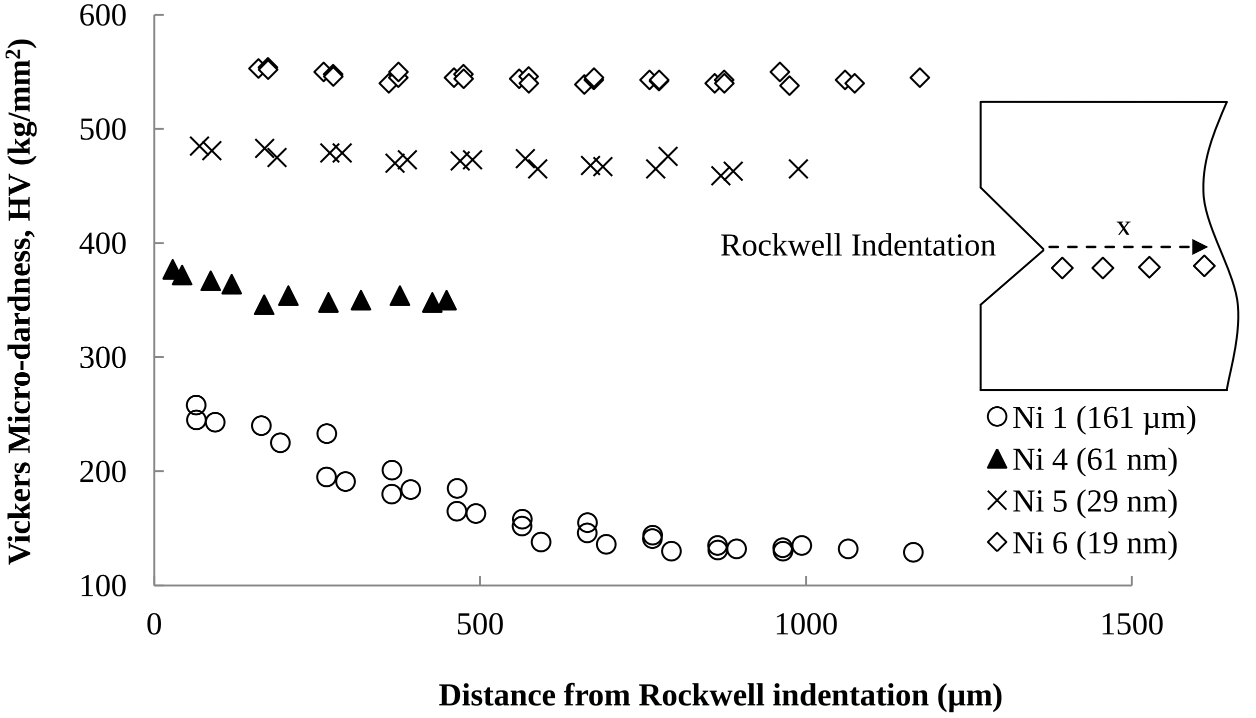

Figure 4.17: Vickers micro-hardness as a function of distance from the Rockwell Diamond indentation

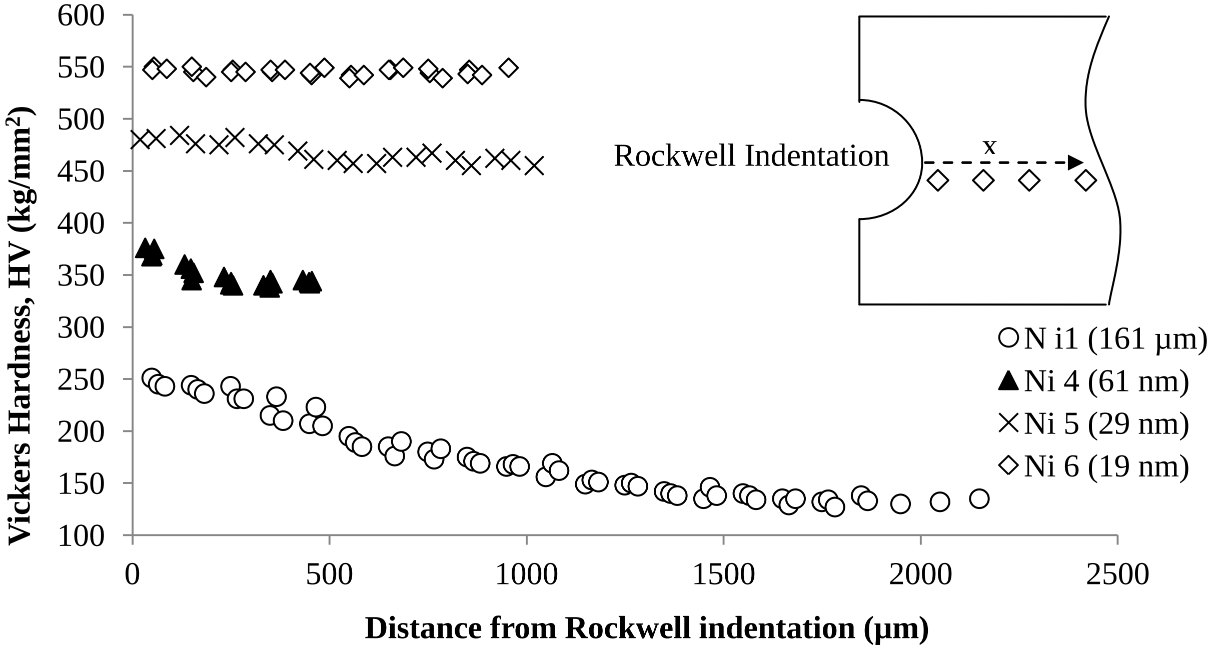

Figure 4.18: Vickers micro-hardness as a function of distance from the Ball indentation

In contrast, the change in Vickers micro-hardness within the plastic zone for the ultra fine grained nickel, Ni 4, is significantly smaller. The Vickers micro-hardness measurement closest to the Rockwell indent has a value of 377 kg/mm^2 which progressively drops to a hardness of 350 kg/mm^2 at a distance of ~160 μm under both ball and diamond Rockwell indentation. With further reduction in grain size to the nanocrystalline region, Ni 5 and Ni 6, the measured Vickers micro-hardness beneath the Rockwell indent is relatively constant through the entire cross section below the indentation. It should be noted that, due to the differences in specimen thickness, the Vickers micro-hardness measurements for the ultra-fine grained nickel (Ni 4) had to be terminated at approximately 500 μm, while measurements beyond 1000 μm were possible for specimens Ni 1, Ni 5 and Ni 6, respectively.

To illustrate the differences in strain hardening capacity for the materials more clearly, normalized hardness is plotted against distance away from the Rockwell ball and diamond indentations, Figs. 4.19 and 4.20. Normalized hardness is defined as the Vickers micro-hardness at a certain distance from the Rockwell indentation divided by the average Vickers micro-hardness of the bulk material, given in Table 4.8. Note that these hardness values are not the same as in Table 4.3. This is because the load used here was only 100 grams while the values given in Table 4.3 were for 1000g loads.

Again, the normalized hardness contours below the Rockwell hardness indentation of the conventional nickel, Ni 1, show considerable changes in the hardness. Vickers micro-hardness values closest to the Rockwell indent are about twice the hardness value of the bulk material. The hardness in the profile gradually decreases with increasing distance from the Rockwell indentation and from the contours it can be seen that the hardness begins to plateau at ~600 µm under the Rockwell diamond indentation and ~1300 µm under the Rockwell ball indentation. On the other hand, with reduction in grain size to the ultra fine grain regime, Ni 4, the hardness value closest to the Rockwell indent is only about 9% higher than the bulk hardness and the measured hardness plateaus at ~150 µm away from the Rockwell indent for both diamond and ball indenters. With further reduction into the nanocrystalline regime, Ni 5 and Ni 6, the changes in hardness are insignificant.

Table 4.8: Average Vickers Micro-hardness measured at 100 grams

Sample	Grain Size	Vickers Micro-hardness (100g, HV)
Ni 1	161 µm	125 ± 5.2
Ni 4	61 nm	345 ± 3.5
Ni 5	29 nm	462 ± 13
Ni 6	19 nm	563 ± 4

To study this phenomenon on a finer scale, nano-indention hardness was utilized on the finest grain sized specimen, Ni 6 (Fig. 4.21). In Fig. 4.22, normalized hardness is again plotted against distance from the Rockwell indentation for the first 200 µm, where the nano-indentation hardness value at a specific distance is divided by the average nano-indentation hardness of the bulk material.

a)

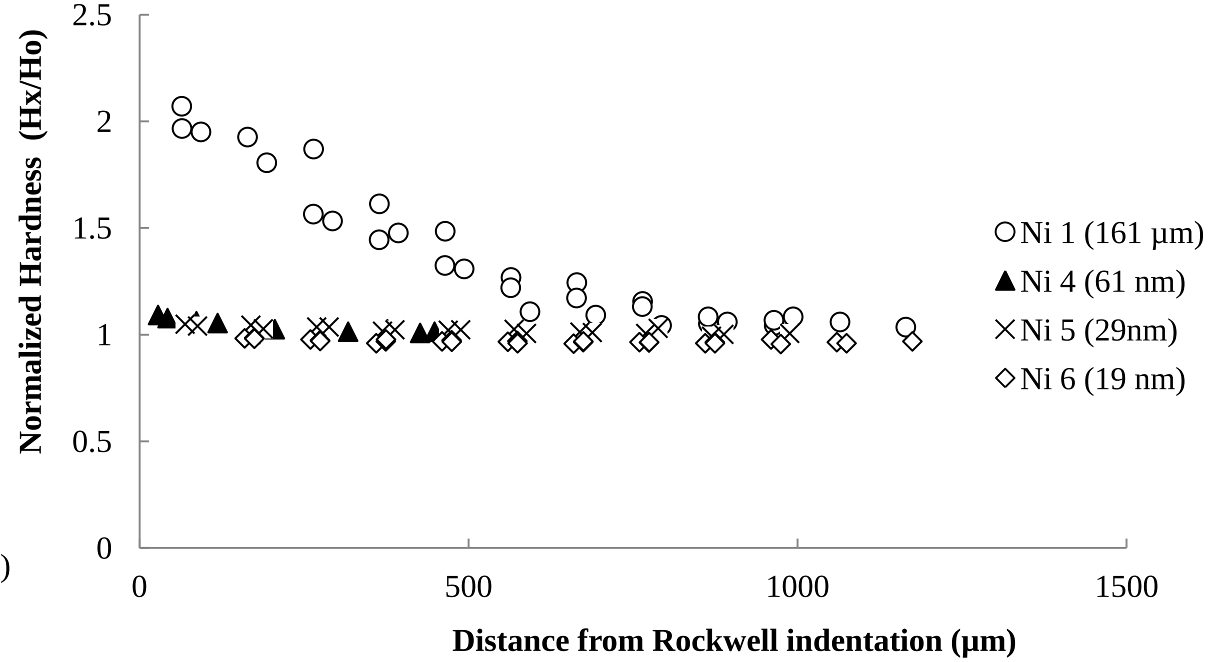

Figure 4.19: Normalized hardness as a function of distance from Rockwell indentation, under Rockwell Diamond indentations

b)

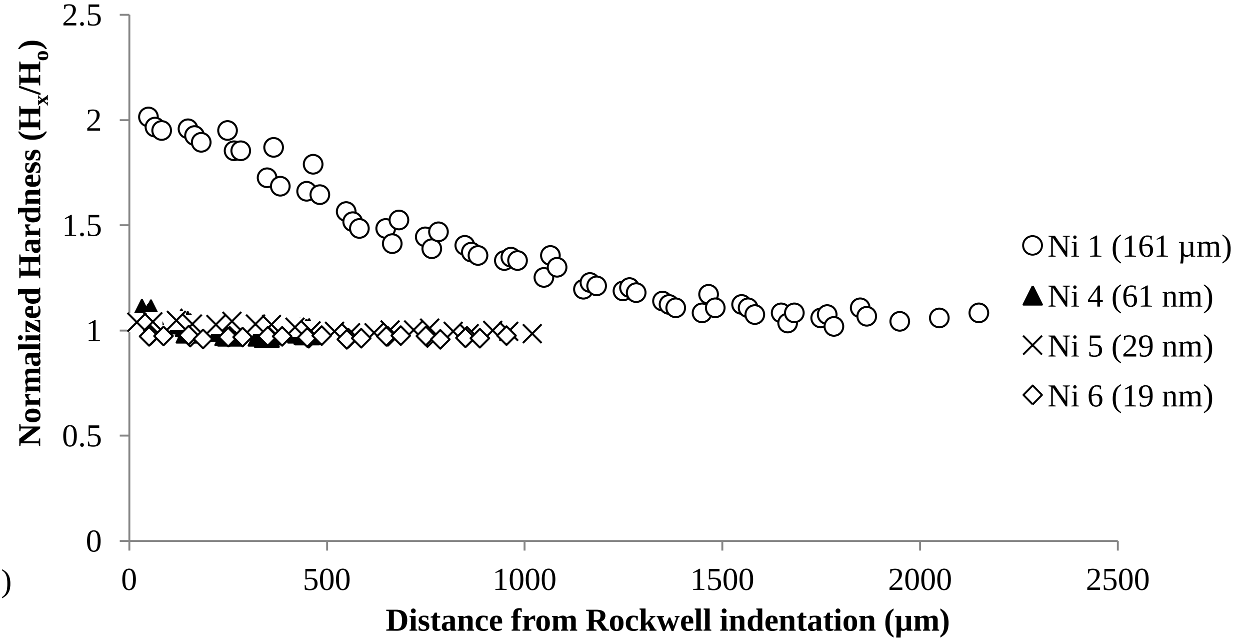

Figure 4.20: Normalized hardness as a function of distance from Rockwell indentation, under Rockwell Ball indentations

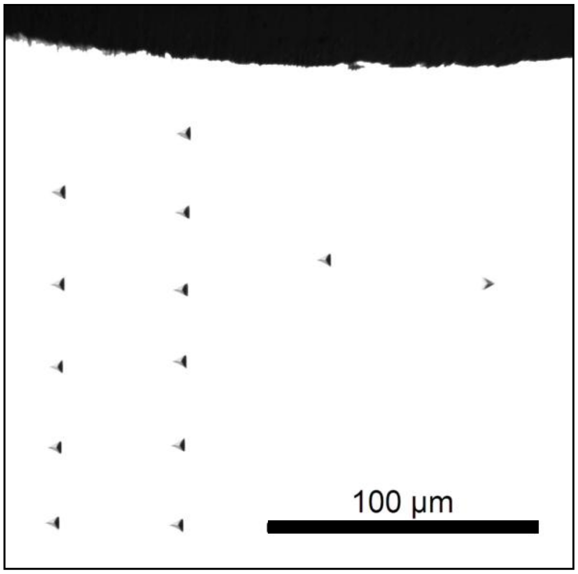

Figure 4.21: Optical micrographs of the cross sections of Rockwell Diamond indentation in Ni 6

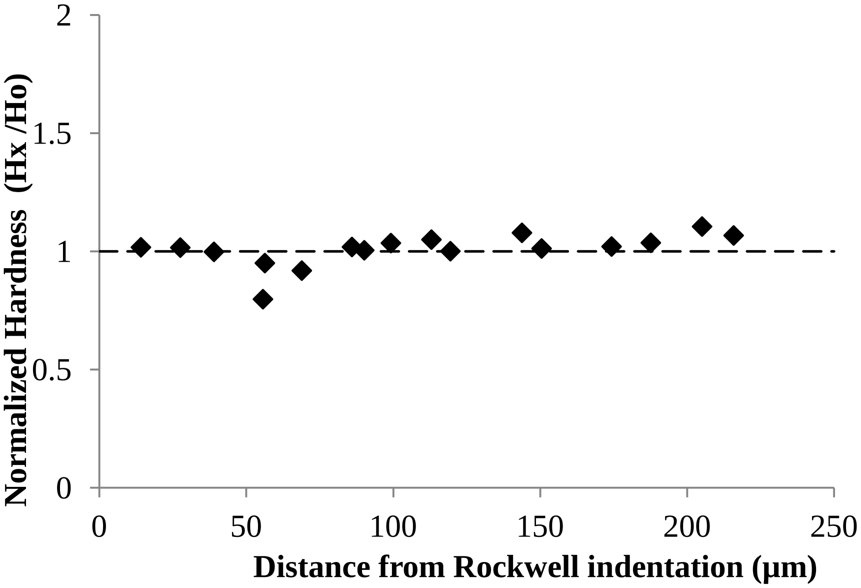

Figure 4.22: Normalized nanoindentation hardness as a function of distance from Rockwell indentation against under Rockwell Diamond indentation

Fig. 4.22 summarizes the three series of nano-indentation hardness measurements made beneath the Rockwell indentation; the hardness values over the distance of 200 μm under the indent are fairly constant. Thus, these results support the normalized Vickers micro-hardness measurements. The closest nano-indentation measurement made was 14 μm away from the Rockwell indentation, with a hardness value approximately 2% higher compared to the bulk hardness.

In summary, these results have shown that there is a significant hardness gradient below the Rockwell indent in the polycrystalline nickel. With the reduction in grain size to the ultrafine and nanocrystalline regime the gradient of the Vickers micro-hardness profile is less pronounced and the hardness plateaus at shorter distances. Thus, the strain hardening capacity of nickel is considerably reduced with the refinement of grain size.

The results from this experimental work are in general agreement with the results reported in previous studies, which observed a large strain hardening effect in polycrystalline nickel and very limited to no change in hardening in electrodeposited ultrafine grained and nanocrystalline nickel after strain is introduced into the specimens through cold rolling [Liang et al. (2008) and Zabev (2008) and Kulovits et al. (2008)]. As Meyers et al. pointed out, with the reduction in grain size the mean free path of dislocations decreases. Thus, this could possibly be the reason for the lack of forest dislocation storage within the finer grains which drive the hardening effect [Meyers et al. (2006)]. This is basically what the hardness profiles in the ultrafine grained and nanocrystalline nickel have shown in the current study; with a reduction in grain size down to 20 nm, the measured change in hardness decreased to 2% respectively; hence, the material's ability to accumulate dislocations decreased. In contrast, the hardness profile for the polycrystalline nickel, Ni 1, revealed significant increases in hardness. This is as expected since dislocation activity is the dominant deformation mechanism in polycrystalline materials where dislocations are envisioned to pass through the grain interiors, multiply and become trapped at grain boundaries. In agreement with previous results which showed very limited strain hardening capacity in ultrafine grained nickel, the current results support the idea that the dominant deformation mechanisms are grain boundary sliding and grain rotation as strong dislocation activity would be expected to result in measureable increases in hardness.

In contrast, Wu et al. [2009] reported significant strain hardening capacity for cryogenically deformed nanocrystalline nickel electrodeposits with a grain size of 20 nm on the basis of relatively large yield strength increases. It should be noted that this significant increase in hardness is unusual and the yield strength values used in their analysis were derived from Vickers micro-hardness tests using values for yield strength as one third of the Vickers hardness in GPA. Brooks et al. [2008] have recently shown that for many electroplated nanocrystalline materials, including nickel, such a relationship between hardness and yield strength is generally not applicable and that this relationship overestimates the yield strength of the material. Furthermore, no TEM micrographs, grain size distribution histograms or cumulative volume fraction curves were provided in the study by Wu et al. In fact, it was not even mentioned in their study how the grain size was determined. One possible reason for the unusual strain hardening behaviour reported by Wu et al. could be the non-uniformity of the microstructure in their material, whereby larger grains in the distribution could contribute to strain hardening, while the smaller grains were responsible for the strength increases. Clearly, this discrepancy requires further studies.

5.0 Conclusions

In the present study, relationships between Vickers micro-hardness and Rockwell/Superficial Rockwell hardness scales were studied for polycrystalline, ultrafine-grained and nanocrystalline nickel, where strengthening in these materials is mainly due to grain refinement. In addition, with the use of large Rockwell indentations combined with microhardness profiles, further insight into the strain hardening behaviour of polycrystalline and nanocrystalline nickel was obtained.

The relationships between Vickers micro-hardness and Rockwell/Superficial Rockwell hardness with ball and diamond indenters was developed in this study. By comparing the relationships observed in this study with the equations found in ASTM E140-07 for conventional nickel and nickel alloys, a clear trend was observed. At low load (15 kgf) the ASTM equations can be applied to describe the relationship between Vickers microhardness and Rockwell/Superficial Rockwell hardness. However, with an increase in penetration load to 30 and 45 kilograms force and reduction in grain size from polycrystalline to nanocrystalline the deviations between the two hardness scales increase. A prior study on indentation hardness testing showed that hardness measurements based on penetration depth methods are sensitive to the material's Young's modulus [D. Tabor (1951)]. While the composition of the nickel alloys used in ASTM's study were not given, it is likely that the discrepancies between the hardness values between this study and the ASTM study are due to the lower Young's modulus of the Ni_3Al precipitates, as it is speculated that Ni_3Al precipitates were responsible for the age hardening of nickel to achieve the highest Vickers hardness values. Thus, when applying the relationships given by ASTM for nickel and high nickel alloys to nanocrystalline nickel, the estimated hardness values are relatively accurate only for low Rockwell/Superficial Rockwell loads. At higher loads the ASTM conversions should be used with care as a direct conversion would underestimate the Superficial Rockwell and Rockwell hardness of nanocrystalline nickel.

Localized plastic deformation zones were introduced in polycrystalline and nanocrystalline nickel by large Rockwell indentations. Subsequently, Vickers micro-hardness profiles through these plastic zones revealed considerable work hardening in polycrystalline nickel for which the hardness close to the Rockwell indentation was about 100% higher than the bulk hardness of the undeformed material. In contrast, the hardness profile in the ultrafine grained nickel revealed a hardness increase of only 7% over the bulk hardness value. Furthermore, micro-hardness testing on the nanocrystalline specimens showed virtually no change in hardness in the cross section under the Rockwell indentation. In order to measure the hardness closer to the Rockwell indent, nano-indentation hardness values were measured beneath the Rockwell indent for the nanocrystalline nickel with an average grain size of approximately 20 nm. The results also showed little change in hardness, lending further support to the weak hardening capacity in nanocrystalline nickel. These differences in work hardening capacity support the general trends observed in other studies. The reduced strain hardening can be attributed to changes in deformation mechanisms as grain boundary sliding and creep, and grain rotation become the dominant deformation mechanisms.

6.0 Recommendations for Future Work

The following recommendations for future work are proposed to provide a more in depth investigation into microstructural and mechanical property evolution resulting from localized deformation in electrodeposited nanocrystalline nickel:

- Produce electrodeposited nanocrystalline nickels with even greater thickness to increase the Rockwell hardness indentation load to 150 kg force for both ball and diamond indenter. This would produce a larger localized plastic zone with even more severe plastic deformation and a large volume of deformation zone
- Perform electron backscatter diffraction or cross-sectional transmission electron microscopy analysis to investigate the possibility of dislocation activity and other deformation mechanisms in the localized deformed electrodeposited ultrafine-grained and nanocrystalline nickel before and after the indentation is introduced into the samples
- Similar studies should be completed on other important metals, e.g. electrodeposited nanocrystalline copper and conventional polycrystalline copper. As copper is one of the most commonly used metals in high conductivity applications, the relationships between Vickers and Rockwell hardness scales for poly and nanocrystalline copper could be of considerable industrial importance
- In addition, a further study is recommended for both nanocrystalline and polycrystalline materials which clearly separate strengthening effects due to strain hardening, precipitation hardening
- For polycrystalline materials with precipitation hardening as the main strengthening mechanism, a systematic study on the effect of the volume percentage of the precipiates

should be conducted. This should help to shed some light on the effect of elastic recovery after the applied load is removed in the hardness tests.

7.0 References

Alexandrov, I. V. and Valiev, R. Z.; Nanostr. Mater., 12 (1999) 709

Allen, S.M. and Thomas, E. L., The Structure of Materials, Wiley (2003)

Ashby, M.F., Verall, R.A., Acta Mater., 21 (1973) 149

Ashby, M.F., Scripta Metall., 3 (1969) 837

ASTM E18 – 08b, Specification for Test Method for Rockwell Hardness of Metallic Materials, ASTM International, West Conshohocken, PA. (2004)

ASTM E140 – 07, Standard Hardness Conversion Tables for Metals Relationship, ASTM International, West Conshohocken, PA. (2004)

ASTM E384 – 10^{e}2, Specification for Test Method for Knoop and Vickers Hardness of Materials, ASTM International, West Conshohocken, PA. (2004)

ASTM E2546 – 07, Standard Practice for Instrumented Indentation Testing, ASTM International, West Conshohocken, PA. (2011)

Aus, M.J., B. Szpunar, A.M. El-Sherik, U. Erb, G. Palumbo, and K.T. Aust, Scripta Metall., 27 (1992) 1639

Birringer, R., H. Hahn, H. Hofler, J. Karch and H. Gleiter, Defect and Diffusion Forum, 59 (1988) 17

Boylan, K., D., Ostrander, U. Erb, G. Palumbo, and K.T. Aust, Scripta Metall. Mater., 25 (1991) 2711

Brooks, I., P. Lin, G. Palumbo, G.D. Hibbard, and U. Erb, Mater. Sci. Eng., A491 (2008) 412

Callister, W.D., Fundamentals of Materials Science and Engineering, 2nd edition, John Wiley & Sons, Hokoen, NJ. (2005)

Cheung, C., F. Djuanda, U. Erb and G. Palumbo, Nanostr. Mater., 5 (1995) 513

Chokshi, A.H., A. Rosen, J. Karch, and H. Gleiter, Scripta Metall., 23 (1989) 1679

Doyle, D.M., G. Palumbo, K.T. Aust, A.M. El-Sherik, and U. Erb., Acta Metall. Mater., 43 (1995) 3027

Erb, U., NanoStr. Mater., 6 (1995) 533

Erb, U., K.T. Aust, & G. Palumbo, “Electrodeposited Nanocrystalline Metals, Alloys, and Composites”, in Nanostructured Materials: Processing, Properties, and Applications, 2nd Ed., C.C. Koch (ed.), William-Andrew Inc. (2007)

Eshebly, J. D., F. C. Frank. and F. R. N. Nabarro, 42 (1951) 351

Fecht, H.J., Phys. Rev. Lett., 65 (1990) 610

Fecht, H.J., and Y. Ivanisenko, "Nanostructured Materials and Composites Prepared by Solid State Processing", in Nanostructured Materials: Processing, Properties, and Applications, 2nd Ed., C.C. Koch (ed.), William-Andrew Inc. (2007)

Mechanical Testing Handbook, Metals Handbook Ninth Edition, American Society for Metals, Metal Park, Ohio (1985)

Girkins, R.C., K. U. Snowden, Nature 212 (1966) 916

Gleiter, H., J. Appl. Cryst., 24 (1991) 79

Gleiter, H., Progr. in Mater. Sci., 33 (1989) 223

Grovenor C.R.M., H.T.G. Hentzell, and D.A. Smith, Acta Metall., 32 (1984) 773

Gunther, B., and A. Kumpmann, Nanostr. Mat, 1 (1992) 27

Hahn, H., O., Mondal, K.A. Padmanabhan, Nanostr. Mater., 9 (1997) 603

Hall, E. O. Proc. Phys. Soc., 64 (1951) 747

Herring ,C., App. Phys., 21 (1949) 437

Herzer, G., Magnetics Society, 25 (1989) 3327

Herzer, G., Scripta Metall. Mater., 33 (1995) 1741

Huges, G. D., S. D. Smith, C. S. Pande, H. R. Johnson, and R. W. Armstrong, Scripta Metall. Mater., 20 (1986) 93

Iwahashi, Y., M. Furukawa, Z. Horita, M. Nemoto and T.G. Langdon, Metall. Mater. Trans. A, 29 (1998) 2245

Iwama, S., and K. Hayakawa, Nanostr. Mat., 1 (1992) 113

Komara, S. J. Mater. Res., 14 (1999) 4044

D. Kuhlmann-Wilsdorf, *ibid.* A113 (1989) 1.

Kulovits A., S. X. Wao and J.M K. Wiezovek, Acta Mater., 51 (2008) 4846,

Lu, K., W.D. Wei, J.T.J. Wang, Scripta Metall. Mater., 24 (1990) 2319

McMahon, G. and U. Erb, Microstruct. Sci., 17 (1989) 447

Metals Handbooks, 2nd edition, J.R. Davis and Davis & Associates, ASM International, Materials Park, OH, 1998

Murayama, M., J.M. Howe, H. Hidaka, and S. Takaki, Science, 295 (2006) 2433

Nieman, G. W., J. R.Weertman, R.W. Siegel, Scripta Metall. Mater., 24 (1990) 145

Nieh, T.G., and J. Wadsworth, Scripta Metall. Mater., 25 (1991) 955

Palumbo, G., S.J. Thorpe and K.T. Aust, Scripta Metall. Mater., 24 (1990) 1347

Palumbo, G., U. Erb, K.T. Aust, Scripta Metall. Mater., 24 (1990) 2347

Petch, N. J. J. Iron Steel Inst., 174 (1953) 25

Rawer, J., G. Slaven, R. Krabbe, Metall. Mater. Trans. A, 27 (1996) 3126

Rofagha, R., R. Langer, A. M. El-Sherik, U, Erb, G. Palumbo, K. T. Aust, Scripta Metall. Mater., 25 (1991) 2867

Siegel, R.W., In Processing and Properties of Nanocrystalline Materials, C. Suryanaranana, J. Singh, and F.H. Froes (eds.), TMS, Warrendale, PA (1996) 3

Siegel, R. W., and J. A. Eastman, Multiocomponent Ultrafine Microstructures, 132 (1989) 3

Siegel, R.W., and M. Nastasi, "Mechanical Properties and Deformation Behavior of Materials", (1993) 509

Suryanaranana, C. and C.C. Koch, Hyperfine Interactions, 130 (2000) 5

Wang, N., Z. Wang, K. T. Aust and U. Erb, Mat. Sci. Eng., A237 (1997) 150

Whang, S. H., Nanostructured Metals and Alloys: Processing, Microstructure, Mechanical Properties and Applications, Woodhead Publishing Limited, Oxford, UK, (2011)

Wu, X.J., L.G. Du, H.F. Zhang, J.F. Liu, U.S. Zhou, Z.Q. Li, L.Y. Xiong, and Y.L. Bai, Nanostr. Mater., 12 (1999) 221

Wu. X. L., Y. T. Zhu, Y. G. Wei and Q. Wei, Physical Review Letters, 103 (2009) 205504

Yu, B., P. Woo, U. Erb and G. Palumbo, Processing and Fabrication of Advanced Materials XV, ASM, Materials Park, OH, (2006) 321

Van Swygenhoven, H., and P.M. Derlet, Phys. Rev. B, 64 (2001) 2241051

Zabev, T., M.A.Sc. Thesis, U of T, 2008

Appendix

ASTM Standard Hardness Conversion Tables for Nickel and High-Nickel Alloys

Hardness conversion numbers for Ni and high nickel alloys			
Vickers indenter 1, 5, 30 kgf (HV)	**A scale (60gkf diamond tip) HRA**	**B Scale (100 kgf 1/16inch ball tip) HRB**	**C Scale (150kgf diamond tip) HRC**
513	75.5		50
481	74.5		48
452	73.5		46
427	72.5		44
404	71.5		42
382	70.5		40
362	69.5		38
344	68.5		36
326	67.5		34
309	66.5	106	32
285	64.5	104	28.5
266	63	102	25.5
248	61.5	100	22.5
234	60.5	98	20
220	59	96	17
209	57.5	94	14.5
198	56.5	92	12
188	55	90	9
179	53	88	6.5
171	52.5	86	4
164	51.5	84	2
157	50	82	
151	49	80	
145	47.5	78	
145	46.5	76	
140	45.5	74	
135	44	72	
126	43	70	
122	43	68	
119	41	66	
115	40	64	
112	39	62	
108		60	
106		58	
103		56	
100		54	

98		52	
95		50	
93		48	
91		46	
89		44	
87		42	
85		40	
83		38	
81		36	
79		34	
78		32	
77		30	

D Scale (100kgf diamond tip) HRD	E Scale (100kgf 1/8inch ball) HRE	F Scale (60kgf 1/16inch ball) HRF	G Scale (150 kgf 1/16 inch ball) HRG
63			
61.5			
60			
58.5			
57			
55.5			
54			
52.5			
50.5			
49.5		116.5	94
46.5		115.5	91
44.5		114.5	87.5
42		113	84.5
40		112	81.5
38		111	78.5
36		110	75.5
34		108.5	72
32	108.5	107.5	69
30	107	106.5	65.5
28	106	105	62.5
26.5	104.5	104	59.5
24.5	103	103	56.5
22.5	102	101.5	53
21	100.5	100.5	50
19	99.5	99.5	47
17.5	98	98.5	43.5
16	97	97	40.5
14.5	95.5	96	37.5
13	94.5	95	34.5
11.5	93	93.5	31
10	91.5	92.5	
8	90.5	91.5	
	89	90	
	88	89	
	86.5	88	
	85.5	87	
	84	85.5	
	83	84.5	
	81.5	85.5	
	80.5	82	
	79	81	
	78	80	
	76.5	79	
	75	77.5	

	74	76.5	
	72.5	75.5	
	71.5	74	
	70	73	

15kgf diamond (HR 15-N)	***30kgf Diamond (HR 30-N)***	***45kgf Diamond (HR 45-N)***	**15kgf 1/16inch ball (HR 15-T)**
85.5	68	54.5	
84.5	66.5	52.5	
83.5	64.5	50	
82.5	63	47.5	
81.5	61	45.5	
80.5	59.5	43	
79.5	58	41	
78.5	56	38.5	
77.5	54.5	36	
76.5	52.5	34	94.5
75	49.5	30	94
73.5	47	26.5	93
72	44.5	23	92.5
70.5	42	20	92
69	39.5	17	91
68	37.5	14	90.5
66.5	35.5	11	89.5
65	32.5	7.5	89
64	30.5	5	88
62.5	28.5	2	87.5
61.5	26.5	-0.5	87
			86
			85.5
			84.5
			84
			83
			82.5
			82
			81
			80.5
			79.5
			79
			78.5
			77.5
			77
			76
			75.5
			74.5
			74
			73.5
			72.5
			72
			71
			70.5

			70
			69
			68.5
			67.5

30kgf 1/16inch ball (HR 30-T)	45kgf 1/16 inch ball (HR 45-T)
85.5	77
84.5	75
83	73
81.5	71
80.5	69
79	67
77.5	65
76	63
75	61
73.5	59.5
72	57.5
70.5	55.5
69.5	53.5
68	51.5
66.5	49.5
65.5	47.5
64	45.5
62.5	43.5
61	41.5
60	39.5
58.5	37.5
57	35.5
56	33.5
54.5	31.5
53	29.5
51.5	27.5
50.5	25.5
49	23.5
47.5	21.5
46.5	19.5
45	17
43.5	14.5
42	12.5
41	10
39.5	7.5
38	5.5

36.5	3
35.5	1
34	-1.5